

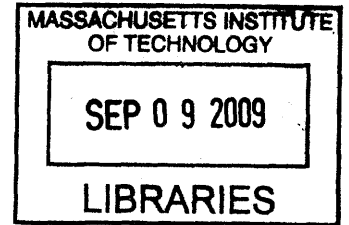
Planar Chalcogenide Glass Materials and Devices

by

Juejun Hu

B.S. Materials Science and Engineering

Tsinghua University, 2004



Submitted to Department of Materials Science and Engineering in Partial Fulfillment of the
Requirements for the Degree of

Doctor of Philosophy in Materials Science and Engineering

at the

Massachusetts Institute of Technology

September 2009

ARCHIVES

© 2009 Massachusetts Institute of Technology. All rights reserved.

Signature of Author: _____

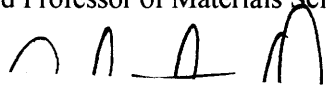
Department of Materials Science and Engineering

August 8th, 2009

Certified by: _____

Lionel C. Kimerling

Thomas Lord Professor of Materials Science and Engineering

 Thesis Supervisor

Accepted by: _____

Christine Ortiz

Professor of Materials Science and Engineering

Chair, Departmental Committee on Graduate Students

To my father, 胡日晶

For the courage and perseverance

勇气和坚持

Planar Chalcogenide Glass Materials and Devices

by

Juejun Hu

Submitted to the Department of Materials Science and Engineering on November 3rd, 2008, in
Partial Fulfillment of the Requirement for the Degree of Doctor of Philosophy in Materials Science and
Engineering.

Abstract

The intrinsic advantages of small footprint, low fabrication cost and immunity to electromagnetic interference make planar photonic device technologies a promising solution to a number of key technical challenges. The examples include high-speed telecommunication, on-chip optical interconnect, imaging and photovoltaics. Another important area planar photonic technologies may penetrate into is biochemical sensing. High precision optical metrology tools can be applied to detect optical property changes associated with the presence of biological or chemical molecules, leading to sensitive, rapid detection of these molecular species.

In this thesis, we focus on the development of novel photonic materials and devices that address the emerging need in the field of biochemical sensing. Chalcogenide glasses have been identified as the material of choice for sensing due to their wide infrared transparency window; on the device side, we have fabricated optical resonator devices that dramatically amplify the photon-molecule interactions towards highly sensitive detection.

We have developed and optimized a lift-off patterning technique for Si-CMOS backend compatible fabrication of high-index-contrast (HIC) chalcogenide glass devices. A thermal reflow technique further removes the sidewall roughness resulting from the patterning process and is shown to effectively reduce the scattering loss in chalcogenide glass waveguides. Using the lift-off technology, we have demonstrated the first micro-ring and micro-disk resonators in chalcogenide glasses, with a record loaded cavity quality factor (Q-factor) exceeding 2×10^5 .

We have shown that these high-Q chalcogenide glass resonators can serve as highly sensitive refractometry sensors with a refractive index detection limit down to 8×10^{-7} . This high sensitivity agrees with our theoretical analysis, which predicts one to two orders of magnitude performance improvement over surface plasmonic resonance (SPR) sensors. The optofluidic resonator devices are leveraged to detect surface binding of biological molecules. Label-free detection of proteins at clinically relevant concentrations (< 1 ng/mL) has been experimentally verified.

We have also demonstrated cavity enhanced absorption spectroscopy near the 1500 nm infrared wavelength. By taking advantage of the strong optical resonance enhancement, we achieved 3-fold chemical sensing sensitivity improvement and 40-fold device physical size reduction simultaneously compared to evanescent waveguide sensors, which clearly demonstrates the competitive advantage of using resonators for cavity enhanced infrared absorption spectroscopy.

Lastly, we have developed a novel precision metrology technique, resonant cavity refractometry, for glass property investigation. It leverages the extreme sensitivity of optical resonators to optical property change of their constituent materials, to accurately extract property and micro-structural evolution information of glass materials. We apply this technique to characterize photosensitive index change and two-photon absorption in chalcogenide glasses with very high accuracy. We also report the first experimental observation of cavity-enhanced photosensitivity of As_2S_3 glass to 1550 nm telecommunication wavelength light, an important design consideration for nonlinear optical devices using chalcogenide glasses*.

Thesis Supervisor: Lionel C. Kimerling

Title: Thomas Lord Professor of Materials Science and Engineering

* This thesis summarizes my Ph.D. work on chalcogenide glass materials and devices. Please refer to my web page: web.mit.edu/hujuejun/www for information about my other research projects, including cavity optomechanics, multi-spectral detectors and integrated magneto-optics.

(This page is not intentionally left blank)

Table of Content

| | |
|---|----|
| Abstract..... | 5 |
| Acknowledgements..... | 15 |
| Chapter 1. Introduction..... | 20 |
| 1.1. Label-free biological detection: challenges and opportunities..... | 20 |
| 1.2. Infrared absorption spectroscopy for chemical sensing..... | 24 |
| 1.3. Precision refractometry techniques for glass metrology..... | 26 |
| Chapter 2. Chalcogenide glass materials..... | 29 |
| 2.1. Structure of chalcogenide glasses and network rigidity..... | 29 |
| 2.2. Density of states and electrical conduction..... | 31 |
| 2.3. Optical transparency..... | 35 |
| 2.4. Photosensitivity and other photo-induced transformations..... | 36 |
| 2.5. Kerr nonlinearity, two photon absorption and magneto-optical properties..... | 38 |
| 2.6. Planar chalcogenide photonic device fabrication techniques..... | 40 |
| 2.7. Why chalcogenide glass?..... | 42 |
| Chapter 3. Optical resonators..... | 44 |
| 3.1. Basic resonator configurations..... | 44 |
| 3.1.1. Standing wave resonators..... | 45 |
| 3.1.2. Travelling wave resonators..... | 46 |
| 3.2. Optical parameters characterizing a resonator..... | 46 |
| 3.2.1. Free spectral range..... | 47 |
| 3.2.2. Cavity quality factor and finesse..... | 47 |
| 3.2.3. Extinction ratio and coupling regimes..... | 49 |

| | |
|---|----|
| 3.3. Experimental characterization of optical resonators..... | 51 |
| 3.4. Applications | 52 |
| Chapter 4. Processing development for planar chalcogenide glass devices | 53 |
| 4.1. Bulk glass preparation and glass film deposition | 53 |
| 4.2. Si-CMOS backend-compatible lift-off patterning [†] | 56 |
| 4.3. Comparison of lift-off and plasma etching techniques [‡] | 66 |
| 4.4. Optical loss reduction in high index contrast (HIC) chalcogenide glass waveguides via thermal reflow [§] | 75 |
| 4.4.1. Kinetic theory of roughness and optical loss evolution during reflow | 76 |
| 4.4.2. Experiment..... | 82 |
| 4.5. Optofluidic integration..... | 89 |
| 4.6. Summary | 90 |
| Chapter 5. Chalcogenide glass optical resonators..... | 92 |
| 5.1. Racetrack resonators | 92 |
| 5.2. Micro-disk and micro-ring resonators | 95 |
| 5.2.1. Modal properties | 95 |
| 5.2.2. Pulley-type coupler | 97 |

[†] Work presented in this section has been published in: “Si-CMOS-compatible lift-off fabrication of low-loss planar chalcogenide waveguides,” *Opt. Express* **15**, 11798-11807 (2007).

[‡] Work presented in this section has been published in: “Exploration of Waveguide Fabrication From Thermally Evaporated Ge-Sb-S Glass Films,” *Opt. Mater.* **30**, 1560-1566 (2007).

[§] Work presented in this section will be summarized in a paper entitled: “Optical loss reduction in HIC chalcogenide glass waveguides via thermal reflow”.

| | |
|---|-----|
| 5.2.3. Experimental characterizations** | 99 |
| 5.3. Summary | 101 |
| Chapter 6. Design guidelines for optical resonator sensors ^{††} | 102 |
| 6.1. Introduction of the time-normalized sensitivity S^* | 103 |
| 6.2. Noise analysis | 106 |
| 6.2.1. Intensity noise and wavelength noise | 106 |
| 6.2.2. Noise simulation results | 107 |
| 6.3. Design optimization of resonator sensors | 113 |
| 6.3.1. Sensor device figure-of-merit | 113 |
| 6.3.2. Parameter dependence of S^* | 114 |
| 6.3.3. Origin and mitigation of thermally-induced refractive index fluctuation..... | 116 |
| 6.3.4. Application to S^* optimization | 118 |
| 6.4. Experiment | 120 |
| 6.4.1. Wavelength resolution dependence on cavity Q-factor | 120 |
| 6.4.2. Impact of humidity and mitigation | 122 |
| 6.5. Summary | 122 |
| Chapter 7. Biological sensing using resonator refractometry | 124 |
| 7.1. Measurement of refractive index sensitivity | 124 |
| 7.2. Quantitative theory of molecular binding and resonant wavelength shift | 126 |

** Work presented in this section has been published in: “Planar waveguide-coupled, high-index-contrast, high-Q resonators in chalcogenide glass for sensing,” *Opt. Lett.* **33**, 2500-2502 (2008).

†† Work presented in this chapter has been published in: “Design guidelines for optical resonator biochemical sensors,” *J. Opt. Soc. Am. B.* **26**, 1032-1041 (2009).

| | |
|---|-----|
| 7.3. Protein detection test..... | 129 |
| 7.3.1. Glass surface functionalization..... | 129 |
| 7.3.2. Prostate specific antigen testing..... | 129 |
| 7.3. Summary | 132 |
| Chapter 8. Infrared absorption spectroscopy | 133 |
| 8.1. Waveguide evanescent wave sensor ^{††} | 133 |
| 8.1.1. Theory | 133 |
| 8.1.2. Experiment..... | 134 |
| 8.2. Resonant cavity enhanced infrared absorption spectroscopy ^{§§} | 139 |
| 8.2.1. Theory | 139 |
| 8.2.2. Experiment..... | 146 |
| 8.3. Summary | 149 |
| Chapter 9. Resonant cavity refractometry for precision glass metrology..... | 151 |
| 9.1. Photosensitivity kinetics of chalcogenide glass to near-band gap illumination ^{***} | 151 |
| 9.2. Measuring nonlinear absorption in chalcogenide glass using cavity enhanced absorption spectroscopy..... | 155 |

†† Work presented in this section has been published in: “Fabrication and Testing of Planar Chalcogenide Waveguide Integrated Microfluidic Sensor,” *Opt. Express* **15**, 2307-2314 (2007).

§§ Work presented in this section will be summarized in a paper entitled: “Cavity-enhanced infrared absorption in planar chalcogenide glass resonators -- experiment & analysis.”

*** Work presented in this section has been published in: “Demonstration of chalcogenide glass racetrack micro-resonators,” *Opt. Lett.* **33**, 761-763 (2008).

| | |
|--|-----|
| 9.3. Thermo-optic cavity instability..... | 158 |
| 9.4. Resonant cavity enhanced photosensitivity in As ₂ S ₃ chalcogenide glass at 1550 nm telecommunication wavelength ^{†††} | 159 |
| 9.5. Aging of As ₂ S ₃ chalcogenide glass..... | 162 |
| 9.6. Summary | 164 |
| Chapter 10. Investigation of copper alloying effects in As-Se-Te glass ^{†††} | 166 |
| 10.1. Film deposition | 167 |
| 10.2. Single source thermal evaporation of Cu doped films in the system As _{0.40} Se _{0.35} Te _{0.25} | 168 |
| 10.2.1. Source characterization..... | 168 |
| 10.2.2. Single-source film characterization | 173 |
| 10.3. Dual source co-evaporation of As-Se-(Te)-Cu Films..... | 175 |
| 10.4. Summary | 180 |
| Chapter 11. Summary and future work..... | 181 |
| 11.1. Summary | 181 |
| 11.1.1. Resonator refractometry for biological sensing..... | 181 |
| 11.1.2. Cavity enhanced infrared spectroscopy for chemical detection | 181 |
| 11.1.3. Resonant cavity refractometry for precision glass metrology | 182 |
| 11.2. Future work..... | 183 |

^{†††} Work presented in sections 9.2 - 9.4 will be summarized in a paper entitled: “Resonant cavity enhanced photosensitivity in As₂S₃ chalcogenide glass at 1550 nm telecommunication wavelength”.

^{†††} Work presented in this chapter has been published in: “Studies on Structural, Electrical and Optical Properties of Cu-doped As-Se-Te Chalcogenide Glasses,” *J. Appl. Phys.* **101**, 063520 (2007).

| | |
|---|-----|
| 11.2.1. Resonator refractometry for biological sensing..... | 183 |
| 11.2.2. Cavity enhanced infrared spectroscopy for chemical detection | 184 |
| 11.2.3. Resonant cavity refractometry for precision glass metrology | 185 |
| 11.2.4. Planar integration: case-by-case analysis..... | 185 |
| Appendix I. Derivation of useful relations in micro-ring/micro-disk resonators | 187 |
| I.1. Cavity Q-factor and optical loss | 188 |
| I.2. Free spectral range and finesse..... | 191 |
| I.3. Resonant field enhancement factor..... | 192 |
| I.4. Resonant wavelength shift as a function of effective index change..... | 193 |
| Appendix II. Monte-Carlo simulation methodology for sensor wavelength resolution determination | 194 |
| Appendix III. Calculation of autocorrelation function evolution during reflow | 198 |
| References..... | 199 |

Acknowledgements

Writing a long acknowledgement section without incurring additional page charges is a privilege that does not come very often when publishing papers. As Richard Feynman has correctly pointed out: “We have a habit in writing articles published in scientific journals to make the work as finished as possible ... so there isn’t any place to publish in a dignified manner what you actually did to get to do the work.” Therefore I do would like to take full advantage of this opportunity to express my deep gratitude to the people who have been kindly helping and supporting me along the way in the past five years.

The outstanding scholastic atmosphere at MIT has made it an amazing and exciting place for pursuing my graduate career. I am very fortunate to have worked with the people MIT hosts who share the same passion and fascination with natural sciences, an experience that I will always cherish in the rest of my life.

My thesis advisor, Professor Lionel C. Kimerling “Kim”, the fearless leader of the Electronic Materials (EMAT) group, has led me to the fascinating field of photonics. His guidance has been a constant source of inspiration. He provided me the freedom to pursue my research interests, to collaborate with other research groups around the globe, and to explore various career opportunities. Kim is also a very nice mentor; he assumes an encouraging approach, and is always supportive of his students. His knowledge, experience, vision and leadership will be invaluable assets I will always admire, learn from and refer to in my career. Thank you so much, Kim, for all your help, your support, and your guidance!

Dr. Anu Agarwal has served as my daily research supervisor. She encourages me to step on the previously uncharted territory of chalcogenide materials in our group, and her constant support has been critical in my research. Started as a green college graduate, I have learnt from Anu the skill set for success in an academic career, from fostering collaborations to writing funding proposals. She is also a very warm and pleasant person to work with, and I feel blessed to enjoy the research with her cheerful demeanor. I owe her my deep gratitude for her help to me in every aspects of my graduate work.

My thesis committee has given me a lot of help to my research work. Proferssor Kathleen Richardson, a leader in chalcogenide materials research, my long-time advisor and collaborator on glass materials, has guided me to a unique combination of materials science and device physics, the key enabler of my thesis work. She has also helped my work tremendously through her insightful suggestions that pave the way towards success. Besides, I am deeply indebted to her role as my mentor who cares and supports my career development. Professor Caroline Ross's advice has been very helpful in improving my thesis work. I have also enjoyed the collaboration with her group on magneto-optical materials and devices. Professor Darrell Irvine's feedback always points to exciting directions of my research. I feel so privileged to have the world-class experts on my committee, and their advising have made my thesis research ever possible.

I have worked on the solar cell project with Dr. Jurgen Michel, the principal research scientist in EMAT, and a sharp-minded physicist. I benefited a lot from the fruitful

interactions with him dealing with the intriguing scientific problems. I have always enjoyed discussions with Professor Kazumi Wada; he captures new concepts and extracts scintillating novel ideas in his hallmark way. Dr. Xiaoman Duan takes motherly care of every EMAT students. Dr. Anat Eshed has taught me how to use the sputtering station and has helped me on maintaining the vacuum systems. Dr. Jifeng Liu has set a high academic standard for all the Tsinghua graduates at MIT DMSE and he is the role model I have always been emulating. I also greatly appreciate his help all the way from my application to graduate schools to the consolidation of my latest ideas. Dr. Yasha Yi pioneered biophotonics in my group and his enlightening work has introduced me to this emerging and exciting field. Dr. Rong Sun and I have followed an identical path since we both came to MIT in 2004; we have become classmates, lab mates and our friendship has even extended to the online virtual world. It has been a great pleasure to work and hang out with him. He also makes himself available whenever I need assistance on my experiments. In the initial stages of my graduate work, I have greatly profited from the experimental skills that my colleagues Dr. Luca Dal Negro, Dr. David Danielson, Dr. Daniel Sparacin, and Dr. Mike Stolfi have taught me. I have shared office with Dr. Donghwan Ahn, Dr. Shoji Akiyama, Dr. Marianne Hiltunen, Suguru Akiyama, Yokia Miyachi, Dr. Wojciech Giziewicz, Michiel Vanhoutte, and Jianfei Wang. I will miss the office parties and all the fun and beers we had together. During my thesis work, I have enjoyed interacting with other students and post-docs of my group, Dr. Winnie Ye, Dr. Ching-yin Hong, Dr. Clara Dimas, Dr. Dong Pan, Dr. Jae-Hyung Yi, Dr. Victor Nguyen, Dr. Samerkhae Jongthammanurak, Dr. Lirong Zeng, Dr. Sajan Saini, Rodolfo Camacho-

Aguilera, Jing Cheng, Kevin McComber, Vivek Raghunathan, Xing Sheng, Timothy Zens and Sarah Bernardis.

I would like to thank my collaborators, the great minds that have helped paved my way towards my research goals. Nathan Carlie, Jonathan Massera, Dr. Laeticia Petit at Clemson University are the trustworthy materials experts who create these amazing chalcogenide glasses with guaranteed high quality throughout the years. They are also the ones who have shared their intriguing new ideas with me, reviewed my paper manuscripts, and inspired novel research pathways. On the softer side, we had a lot of fun chatting on topics ranging from French wines to the sunshine in Orlando. Dr. Bogdan Zdyrko and Professor Igor Luzinov are the polymer magicians whose magic polymer coatings always give us happy surprises. Their warm attitude and easy-going personality also made our collaboration a most pleasant experience. Mr. Troy Anderson at UCF have extended the application of chalcogenide thin films using the versatile femtosecond laser processing technique; and I also would like to acknowledge his and Professor Martin Richardson's many insightful suggestions that have helped me to think deeper into and perfect the optical sensing technologies. Dr. Matteo Torregiani, Dr. Francesco Morichetti and Professor Andrea Melloni at Politecnico Di Milano are brilliant and creative device scientists who lead the pioneering experiments on novel chalcogenide devices and resonant cavity refractometry; I have enjoyed the collaboration a lot, as well as the beautiful Milano city. I am glad to have the opportunity to work with Mr. Shiyun Lin and Professor Kenneth Crozier at Harvard University on cavity optomechanics: I have truly enjoyed the stimulating and interesting discussions. Mr. Lei Bi and I share the same

passion on science; the same fascination has led to a fruitful and pleasant collaboration on magneo-optics with Professor Caroline Ross's group. I would like to thank Dr. Shaun Filocamo and Dr. Romy Kirby who have taught me the surface chemistry that enabled my biological sensing experiments. I also would like to acknowledge Dr. Joel Hensley, Dr. Krishnan Parameswaran, Dr. Mark Allen from Physical Sciences Inc. for kindly performing the mid-infrared measurements. Dr. Ning-Ning Feng from Kotura Inc. is an ingenious photonics simulation expert; throughout the years, he has helped me with numerous device simulations which I immensely appreciate. And finally, I owe my special gratitude to Dr. Xiaochen Sun, my former classmate and officemate. I always feel that it was such a privilege for me to have worked with him, a truly gifted scientist. The intellectually stimulating and enjoyable discussions with him are among the most memorable experiences throughout my stay at MIT.

Thank you Di for your companion, your support, your advice and your love. You are the angel who painted the brisk colors on the canvas of my life. I know we will carry on, and overcome any challenge on the road ahead, hand-in-hand.

我还要深深感谢我的父母，他们对我的信任，支持，鼓励，和无私的爱我永远铭记在心。你们积极乐观的生活态度，坚忍不拔的毅力，和面对挫折永不言败的精神是我毕生学习的榜样。我在大洋彼岸，为你们致以我最美好的祝愿。我爱你们。

Chapter 1. Introduction

1.1. Label-free biological detection: challenges and opportunities

Recent development in the fields of pharmaceuticals, biotechnology, food safety, clinical diagnostics and biodefense has seen the increasing need for a high-throughput, label-free biological molecular interaction analysis platform with high sensitivity and specificity. Understanding the binding interactions (including specificity, affinity and kinetics) between biological molecules is of fundamental importance in technical fields such as proteomics, immunogenicity, drug discovery, antibody screening, and biotherapeutic development. In addition, whereas detection of trace amount of pathogens comprises the core technical requirement for anti-bioterrorism, specific and sensitive identification of certain proteins has been proposed for a number of clinical diagnostic applications, including early detection of cancer¹.

So far, the gold standard for biological molecule (in particular, protein) analysis is a label-based conventional immunoassay test called ELISA (Enzyme-Linked ImmunoSorbent Assay). ELISA relies on chromogenic or fluorescent labels to detect the presence of certain molecular species. It features highly specific (especially in the case of a sandwiched ELISA), and highly sensitive detection for a wide range of protein molecules. However, because of the multiple labeling and reaction steps, ELISA tests typically take 5 hours to overnight to run. Figure 1 illustrates the major operation procedures in an ELISA test. The test is time-consuming and labor-intensive; the high degree of complication also increases the risk of human error. An automatic ELISA

testing bench can lead to ~ 1.5 hour time-saving; however, such machines for clinical purposes cost approximately \$100,000.

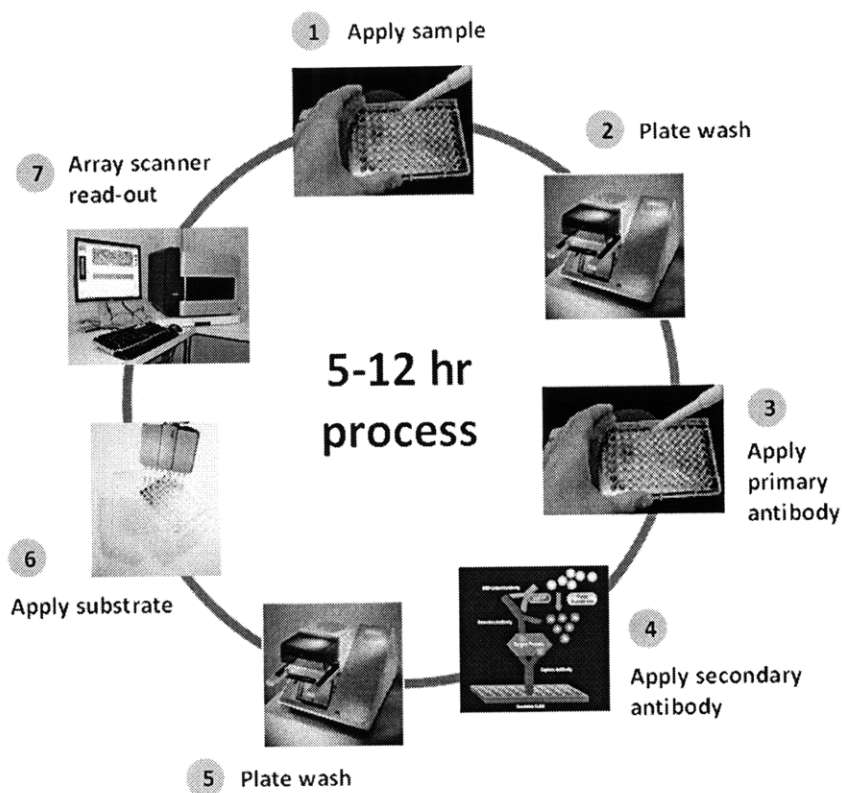


Figure 1 Schematic illustration of ELISA test procedures

Label-free detection techniques have thus been proposed as alternatives for ELISA testing. Compared to conventional label-based immunoassay testing, label-free techniques feature rapid detection, lower reagent and labor cost, as well as elimination of influence from labels on the physiochemical properties of the molecules to be analyzed. In addition, several label-free techniques such as surface plasmon resonance (SPR) are capable of measuring the molecular binding kinetics in real-time, a capability ELISA cannot accomplish. Despite these advantages, label-free techniques are often criticized for their lower sensitivity compared to label-based assays; in addition, some of the label-

free techniques require costly machines to operate (e.g. commercial Biacore SPR automatic protein analysis systems cost up to ~ \$300,000, and the price of each sensor chip ranges from \$200-600), largely due to the need for discrete optical components as well as complicated peripheral electronics for signal readout and interpretation. In addition, insufficient surface binding specificity of label-free techniques in biological fluids and limited measurement throughput are two major factors limiting their biomedical and clinical applications. Table 1 lists the sensitivity figures reported for several common label-free techniques. Note that the sensitivity figures are also normalized to surface mass load sensitivity to facilitate direct comparison between these technologies.

Table 1 Performance comparison of label-free detection technologies

| Sensor type | Sensitivity reported | Normalized sensitivity (ng/cm ²) | References |
|---------------------------------|--|---|------------|
| Surface plasmon resonance (SPR) | 10 ⁻⁵ to 10 ⁻⁶ RIU | 0.1 to 1 | 2, 3, 4 |
| Quartz crystal micro-balance | 35 pmol | ~ 0.2 | 5 |
| Ion channel chemistry | ~ nM | 10 to 100 | 6 |
| Micro-cantilever | 1.4 ag to > 100 pg | 0.02 to 10 | 7, 8, 9 |
| Micro-calorimetry | ~ 10 µg | > 10 ³ | 10 |
| Electrochemistry | ~ 0.1 ng/mL | ~ 100 | 11, 12 |

Our investigation in this thesis focuses on the development of a novel protein-interaction sensor platform that leverages on mature CMOS manufacturing technology, and high-Q optical resonance, thus achieving low cost, improved sensitivity and multiplexed detection on a miniaturized sensor chip platform. Figure 2 illustrates the operating principles of an optical resonator biosensor. Light from a laser diode is coupled into a planar waveguide via an optical coupler, passing through a microfluidic-integrated chalcogenide glass micro-disk resonator, and subsequently detected by a photodiode. The resonator surface is functionalized with antibodies conjugate to the biomarker molecules to be detected. When the resonator is exposed to liquid samples containing the molecules to be detected, specific surface molecular binding occurs. The refractive index change resulting from surface molecular binding leads to a resonant frequency change of the optical resonator that can be detected by the photodiode. The high-Q optical resonance leads to strong interaction between photons and the molecules to be detected and hence very high sensitivity.

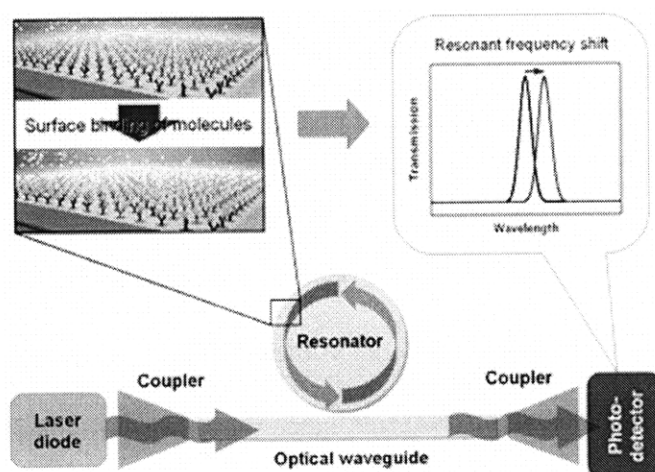


Figure 2 Schematic diagram illustrating the operating principles of an optical resonator biosensor

The competitive advantages of the proposed technology include:

- 1) *rapid, sensitive* detection which is achieved by a combination of microfluidic sample delivery (rapid) and strong optical resonance enhancement (sensitive), without the need for time-consuming fluorescent labeling;
- 2) utilization of the asset base of mature silicon CMOS fabrication technology to significantly *reduce the cost* and enable a small-footprint cartridge design ideal for *point-of-care* applications; and
- 3) a detection mechanism which can be applied to a wide range of molecular species including proteins, nucleic acids and certain small molecules, thus making it a versatile *platform technology* for biomedical applications.

1.2. Infrared absorption spectroscopy for chemical sensing

Perhaps the most widely used method of applied spectroscopy, infrared (IR) absorption spectroscopy probes the characteristic vibration spectra of molecular species, and provides a wealth of structural and chemical information. This unique capability of infrared spectroscopy has led to numerous applications in environmental monitoring¹³, medical diagnosis¹⁴, forensic analysis¹⁵ and pharmaceutical manufacturing¹⁶.

Traditional infrared spectrophotometers usually employ a free-space geometry to measure single-pass absorbance. Such a configuration, however, poses a trade-off between sensitivity and instrument footprint, since the sensitivity gain has to be achieved via increasing optical path length. Such a constraint can be overcome by using a resonant cavity (optical resonator), which offers resonantly-enhanced, long optical path length

while still maintaining a small physical device size¹⁷. Compared to Fabry-Perot resonant cavities comprised of a pair of highly reflective mirrors, index-guided planar resonators such as microrings and microdisks do not require complicated optical alignment, and can be mass produced at very low cost via mature planar CMOS microfabrication technologies. To date, cavity-enhanced absorption spectroscopy has only been demonstrated in index-guided resonators made of traditional optical materials such as silica^{18, 19} and more recently silicon-on-insulator²⁰. The operation wavelength selection of such devices is bounded by the limited infrared transparency window of the dielectric or semiconductor materials used. Although the absorption fingerprints of most molecular species lie in the mid-wave and long-wave infrared (wavelength $> 3 \mu\text{m}$), cavity-enhanced spectroscopy in these wavelength range remains largely unexplored due to the limited material choice.

Chalcogenide glasses (ChG's), namely the amorphous compounds containing S, Se and/or Te, have been recognized as a material of choice for infrared applications thanks to their wide optical transparency in the mid-wave and long-wave infrared. The wide infrared transparency window of chalcogenide glasses covers the characteristic absorption wavebands for most molecules of interest. Further, their amorphous nature allows ChG glass film deposition on virtually any substrate using low-cost, large-area techniques such as evaporation and sputtering. Lastly, sidewall roughness on as-fabricated chalcogenide glass guided wave photonic devices can be effectively removed to achieve low optical loss, a unique advantage over crystalline materials (Chaper 5).

In this thesis, we will present the fabrication and characterization of planar evanescent waveguide and optofluidic micro-disk resonators chalcogenide glass for infrared spectroscopy (Chapter 8).

1.3. Precision refractometry techniques for glass metrology

Unlike their single crystalline counterparts, materials in amorphous state or glassy state are thermodynamically unstable, and the structural relaxation processes in glass towards thermodynamically more stable state is only inhibited kinetically. Therefore, the microstructures of glass materials can be subjected to change when additional energy is supplied in the form of heat (annealing or sub- T_g structural relaxation) or light (photosensitivity). Such structural transformations are intriguing issues for fundamental scientific investigations, as they provide important information regarding the structure and properties of glasses. For example, study of glass transition, a phenomenon of fundamental importance in glass science, has centered on the associated structural modifications occurring near the transition temperature. On the other hand, structural evolutions in glasses are technically important for a wide array of practical applications, as glass properties also vary when the glass micro-structure changes. For instance, sub- T_g structural relaxation in glasses is usually accompanied by a change of glass refractive index; under certain circumstances, such a time evolution of refractive index can severely disrupt photonic device performance. Photo-induced index change in chalcogenide glasses has been applied to create direct-written photonic devices: the sign and magnitude of photo-induced index modification largely determines the performance characteristics of the device and thus requires in-depth understanding of its kinetics.

A range of metrology tools have been applied to study glass micro-structural evolution. X-ray diffraction characterizes glass network ordering, phase composition and crystallinity; Raman spectroscopy and Fourier-Transform Infrared spectroscopy measure material phonon spectra; and X-ray photoelectron spectroscopy detects local bonding structures and oxidation states. All these tools directly probe glass structure. In addition, measuring glass properties can indirectly infer structural modifications, and the examples include thermal analysis, mechanical property testing, viscosity measurement, and refractometry. Refractometry measures optical properties of glasses (refractive index and absorption coefficient), and is thus of particular relevance to photonic device design and application. Currently, refractometry are usually conducted using ellipsometer, prism coupler or optical interferometry²¹. The detection limits of the aforementioned refractometry tools are typically in the order of 10^{-3} refractive index unit (RIU) and can be down to 10^{-4} RIU in certain scenarios²²; further, the wavelength choices of these measurements is often limited by the availability of laser sources. Alternatively, transmission/reflectance spectra fitting techniques such as the Swanepoel method²³ or multilayer fitting²⁴ provides optical data over a wide wavelength range with limited accuracy ($n \sim 0.01$). Since the refractive index change in glasses can be exceedingly small (e.g. in the case of sub- T_g relaxation in a short time scale of < 1 year), the current refractometry techniques still cannot fulfill the need for accurate characterization of glass structural evolution kinetics.

In this thesis, we will present a resonator cavity refractometer we developed (Chapter 9). This technique enables sensitive detection of refractive index changes down to 10^{-7} RIU, and optical absorption coefficient down to 10^{-4} dB/cm. We will also demonstrate the first applications of this technique to characterizing structural relaxation (aging) and photosensitivity in chalcogenide glasses.

Chapter 2. Chalcogenide glass materials

Chalcogenide glasses (ChG's) are amorphous compounds of chalcogens (sulfur, selenium and/or tellurium) with other metal or non-metal elements. The common elements contained in chalcogenide glasses include arsenic, germanium, antimony, gallium, lanthanum etc. There has been a recent surge of interest in these glass materials both from the academia and from the industry, largely due to its excellent optical properties in the infrared. In this chapter, I review the basic properties of chalcogenide glasses with an emphasis on their optical properties. I also seek to provide the motivation we use these glass materials for our research and the targeted applications.

2.1. Structure of chalcogenide glasses and network rigidity

Similar to their oxide counterparts such as silica, chalcogenide glasses are typified by a network structure that lacks long-range order. Such a disordered network can be described using different models and characterized by a number of structural parameters.

Reduced radial distribution function (RDF), which gives the atomic density variation as a function of the distance from a particular atom, is a commonly used structural function for describing amorphous solids²⁵. Whereas RDF is generally considered effective in describing the structures of non-covalent amorphous solids such as metallic glasses, it is criticized for overlooking the geometrical connection between neighboring atoms, a connection arising from the directional nature of covalent bonds. An alternative model based on glass network topology and the concept of local clusters has been proposed and used for analyzing oxide and chalcogenide glass structures²⁶.

Alternatively, if we neglect the network details of its constituent atoms, a number of general conclusions can be drawn simply based on a geometrical consideration using mean-field constraint counting procedures^{27,28}. An important conclusion is the presence of a rigidity percolation threshold at a mean coordination number $\langle r = 2.4 \rangle$: when the average coordination number in a glass is smaller than 2.4, the glass network is under constrained and “floppy”, a case when the glass is often called “polymeric glass”; on the other hand, when the mean coordination number is greater than 2.4, the whole network is rigid and the floppy regions can only form isolated islands in the glass, a case when the glass is considered “amorphous solid”.

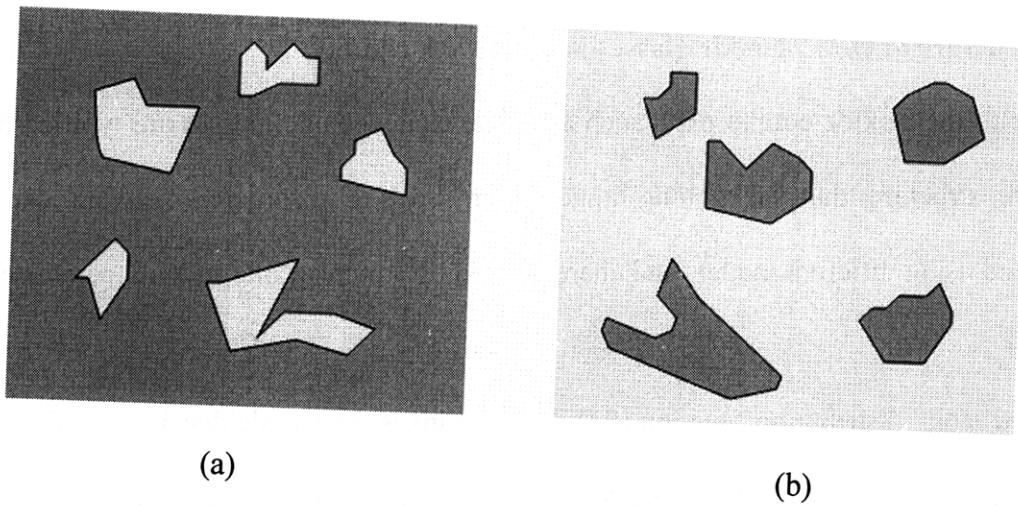


Figure 3 Schematic illustrations of glass structural regions following M. Thorpe²⁸ in (a) an amorphous solid, where the floppy regions are surrounded and separated by rigid regions; and (b) a polymeric glass, where the rigid regions form isolated islands in a floppy network matrix. The light blue areas denote the floppy regions and the grey areas represent the rigid regions in glass network.

If we apply the network rigidity theory to the two glass composition commonly used in this thesis research, As_2S_3 and $\text{Ge}_{23}\text{Sb}_7\text{S}_{70}$, we obtain a mean coordination number of 2.4 for As_2S_3 and $\langle r = 2.53 \rangle$ in the case of $\text{Ge}_{23}\text{Sb}_7\text{S}_{70}$. The network rigidity, along with the

high bonding energy between germanium and sulfur (534 kJ/mol for the Ge-S bond and 379.5 kJ/mol for the As-S bond²⁹), lead to the higher glass transition temperature (T_g) in $\text{Ge}_{23}\text{Sb}_7\text{S}_{70}$ ($T_g \sim 310$ °C) as compared with that of As_2S_3 ($T_g \sim 200$ °C). This distinction also underlies the different applications of the two glass compositions in this thesis research: $\text{Ge}_{23}\text{Sb}_7\text{S}_{70}$ is chosen mostly for sensing applications given its high T_g and hence much slower structural relaxation, whereas As_2S_3 is a good model material system for studying structural modifications induced by environmental changes (light illumination, heat, etc.).

2.2. Density of states and electrical conduction

Besides their applications as optical materials, chalcogenide glasses are also considered as amorphous semiconductors. According to the Mott-Davis model³⁰, amorphous semiconductors exhibit non-vanishing density of state (DOS) within their mobility gap due to localized states. A traditional way of categorizing these localized states within the mobility gap divide these states into two classes: the band tail states (Urbach tail) and the mid-gap states usually formed due to dangling bonds. The Urbach tail is believed to be the consequence of long-range disorder in amorphous semiconductors.

Distinctive from another type of well-studied amorphous semiconductor, amorphous silicon (a-Si), the dangling bonds in chalcogenide glasses are doubly charged, i.e. the following reaction is energetically favorable in chalcogenide glasses: $2D^0 \leftrightarrow D^+ + D^-$ (two singly charged dangling bond states spontaneously convert to one doubly charged state and one empty state). Formation of such defect pairs leads to two experimental

observations: 1) absence of electron spin resonance signal from chalcogenide glasses; 2) pinning of Fermi level near mid-gap³¹.

On the electrical conduction mechanism side, these mid-gap states contribute to hopping conduction mechanism besides extended state conduction due to thermally excited carriers in the conduction and valence bands. The commonly accepted theory about hopping conduction is proposed by Mott, the so-called variable range hopping (VRH) conduction³². In this model, conduction takes place via carrier tunneling between localized states. According to this model, the tunneling probability is proportional to the overlap of electron wave functions in the two localized states involved in the tunneling process, as well as the Boltzmann factor that scales with the energy difference between them (in the case of hopping from a low energy site to a high energy site which requires absorption of a phonon):

$$\text{Eq. 1: } \Gamma_{ij} \sim \langle n_i(1 - n_j)\gamma_{ij} \rangle$$

where Γ_{ij} represents the tunneling probability from the localized site i to another site j , n_i and n_j denote the probability of the site i and j being occupied by an electron (i.e. the Fermi-Dirac distribution), respectively, and γ_{ij} is the product of the wave function overlap and thermalization factor, which according to Miller-Abrahams writes³³:

$$\text{Eq. 2: } \gamma_{ij} = \frac{\gamma_0 \exp(-2\alpha R_{ij} - (E_j - E_i)/k_B T)}{\gamma_0 \exp(-2\alpha R_{ij})}$$

where α is the mean decay length of electron wave function in the localized sites, R_{ij} the spatial separation between the sites, E_i and E_j correspond to the energy of the sites i and j , respectively, k_B the Boltzmann constant and T the temperature of the semiconductor. The

first equality holds when the energy of site i is lower than that of site j , in which case the tunneling is actually phonon assisted to preserve energy conservation, and in this case the Boltzmann factor is actually an approximation of the Bose-Einstein distribution function that gives the probability of finding a phonon with the energy $(E_j - E_i)$. In the case of $E_j < E_i$, however, the tunneling process is accompanied with phonon emission and the probability of emission is considered unity.

The simplistic way to deriving conductivity inside an amorphous semiconductor is then to maximize the probability of hopping as is shown in Eq. 2 with respect to temperature. Assuming a constant DOS near the Fermi level, such an optimization process yields the following temperature dependence of hopping conductivity σ :

$$\text{Eq. 3: } \sigma = \sigma_0 \exp\left(\frac{T_0}{T}\right)^{-1/4}$$

the well-known $-1/4$ temperature dependence law for VRH. In this equation, the characteristic temperature T_0 is given by:

$$\text{Eq. 4: } T_0 = \frac{16\alpha^3}{k_B N(E_F)}$$

where $N(E_F)$ represents the DOS near the Fermi level.

The VRH model allows the determination of amorphous semiconductor band parameters by measuring the temperature dependence of electrical conductivity. According to the discussions by Ambegaokar et al.³⁴ and Paul et al.³⁵, electron localization parameter α and density of states near Fermi energy $N(E_F)$ can be calculated using:

$$\text{Eq. 5: } \alpha (cm^{-1}) = \left(\frac{21.22 \times 10^{13}}{\nu_{ph}^3} \right) \sigma_0 T^{1/2} T_0^{1/2}$$

$$\text{Eq. 6: } N(E_F)(cm^{-3}eV^{-1}) = \frac{1.996 \times 10^{48}}{\nu_{ph}} (\sigma_0 T^{1/2})^3 T_0^{1/2}$$

where $\sigma_0 T^{1/2}$ is the intercept of $\ln(\sigma T^{1/2})-T^{-1/4}$ curve, T_0 is the characteristic temperature defined in Eq. 3 and ν_{ph} is the characteristic phonon frequency taken as 10^{12} Hz, a typical value in amorphous materials³⁶. It turns out that due to the over simplified assumptions in Mott's VRH theory, Eq. 6 often significantly overestimates the DOS near Fermi level. Therefore, an alternative approach has been suggested that Eq. 4 can be used to extract the value of $N(E_F)$ by assuming $\alpha \sim (10\text{\AA})^{-1}$ (a value comparable to a few atomic spacings in glasses)³⁰. Although this approach gives DOS relatively close to physically viable values, it is still a slight underestimation of the DOS near Fermi level. Nevertheless, $N(E_F)$ estimated from Eq. 6 still provides a good measure of DOS near Fermi level in amorphous semiconductors.

A more accurate description of hopping conduction is based on the percolation theory, by considering the localized states as lattice sites on a percolation network³⁷, where the hopping probability between the lattice sites is given by Eq. 2. The VRH theory has been extended to account for non-uniform DOS using such percolation formalism. Alternatively, Monte-Carlo simulations using such a percolation network concept have also been employed to quantitatively evaluate the inadequacies of the simplistic VRH theory³⁸. Here I also would like to call for attention to the discussion on the VRH theory by J. Marshall³⁸, which highlights the limitations of the simplistic VRH formalism.

2.3. Optical transparency

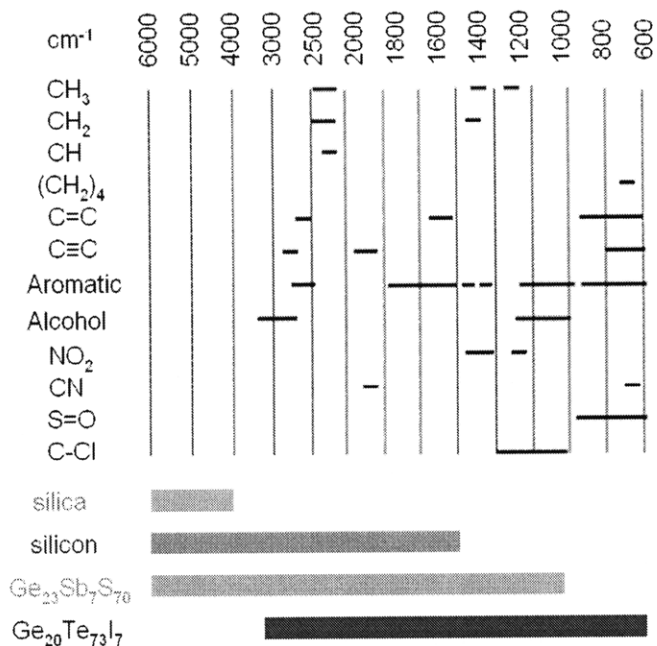


Figure 4 Top figure shows the infrared absorption overtones of some common chemical species, represented by the horizontal lines [9]; the bars in the bottom figure denote the optical material transparency window (defined as wavelength range where the material loss < 2 dB/cm) of IR grade fused silica, silicon³⁹, as well as two chalcogenide glass compositions $\text{Ge}_{23}\text{Sb}_7\text{S}_{70}$ and $\text{Ge}_{20}\text{Te}_{73}\text{I}_7$ ⁴⁰. The two figures are aligned in wave numbers to facilitate comparison. It is clear the optical transparency window of chalcogenide glasses covers most of the infrared molecular absorption bands.

Chalcogenide glasses are well-known for their excellent optical transparency in the infrared wavelength range. Compared to their oxide counterparts, chalcogenide glasses constitute of heavier atoms and therefore the phonon absorption edge is significantly red shifted. Figure 4 compares the infrared transparency in several glasses and semiconductors, along with the infrared spectra of a model chemical we have been working with, N-methylaniline. The wide infrared transparency window of chalcogenide glasses covers the characteristic absorption wavebands for most molecules of interest. A

property that makes these glasses an ideal material candidate for infrared chemical sensing.

More detailed analysis of the optical transparency in chalcogenide glasses necessarily involves investigating the loss mechanisms in these glasses. Three types of mechanisms contribute to intrinsic optical losses in glasses (in contrary to extrinsic loss caused by impurities): electronic absorption, Rayleigh scattering, and bond vibrational absorption (phonon scattering absorption). Following T. Tanabe et al.⁴¹, the intrinsic material loss can be written as the summation of these different loss contributions:

$$\text{Eq. 7: } \alpha_i = A / \lambda^4 + B_1 \exp(B_2 / \lambda) + C_1 \exp(C_2 / \lambda)$$

The first term represents contributions from Rayleigh scattering, i.e. scattering due to density fluctuations and hence refractive index spatial variations in glass. Thermodynamic analysis yields the Rayleigh coefficient A as⁴²:

$$\text{Eq. 8: } A \approx \frac{8}{3} \pi^3 n^8 p^2 \beta k_B T_F \approx \frac{8}{3} \pi^3 (n^2 - 1)^2 \beta k_B T_F$$

where n is the glass refractive index, p is the photoelastic constant, β denotes isothermal compressibility, k_B is the Boltzmann constant and T_F the Fictive temperature. B_1 , B_2 , C_1 , and C_2 in Eq. 8 are material constants that can be experimentally determined from precision spectroscopic measurements.

2.4. Photosensitivity and other photo-induced transformations

An important characteristic of chalcogenide glasses is their photosensitivity, in particular, light with photon energy close to their optical band gap. Usually photosensitivity refers to photo-induced refractive index modification in these glasses, a process which is often

connected to optical band edge shift and hence absorption change, as is dictated by the Kramers-Kronig relation. The optical band edge shift is named “photodarkening” in the case of a band edge red shift and “photobleaching” in the case of a blue shift. Photosensitivity to near-band gap light illumination in chalcogenide glasses has been extensively investigated^{43, 44, 45, 115} and widely exploited for photonic device fabrication^{46, 47, 113}. Photosensitivity is most prominent under near-band gap illumination; for light with photon energy much greater than glass band gap, the optical absorption takes place within a very small thickness on the surface, and the spatial extent of such change is thus very limited. On the other end, report on photosensitivity at wavelengths much longer than the band edge (e.g. 1550 nm telecommunication wavelength for As_2S_3 glass) is scarce to date⁴⁸ largely due to the much weaker interaction between glass and photons with energy well below its optical band gap and the lack of sensitive characterization techniques. We will be reporting the first discovery of cavity enhanced photosensitivity of As_2S_3 glass to 1550 nm telecommunication wavelength light in Chapter 9.

Besides photo-induced index change, a large amount of other photo-induced material transformation phenomena are also present in chalcogenide glasses. Examples of such photo-induced phenomena include photo-fluidity⁴⁹ (viscosity change under illumination), photo-induced anisotropy⁵⁰ and photo-induced phase transformation⁵¹. A review of these photo-induced phenomena in chalcogenide glass is provided by K. Tanaka⁵².

2.5. Kerr nonlinearity, two photon absorption and magneto-optical properties

Chalcogenide glasses have attracted increasing interest for their high Kerr nonlinearity (3rd order optical nonlinearity) and low nonlinear absorption in the telecommunication wavelengths, and therefore they hold promise for ultra-high-bandwidth all-optical signal processing⁵³. An example of such an application is the recently demonstrated all-optical spectrum analyzer with terahertz bandwidth⁵⁴.

A simple and empirical way to estimate the Kerr nonlinearity in glasses is given by the Miller's rule⁵⁵:

$$\text{Eq. 9: } \chi^{(3)} \sim [\chi^{(1)}]^4 \cdot 10^{-10} \text{ esu}$$

where $\chi^{(3)}$ and $\chi^{(1)}$ denote the third-order and first-order (linear) susceptibility, respectively. According to Miller's rule, high refractive index glasses, such as chalcogenide glasses, can exhibit nonlinear refractive index (n_2) values more than two orders of magnitude higher compared to silica glass. Unlike semiconductors which derive a large fraction of their 3rd order nonlinearity from free electrons with a time scale comparable to their carrier lifetime (\sim ns), the origin of such Kerr nonlinearity in chalcogenide glasses is associated with electronic processes with an ultra-short time scale typically < 50 fs⁵⁶. Measurements have shown that the nuclear contribution to the optical nonlinearity for chalcogenide glasses is approximately 12 ~ 13%⁵⁷. The ultra-fast Kerr nonlinearity in chalcogenide glasses forms the basis for high-bandwidth optical signal processing using these glass materials.

In addition to nonlinear refractive index change (Kerr nonlinearity), nonlinear absorption processes can occur in chalcogenide glasses as well, which involves absorption of multiple photons to excite an electron-hole pair. This is the so-called multi-photon absorption process or more generally referred to as nonlinear absorption. The lowest order effect, two photon absorption (TPA), leads to additional optical loss besides the linear attenuation described in section 2.3. In the presence of TPA, the optical attenuation in glass can be written as:

$$\text{Eq. 10: } \frac{dI}{dz} = -\alpha I - \alpha_2 I^2$$

where α is the linear optical attenuation coefficient, I represents the optical power density (e.g. in W/cm^2) as a function of the propagation distance z , and α_2 is the TPA coefficient usually given in m/W . In crystalline semiconductors, free carriers generated by TPA can also contribute to optical loss in the form of free carrier absorption, a loss mechanism that is much reduced in glasses due to the small carrier mobility in an amorphous network.

From a nonlinear optical device perspective, TPA leads to increased device insertion loss penalty. Therefore, a nonlinear figure-of-merit (FOM) is often used to enable quantitative performance comparison between different optical nonlinear materials:

$$\text{Eq. 11: } FOM \propto \frac{n_2}{\alpha_2}$$

Note that the specific form of FOM definition may vary depending on the citing source. Chalcogenide glasses exhibit high Kerr nonlinearity as well as low TPA, which makes them a preferred material choice over traditional semiconductors for nonlinear optical

applications. For example, the nonlinear FOM in As₂S₃ glass can be over 20 times that of silicon⁵⁸, mainly due to the negligible TPA in As₂S₃ glass (see Chapter 9).

Magneto-optical properties of chalcogenide glasses have also been investigated⁵⁹. The Verdet constant of these glasses at telecommunication wavelengths is much higher compared to silica glass. This observation can be semi-quantitatively explained by invoking the Becquerel formula:

$$\text{Eq. 12: } V_e = \frac{e}{2mc^2} \lambda \frac{dn}{d\lambda}$$

where V_e is the Verdet constant, λ is the light wavelength, c represents light velocity, e and m denote the electron charge and mass, respectively. This formula correlates the Verdet constant of a material with its chromatic dispersion at the wavelength under investigation. Verdet constant exceeding 0.05 min/G·cm has been experimentally measured in Ge₃₃As₁₂Se₅₅ glass at 1550 nm wavelength.

2.6. Planar chalcogenide photonic device fabrication techniques

The conventional technology of fabrication planar photonic structures in chalcogenide glasses takes advantage of their photosensitivity. In a typical waveguide fabrication process, the light guiding region of a planar optical waveguide is formed through photo-induced index increase⁶⁰. Since the light exposure can be performed through a commercially available photomask, this photosensitive fabrication process is conceptually and practically simple and inherently low-cost.

A variation of the simple photosensitive waveguide fabrication process is femtosecond laser direct writing. Basically, femtosecond laser direct writing utilizes the interaction of ultra-short laser pulses with chalcogenide glasses and hence the induced material modifications (index change or ablation) to create the desired features⁶¹. Compared to waveguides fabricated using traditional photolithography and etching, laser-written waveguides are low-index contrast and hence often exhibit relatively low propagation loss, typically ~ 0.1 to 1dB/cm in unpurified chalcogenide glasses⁶². As an example, Figure 5 show (a) A straight channel waveguide, and (b) a waveguide Y-splitter written in As_2S_3 glass film. Waveguides can be written in two distinctive modes: transverse mode, in which the sample is translated in a direction perpendicular to the laser beam and longitudinal modes, in which the sample is translated along the direction of laser beam. The former is considered more useful for planar microphotronics, since planar waveguides can only be defined in this configuration. An important advantage of direct laser writing lies in its ability to create complex 3-d structures. When a laser pulse is focused through an optical lens with large numerical aperture, the laser-matter interaction can be confined spatially to a very small range within the focal point of the lens, either on material surface or inside a volume of materials. By adjusting the position of the focal point, complicated 3-d structures can be directly written with high accuracy. Intrinsically a beam-based method, femtosecond laser direct writing is highly flexible and versatile; nevertheless, just as other beam-based fabrication methods such as electron beam lithography, the application of femtosecond laser direct writing for mass production is limited by its low throughput compared to batch processes such as lift-off and plasma etching.

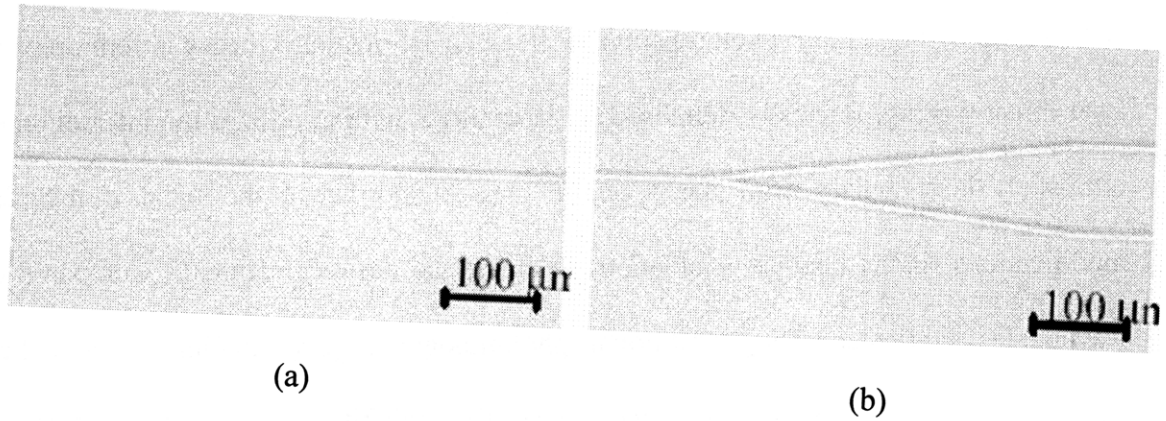


Figure 5 (a) A straight channel waveguide and (b) a waveguide Y-splitter written using transverse configuration in As_2S_3 glass film⁶²

Both photosensitive fabrication and femtosecond laser direct writing leads to photonic devices with low index contrast (core-cladding index difference $\Delta n < 0.1$). Plasma etching, a commonly used patterning technique in microelectronics, can also be applied to pattern chalcogenide glass films, which enables the creation of high-index-contrast photonic structures. By using a large rib waveguide cross-section to minimize modal overlap with sidewall roughness, optimized plasma etching process yields chalcogenide glass waveguides with optical loss down to 0.05 dB/cm^{63} . However, the large rib design is not applicable to sensing applications since the optical mode is almost completely confined with the waveguide core, leaving little evanescent field for interaction with molecular species to be detected.

2.7. Why chalcogenide glass?

Chalcogenide glasses exhibit unique optical properties attractive for both refractometry biological sensing and infrared absorption spectroscopic chemical sensing. Their high refractive index facilitate planar integration and low cost mass production; the amorphous

nature of chalcogenide glasses allows their monolithic integration on a silicon platform via low-cost deposition techniques such as evaporation and sputtering; their amorphous nature also enables a thermal reflow process for optical loss reduction (Chapter 4) and hence sensitivity improvement.

Specific to the refractometry biological sensing application, intrinsically these glasses exhibit low optical loss in near infrared where water is also optically transparent; this is important since most biological reactions occur in an aqueous environment. The thermo-optic coefficient of chalcogenide glasses lies in the range between 10^{-5} K^{-1} and 10^{-4} K^{-1} ; as we will see in Chapter 6, such a range of thermo-optic coefficient is appropriate for creating refractometry sensors minimally affected by temperature fluctuations.

The transparency of chalcogenide glasses to mid-infrared and far-infrared wavelengths justifies their application as chemical sensor materials. Further, their almost unlimited capability for compositional alloying and property tuning provide immense flexibility for device design and fabrication.

Chapter 3. Optical resonators

An optical resonator is often alternatively termed “optical cavity”, “micro-cavity” or “resonant cavity”. When light is launched into an optical resonator, the optical wave can interfere constructively and oscillates at certain optical wavelengths (frequencies), called “resonant wavelengths (frequencies)”. When the resonant condition is met, the optical power becomes resonantly enhanced inside the resonator, making optical resonators an ideal device platform for both fundamental investigations and practical applications based on photon-matter interactions. The examples include all-optical switching, light emission, nonlinear optics, and biochemical sensing. In this chapter, we will provide an overview on the fundamental device physics of optical resonators.

From an electromagnetism perspective, solving the Maxwell’s equations with a given resonator dielectric configuration leads to a set of discrete eigensolutions (in the case of a perfectly lossless resonator) called the “modes” of the resonator. Each solution or mode also corresponds to a unique pattern of electrical and magnetic fields in the resonator.

3.1. Basic resonator configurations

Optical resonators are usually categorized into two types: standing wave resonators and traveling wave resonators. Roughly speaking, in a standing wave resonator, the optical resonant mode has a field momentum close to zero, while in a traveling wave resonator, the resonant mode circulates inside the resonator and possesses non-vanishing momentum. Simply put, in integrated photonics, standing wave resonators often feature small mode volume and high finesse, and thus they are suitable for applications that

require high field density, such as nonlinear optics and optical trapping. By comparison, traveling wave resonators boast superior fabrication tolerance and higher cavity quality factor (Q-factor), making them ideal for biochemical sensing and optical filtering.

3.1.1. Standing wave resonators

The simplest form of a standing wave resonator, a Fabry-Perot cavity, is comprised of two mirrors facing each other. When integral multiples of the wavelength of light equals the resonator length, the resonant condition is met and light can interfere constructively while reflecting back and forth between the two mirrors, and thus creating a standing wave pattern between the two mirrors.

In integrated photonics, standing wave resonators often take the form of a Bragg cavity stack or a point defect in a 2-d photonic crystal slab. The major advantage of both types of resonators is the tight optical confinement within a small physical volume, and hence the strong field enhancement effect. The degree of optical confinement inside a resonator can be characterized by its mode volume, often defined as the equivalent volume the mode occupies if the energy density was distributed homogeneously at the peak value:

$$\text{Eq. 13: } V_m = \frac{\int_v |E|^2 dV}{|E_{\max}|^2}$$

where E is the mode field profile, E_{\max} is the peak value of electric field, and the integration takes place inside the resonator (without taking into account the evanescent wave). The small mode volume of these standing wave resonators make them ideal for applications that require high field intensity, such as nonlinear optics and optical trapping. However, a Bragg cavity stack offers only one-dimensional confinement of the field and

often requires coupling to free space optics. A point defect cavity in a 2-d photonic crystal slab, on the other hand, is considered highly sensitive to fabrication errors and often poses a major challenge to fabrication tolerance control. In addition, despite its small mode volume and high finesse, its cavity quality factor is often inferior to traveling wave resonators (micro-rings or micro-disks) under the same set of fabrication conditions, due to the intrinsic optical leakage from a photonic crystal with non-perfect periodicity (even though high Q-factor can be achieved in 2-d photonic crystal cavities via appropriate cavity design⁶⁴, it is still several orders of magnitude inferior compared to ultra-high-Q micro-spheres⁶⁵).

3.1.2. Travelling wave resonators

Instead of forming a standing wave pattern, light circulates inside a traveling wave resonator at optical resonance. Examples of traveling wave resonators include micro-rings, micro-disks, micro-spheres and micro-toroids⁶⁶. In these resonators, the resonant condition is defined by:

$$\text{Eq. 14: } \lambda_r = \frac{n_{\text{eff}}L}{N}, N \in Z^+$$

where λ_r denotes the resonant wavelength, n_{eff} is the modal effective index, L is the circumference of the resonator, and N is an integer sometimes called the resonance order or mode order.

3.2. Optical parameters characterizing a resonator

Besides its resonant wavelength λ_r , a resonator is often characterized by a set of parameters that represent its resonance properties including free spectral range (FSR),

cavity quality factor (Q or Q-factor), finesse F, and extinction ratio; as well as a set of modal parameters such as effective index n_{eff} and group index n_g . Detailed derivations of the formulae used in this section are presented in Appendix I.

3.2.1. Free spectral range

Free spectral range is defined as the spacing between adjacent resonant wavelengths (or frequencies). The wavelength domain FSR of a travelling wave resonator for high resonance order is given by:

$$\text{Eq. 15: } FSR = \frac{\lambda_r^2}{n_g L} \text{ when } N \gg 1$$

where n_g is the group index defined as:

$$\text{Eq. 16: } n_g = n_{\text{eff}} - \lambda \frac{\partial n_{\text{eff}}}{\partial \lambda}$$

in which λ represents optical wavelength in vacuum. It is worth pointing out that the wavelength domain FSR is not uniform at different wavelengths; however, the FSR of a travelling wave resonator defined in the frequency domain is indeed a constant independent of the frequency.

3.2.2. Cavity quality factor and finesse

The quality factor of a resonator is a measure of effective optical path length inside the resonator. Mathematically, Q is defined as the ratio of the resonator's resonant wavelength (or frequency) against its resonant peak full-width-at-half-maximum (FWHM):

$$\text{Eq. 17: } Q = \frac{\lambda_r}{\Delta\lambda_{FWHM}}$$

Since the Q-factor is correlated to optical loss, we can decompose the cavity Q-factor into factors arising from different loss contributions:

$$\text{Eq. 18: } \frac{1}{Q} = \frac{1}{Q_{in}} + \frac{1}{Q_{ex}} = \frac{1}{Q_{abs}} + \frac{1}{Q_{sca}} + \frac{1}{Q_{rad}} + \frac{1}{Q_{ex}}$$

where Q_{in} is the intrinsic Q-factor taking into account only optical loss due to the resonator itself, and Q_{ex} gives the Q-factor due to optical coupling (e.g. to an optical waveguide) and hence power leakage into the external world. Further, the intrinsic Q can be separated into contributions from material attenuation (Q_{abs}), scattering loss (Q_{sca} , usually resulting from Rayleigh scattering from surface roughness), and modal radiative loss mechanisms (Q_{rad} , e.g. due to bending, optical leakage into substrate or modal mismatch at junctions). A complete quantitative description of these loss mechanisms is given by M. Borselli et al.⁶⁷

Another parameter related to cavity Q-factor is cavity finesse F , defined as the ratio between FSR and the resonant peak FWHM:

$$\text{Eq. 19: } F = \frac{FSR}{\Delta\lambda_{FWHM}}$$

Finesse is directly correlated to the optical power enhanced inside a resonator at resonance (neglecting back scattering, see Appendix I):

$$\text{Eq. 20: } G = \frac{F}{2\pi} \cdot (1 - T)$$

where G is the power enhancement factor defined as the power circulating inside a resonator against the power launched in the bus waveguide, and T is the transmission coefficient.

Importantly, both intrinsic Q and intrinsic finesse can be quantitatively related to the equivalent waveguide loss in a critically coupled traveling wave resonator (see Appendix I):

$$\text{Eq. 21: } Q_m = \frac{2\pi n_g}{\alpha \lambda_r}$$

$$\text{Eq. 22: } F_m = \frac{2\pi}{\alpha L}$$

where α denotes the equivalent waveguide loss in the traveling wave resonator given in an inverse length scale (e.g. cm^{-1}). These important relations provide a way to directly determine optical loss in waveguides simply by measuring the transmission spectrum of an optical resonator.

3.2.3. Extinction ratio and coupling regimes

Extinction ratio is defined as the peak power extinction at optical resonance when light passes through a resonator. In the most simple traveling wave resonator configuration with one bus waveguide coupled to one single-mode resonator (neglecting back reflection), extinction ratio is completely determined by the intrinsic Q and extrinsic Q of the resonator. A straightforward derivation of the quantitative relation between extinction ratio and the two Q -factors is based on a generalized coupling matrix formalism⁶⁸, which can be proven to be mathematically equivalent to the coupled mode theory⁶⁹. Notably,

this relation is also the basis of optical waveguide loss measurement using ring resonators which does not necessarily require the condition of critical coupling to be met⁷⁰.

The relative magnitude of intrinsic and extrinsic Q-factors demarcates the resonator operation into three distinctive regimes: under coupling when $Q_{in} > Q_{ex}$, critical coupling when $Q_{in} = Q_{ex}$, and over coupling when $Q_{in} < Q_{ex}$ (note that the definition of coupling regimes is slightly different in the case of one resonator coupled to two bus waveguides, where critical coupling is achieved when the input coupling loss equals the sum of intrinsic loss and output coupling loss). Critical coupling is featured by zero optical transmission at the resonant wavelength, whereas the transmission intensity is non-vanishing in the other two regimes. Figure 6 gives an example of the transmission spectra evolution of a micro-ring resonator as the extrinsic Q-factor Q_{ex} increases and the resonator evolves from under coupling (the green curve) to over coupling (the red curve).

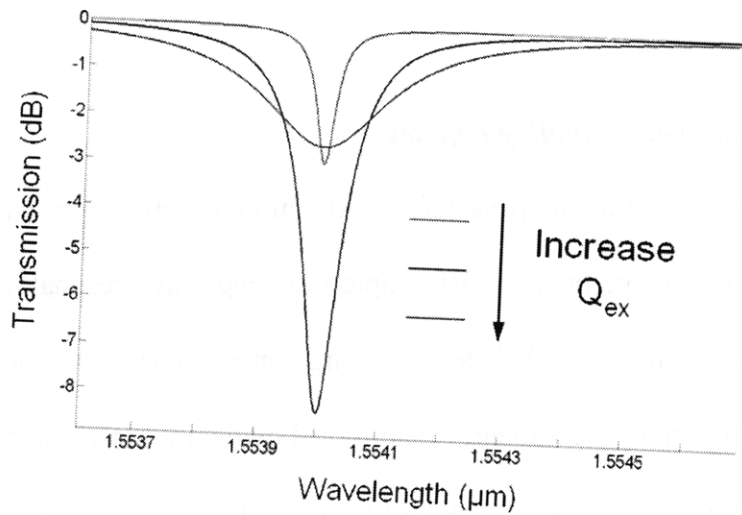


Figure 6 Transmission spectra evolution of a micro-ring resonator coupled to one bus waveguide as a function of extrinsic Q-factor Q_{ex} ; the spectra are simulated using the coupling matrix approach.

3.3. Experimental characterization of optical resonators

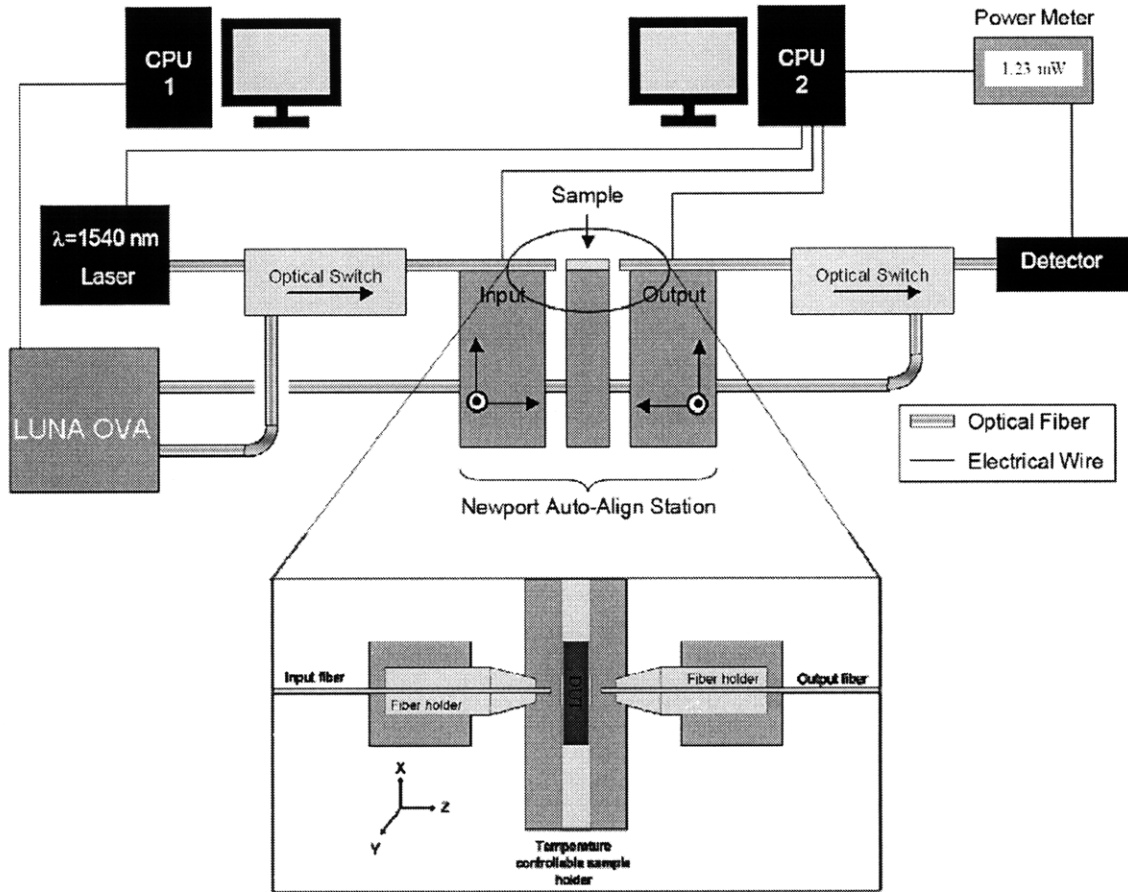


Figure 7 Schematic diagram of a Newport Autoalign station. The bottom is the top view of the sample stage and fiber holders where light is coupled from fiber to the device under test (Courtesy of Dr. Daniel K. Sparacin).

In our experiments, the transmission spectra of a resonator is measured on a Newport AutoAlign workstation in combination with an Hewlett-Packard 8164 external cavity tunable laser. The output state of light is then analyzed by an optical vector analyzer (LUNA Technologies, Inc.). Figure 7 shows the Schematic diagram of the measurement setup. Reproducible coupling is achieved via the AutoAlign system, which comprised of two 4-degree-of-freedom motors capable of automatically locate the fiber position corresponding to maximum transmitted power with a spatial resolution of 50 nm. Lens-

tip fibers are used to couple light from the laser into and out of the devices. The sample is mounted on a temperature-controllable thermostat stage.

A single wavelength alignment laser is first used to align the fiber-to-waveguide coupling, and then the optical path is switched to tunable laser and conduct wavelength sweep measurement. The optical vector analyzer is capable of measuring, not exclusively: (1) insertion loss, (2) polarization dependent loss, (3) group delay, (4) chromatic dispersion, optical phase, and (5) polarization mode dispersion as a function of wavelength. The light output state analysis by the optical vector analyzer is carried out using a Jones matrix method⁷¹. The measured transmission spectra (insertion loss of a particular polarization) can then be used for subsequent analysis.

3.4. Applications

Optical filters often take advantage of the spectral selective transmission characteristic of resonators⁷². Similarly, all-optical switching has been realized leveraging on the same property of resonators⁷³. The strong optical field enhancement at resonance makes resonators an ideal platform for nonlinear optics⁷⁴ and optomechanics⁷⁵. Resonators are also known to be capable of modifying the accessible modes to an oscillating dipole (Purcell effect), a property useful for light emission and lasing⁷⁶. The long optical path length in a high-Q resonator renders their extreme sensitivity to refractive index and absorption change of its constituent materials, the cornerstone of biochemical sensor applications we will describe in detail in this thesis.

Chapter 4. Processing development for planar chalcogenide glass devices

4.1. Bulk glass preparation and glass film deposition

Bulk glass is prepared from high purity elements using a traditional chalcogenide melt-quenching technique^{43, 84, 86}. Figure 8 shows the schematic procedures of glass bulk preparation.

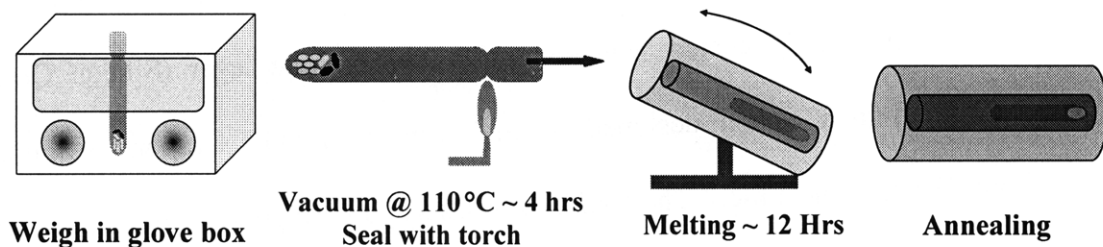


Figure 8 Schematic procedures of glass bulk preparation

The glasses were melted from high purity elements (As: Alfa-Aesar 99.999% Ge: Sigma-Aldrich 99.999%, Sb: Alfa-Aesar 99.999% and S: Cerac 99.999%). Notably, despite the stated purity, species which contribute to extrinsic absorption (trace impurities, hydrides, etc.) are still present which results in an unpurified starting material. No purification procedures were carried out during this study. All loss data in this thesis are measured in films deposited using the unpurified bulk glass. Prior to sealing and melting, the ampoule and batch were pre-heated to 100°C, while under high vacuum, for 4 hours to remove surface moisture from the quartz ampoule and the batch raw materials. The ampoule was then sealed with a gas-oxygen torch while still under vacuum and heated to usually

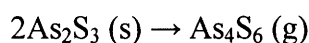
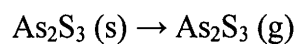
between 600 and 925 °C for 15 hours. The melting temperature is dependent on the specific glass composition. A rocking furnace was used during melting in order to increase the homogeneity of the melt. Once fully homogenized, the melt-containing ampoule was quenched in air to room temperature. To avoid fracture of the tube and glass ingot, the ampoules were subsequently returned to the furnace for annealing for 15 hours at 40 °C below the glass transition temperature (T_g). Bulk glasses were then cut polished and optically examined for homogeneity.

The bulk glass is grounded into powder in an agate mortar and then thermally deposited onto 6" Si wafers already coated with a 3 μm thermal oxide layer (Silicon Quest International Inc.) in a custom-designed thermal evaporator (112 Evaporator-Sputter Station from PVD Products Inc.). The film is deposited at a base pressure of 2×10^{-7} Torr using an alumina coated Tantalum baffled source, and the deposition rate is stabilized at 18 $\text{\AA}/\text{s}$. A surplus of starting glass materials is loaded into the boat (usually far exceeding that required for the target film thickness) to minimize composition non-uniformity across the film thickness. The Si substrate is mounted on a thermostat stage and is maintained at room temperature throughout the deposition process. The substrate-source distance is approximately 80 cm to guarantee good thickness uniformity across an entire substrate.

We investigate the structure and property change in the transition from bulk glass to thin film using a combination of composition analysis, Raman spectroscopy, optical

transmission and thermal analysis. Summarized here are the key findings in the two main glass compositions we employ in our applications, As_2S_3 and $\text{Ge}_{23}\text{Sb}_7\text{S}_{70}$.

Thermally evaporated As_2S_3 films are found to be stoichiometric within the measurement accuracy ($\sim 1\%$) of wavelength dispersive spectroscopy (WDS) using an electron microprobe. In the As_2S_3 thermal evaporation process, several molecular species are found in the vapor phase according to previous reports^{77, 78, 79}. The exact composition of the vapor phaser, however, seems to be highly dependent on the vaporization condition and thus considerable disagreement between the different reports exists. According to B. Kuadzhe et al., when As_2S_3 evaporates at temperatures lower than its melting point, two main reactions take place in the vaporization process:



Another reaction possible contributing to this process is⁷⁸:



Our deposition temperature is slightly lower than the melting temperature of As_2S_3 estimated using the vapor pressure of As_2S_3 (deduced from the deposition rate). Therefore, we expect major contributions from congruent sublimation of As_2S_3 in the gas phase and hence the stoichiometric film. The presence of As_4S_4 molecule is evident from our Raman spectroscopic studies, as the thermally evaporated films show significantly increased As_4S_4 unit as compared to As_2S_3 glass bulks. This is in agreement with results seen in many prior studies of thermally evaporated As_2S_3 .

In $\text{Ge}_{23}\text{Sb}_7\text{S}_{70}$, the addition of four-fold coordinated Ge increased connectivity of the glass network and the average bond energy, as is reflected by the increased T_g of $\text{Ge}_{23}\text{Sb}_7\text{S}_{70}$ glass. In addition, in a ternary glass such as $\text{Ge}_{23}\text{Sb}_7\text{S}_{70}$, the vaporization process is highly complicated with multiple molecular species contributing. As a consequence of their different equilibrium vapor pressures, the deposited $\text{Ge}_{23}\text{Sb}_7\text{S}_{70}$ films are usually slightly off-stoichiometry, and their exact composition is highly dependent on the deposition conditions. For purposes of maintaining repeatable glass film with reproducible optical and physical properties, deposition conditions in our study were held constant. The ensuing structural and property modifications are discussed in a separate publication⁸⁰. However, no significant composition variation ($< 2\%$) across the film thickness is found within the detection limit of Auger spectroscopy, in the 450 nm thick $\text{Ge}_{23}\text{Sb}_7\text{S}_{70}$ films used in this study.

4.2. Si-CMOS backend-compatible lift-off patterning

As in a standard lift-off process, a photoresist pattern is first formed on a substrate, which is a blank oxide-coated Si wafer in our case. Chalcogenide glass is then thermally evaporated onto the wafer patterned with photoresist, and sonicated in solvent (usually acetone) to dissolve the photoresist layer beneath the undesired parts of the glass film, thus lifting it off. Only glass deposited onto areas not covered by photoresist is retained, and thus a chalcogenide pattern reverse that of the photoresist is defined. The patterned wafer is then rinsed in methanol and isopropanol to clean the surface. To fabricate rib waveguides, a second glass deposition is made sequentially on a lift-off patterned glass

film. A schematic of the process flow and the relevant waveguide dimensions in this study are illustrated in Figure 9.

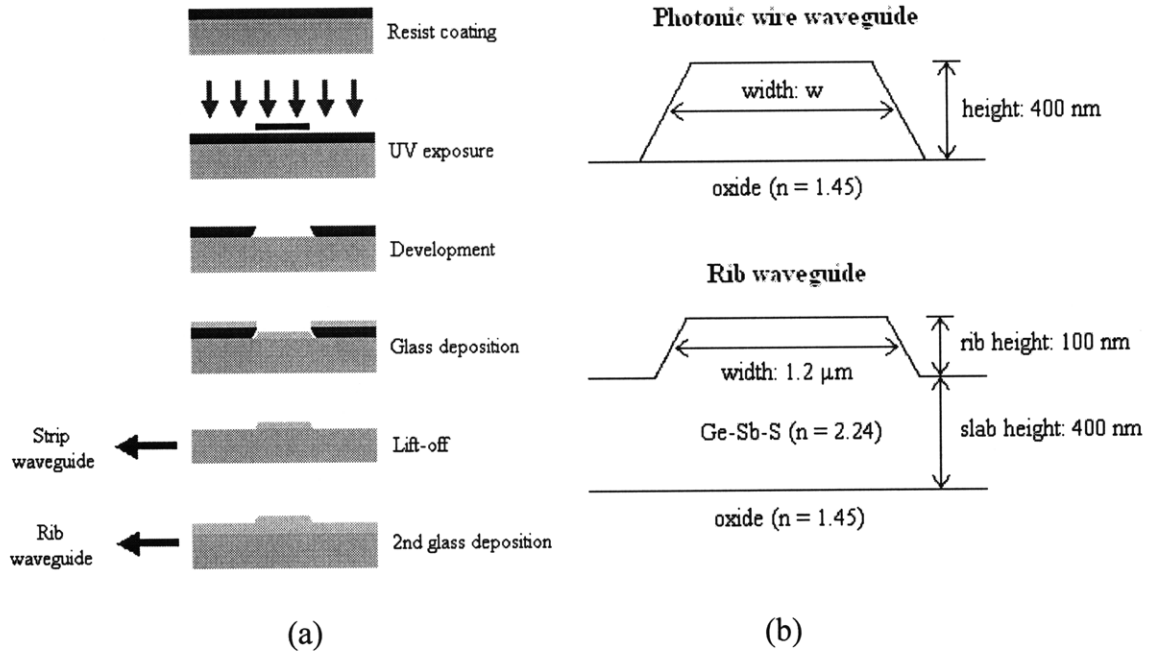


Figure 9 (a) Schematic cross-sectional process flow of chalcogenide glass waveguide fabrication by lift-off; (b) Dimensions of fabricated strip and rib waveguides for this test.

In our process, the starting substrates are 6" Si wafers already coated with a $3 \mu\text{m}$ -thick thermal oxide (Silicon Quest International Inc.). Commercially available negative resist NR9-1000PY (Futurrex Inc.) is used due to its negative-sloping sidewall profile and superior pattern resolution. The resist is spin-coated onto substrates on a manual photoresist coater (Model 5110, Solitec Inc.). UV exposure is carried out using a Nikon NSR-2005i9 i-line wafer stepper (minimum line width of 500 nm). Resist pattern development and subsequent baking are both completed on an SSI 150 automatic photoresist coater/developer track. The entire photolithography process is performed in a class-10 CMOS clean room in the Microsystems Technology Laboratory at MIT. No

additional upper cladding layer is added for two reasons: first, in this study we would like to investigate optical properties that are intrinsic to chalcogenide glass films, so an upper cladding layer which can introduce additional loss due to cladding material absorption is avoided; second, an air-cladded waveguide configuration is appropriate for applications such as chemical and biological sensing, in which direct interaction between the waveguide mode and external environment is necessary.

In order to evaluate the quality of lift-off fabricated waveguides, we performed a series of systematic tests using waveguides fabricated in the $\text{Ge}_{23}\text{Sb}_7\text{S}_{70}$ glass system. The aim of our study is two-fold: to demonstrate lift-off as a novel route of chalcogenide glass film patterning for single-mode, high-index-contrast waveguide fabrication (core sizes are in the submicron range), and to identify the origin of optical loss in such waveguides.

Morphology of $\text{Ge}_{23}\text{Sb}_7\text{S}_{70}$ waveguides has been characterized using a JEOL 6320FV field-emission high-resolution SEM. A Digital Instruments Nanoscope IIIa Atomic Force Microscope (AFM) is used to measure the roughness of the as-patterned $\text{Ge}_{23}\text{Sb}_7\text{S}_{70}$ waveguides. AFM Measurement scans are performed parallel to the direction of the waveguides using the tapping mode, and the data obtained is analyzed using the Digital Instruments Nanoscope Software.

$\text{Ge}_{23}\text{Sb}_7\text{S}_{70}$ waveguide transmission loss measurements are performed on a Newport AutoAlign workstation in combination with a JDSU SWS tunable laser (see Chapter 3 for details). Optical loss in strip waveguides is measured by a cutback method using paper-

clip waveguide patterns, whereas rib waveguide loss is determined by traditional Fabry-Perot method considering the large bending loss in rib waveguides due to their small effective index contrast. Finite-Difference Time-Domain (FDTD) technique is used to simulate the waveguide facet reflectivities for accurate determination of waveguide loss via the Fabry-Perot method. Each loss number reported in this paper is averaged over more than 20 waveguides.

Figure 10 shows a cross-sectional SEM image of a strip $\text{Ge}_{23}\text{Sb}_7\text{S}_{70}$ waveguide before photoresist lift-off. Waveguides fabricated by lift-off typically show rounded corners, and the sidewall angle measured from the SEM image is $\sim 65^\circ$. Figure 10 shows the AFM scan of a $2\ \mu\text{m}$ by $2\ \mu\text{m}$ square area showing the surface morphology of a waveguide with a width of $750\ \text{nm}$. The AFM measurements also yield a sidewall line RMS roughness value of $(11 \pm 2)\ \text{nm}$ for as-fabricated waveguides, which is averaged over several AFM scans on different waveguides across an entire wafer. In comparison, plasma etched chalcogenide waveguide sidewalls exhibit RMS roughness values typically ranging from $20\text{-}150\ \text{nm}$ depending on etching parameters⁸¹. The relatively low sidewall roughness in waveguides fabricated through lift-off can be attributed to the fact that the sidewall is defined during a deposition process rather than etching. In the lift-off process, the major source of sidewall roughness probably originates only from edge roughness of photoresist patterns. Conspicuous by its absence here is evidence of any side-etching effect, often responsible for sidewall surface roughening in a standard etching process. We also find that waveguides with three different widths, $0.75\ \mu\text{m}$, $1.2\ \mu\text{m}$ and $1.6\ \mu\text{m}$, exhibit the same sidewall roughness value within the accuracy of our AFM measurement. Similarly,

the average RMS roughness on the strip waveguide top surface is determined to be (1.6 ± 0.3) nm, an understandably much lower value given that the top surface is formed during the film deposition process and is free of any roughness resulting from photolithography.

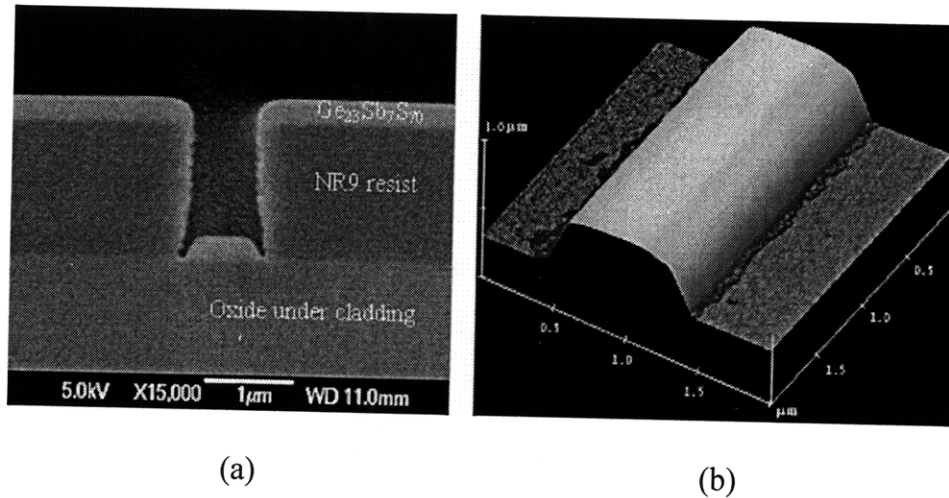


Figure 10 (a) Cross-sectional SEM image of a $\text{Ge}_{23}\text{Sb}_7\text{S}_{70}$ waveguide before photoresist lift-off, showing a sidewall angle of $\sim 65^\circ$ and rounded corners; (b) Submicron strip waveguide morphology measured by AFM with a sidewall RMS roughness value of (11 ± 2) nm and top surface RMS roughness of (1.6 ± 0.3) nm.

Measured transmission losses of strip and rib $\text{Ge}_{23}\text{Sb}_7\text{S}_{70}$ waveguides with different widths and cross-sectional geometry at the wavelength of 1550 nm are tabulated in Table 2. These data show that the Transverse-Magnetic (TM) mode exhibits lower transmission loss than the Transverse-Electric (TE) mode in strip waveguides with the same width. Also, transmission losses for both modes decrease as strip waveguides become wider. Additionally, as expected, the loss dependence on width is more significant for the TE mode than for TM mode. All these experimental observations are characteristic of loss arising from sidewall roughness scattering, often the dominant loss mechanism in high-

index-contrast waveguides, as we will analyze in detail later. The rib waveguides show very low loss for both TE and TM modes due to less mode interaction with sidewall roughness in the rib waveguide geometry.

Table 2 Measured optical transmission losses and calculated modal parameters of $\text{Ge}_{23}\text{Sb}_7\text{S}_{70}$ waveguides at 1550 nm and modal parameters for fundamental TE/TM modes calculated using a finite-difference technique.

| Waveguide width w | 0.75 μm (strip) | | 1.2 μm (strip) | | 1.6 μm (strip) | 1.2 μm (rib) |
|---|----------------------------|-----------------------|---------------------------|-----------------------|------------------------------|----------------------------|
| | TM | TE | TM | TE | TM | TE |
| Transmission loss (dB/cm) | 3.9 ± 0.4 | 6.4 ± 0.8 | 3.5 ± 0.3 | 5.2 ± 0.5 | 2.3 ± 0.4 | < 0.5 |
| Number of modes supported | 1 | 1 | 1 | 2 | 1 | 1 |
| Effective index | 1.602 | 1.721 | 1.660 | 1.848 | 1.674 | 1.987 |
| Γ_{core} | 0.966 | 0.726 | 0.767 | 0.980 | 0.783 | 0.989 |
| $\Gamma_{\text{surface}} (\text{nm}^{-1})$ | 6.00×10^{-3} | 2.83×10^{-3} | 3.07×10^{-3} | 1.40×10^{-3} | 1.69×10^{-3} | 0.81×10^{-3} |
| $\Gamma_{\text{sidewall}} (\text{nm}^{-1})$ | 4.80×10^{-3} | 1.95×10^{-3} | 1.74×10^{-3} | 0.44×10^{-3} | 0.33×10^{-3} | 7.79×10^{-5} |
| $\alpha_{\text{substrate}} (\text{dB/cm})$ | 7.2×10^{-3} | 0.098 | 2.8×10^{-5} | 0.016 | 4.0×10^{-3} | 2.8×10^{-4} |

We also experimentally verified that loss in a strip waveguide is a function of wavelength, as is shown in Figure 11. Transmission loss reduces for both TE and TM mode for longer wavelength. Per the results shown in Figure 11, one might expect lower loss at mid-IR wavelengths where the key operating wavelength of biochemical sensors would be further exploited.

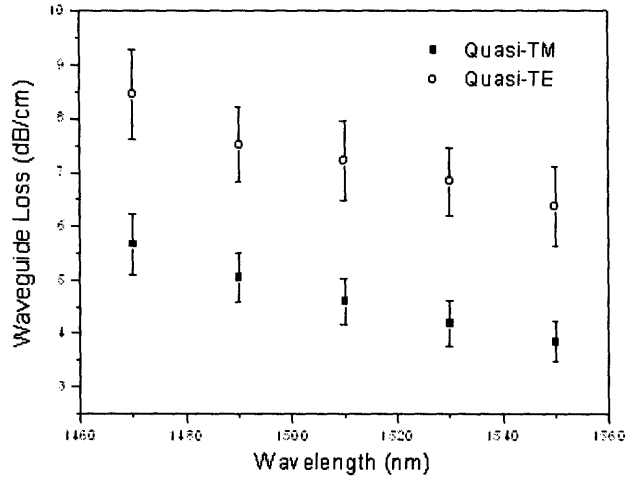


Figure 11 Measured transmission loss of single-mode $0.75 \mu\text{m} \times 0.4 \mu\text{m}$ $\text{Ge}_{23}\text{Sb}_7\text{S}_{70}$ strip waveguide as a function of wavelength. Loss increases for lower wavelength values, pointing to a negligible contribution from substrate leakage loss.

For practical applications we investigate the processing uniformity across an entire wafer. Towards this end, loss figures for $1.6 \mu\text{m}$ wide strip waveguides are measured using paper clip patterns on 40 different dies (waveguides with at least three different lengths are measured on each die to give one loss number) across a 6" wafer, and the distributions of waveguide loss values are shown in Figure 12. Statistical analysis reveals that these waveguides have an average loss of (2.3 ± 0.4) dB/cm at 1550 nm wavelength. The small standard deviation of 0.4 dB/cm indicates excellent processing uniformity of our lift-off technique, and confirms that lift-off is intrinsically a wafer-scale processing technique that lends itself to mass production.

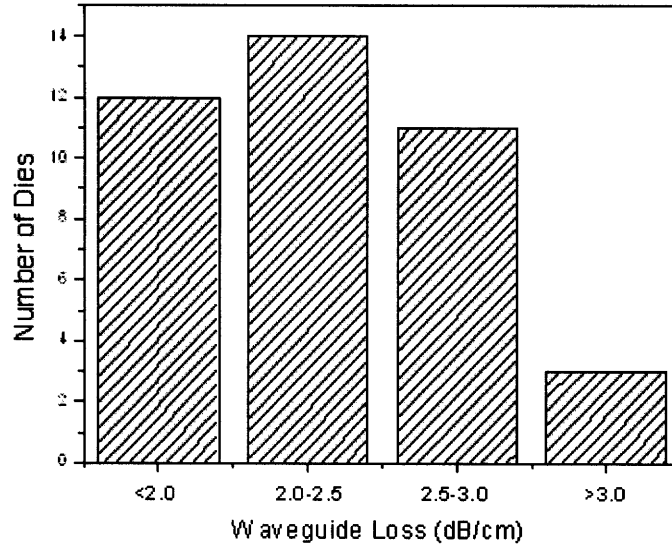
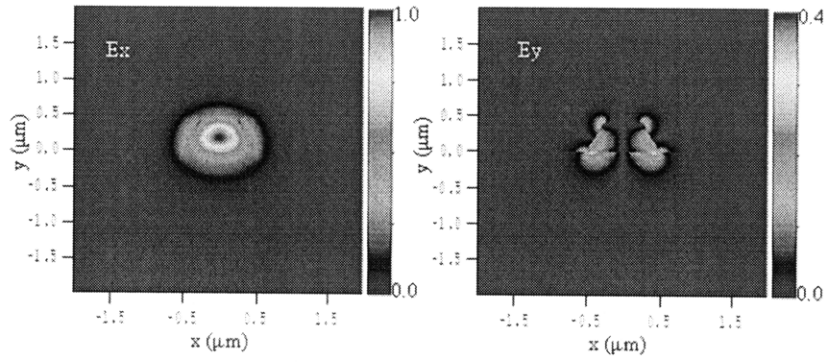
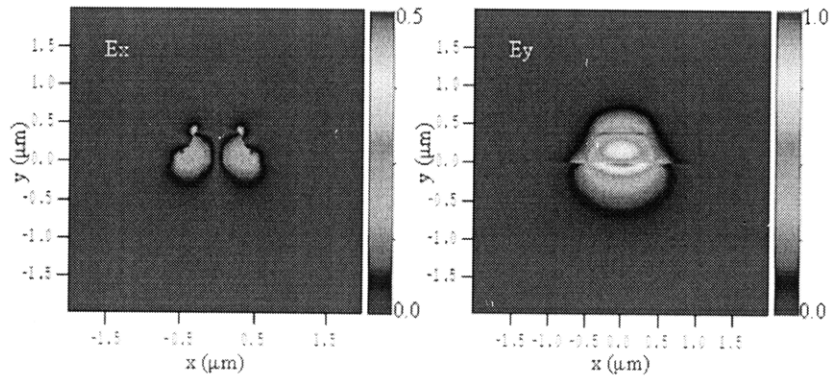


Figure 12 Statistical distributions of loss values of $1.6 \mu\text{m} \times 0.4 \mu\text{m}$ $\text{Ge}_{23}\text{Sb}_7\text{S}_{70}$ strip waveguides measured from 40 individual dies across a 6" wafer, which yield an average loss number of (2.3 ± 0.4) dB/cm. This tight distribution of waveguide loss values suggests excellent wafer-scale uniformity of the lift-off process.

Optical modes in strip $\text{Ge}_{23}\text{Sb}_7\text{S}_{70}$ waveguides are numerically simulated using a full-vectorial finite-difference method¹⁹. The simulated modes in both strip and rib waveguides are not rigorously pure TE or TM modes, and in the case of our lift-off defined waveguides, the coupling between TE and TM modes is enhanced due to the slanted sidewall profile. Figure 13 shows the simulated quasi-TE and quasi-TM modal profiles for a $0.75 \mu\text{m}$ wide strip waveguide. The presence of both x and y in-plane electric field components for both TE and TM modes clearly indicates the mixed-polarization nature of the modes. For simplicity, we still refer to these quasi-TE/TM modes as TE/TM modes below.



(a)



(b)

Figure 13 Modal profiles of (a) quasi-TE mode and (b) quasi-TM mode in a 0.75 μm wide $\text{Ge}_{23}\text{Sb}_7\text{S}_{70}$ strip waveguide with 65° sidewall angle, simulated using a finite difference technique, indicating the mixed-polarization nature of the modes.

Generally, optical loss in waveguides is the sum of contributions from: bulk material absorption, scattering from top surface roughness, scattering from sidewall roughness, surface state absorption and optical power leakage into substrate, i.e. total transmission loss can be expressed as:

$$\text{Eq. 23: } \alpha_{\text{tot}} = \sum \alpha = \alpha_{\text{bulk_absorption}} + \alpha_{\text{top_roughness}} + \alpha_{\text{sidewall_roughness}} + \alpha_{\text{surface_absorption}} + \alpha_{\text{substrate}}$$

For chalcogenide waveguide geometries shown in Figure 9, the under cladding (thermal oxide) is transparent at 1550 nm wavelength and can be regarded as loss-less. Thus the only contribution of bulk material absorption comes from the $\text{Ge}_{23}\text{Sb}_7\text{S}_{70}$ core, which is given by:

$$\text{Eq. 24: } \alpha_{\text{bulk_absorption}} = \Gamma_{\text{core}} \alpha_{\text{Ge}_{23}\text{Sb}_7\text{S}_{70}}$$

where Γ_{core} represents the modal power confinement factor in the $\text{Ge}_{23}\text{Sb}_7\text{S}_{70}$ core and $\alpha_{\text{Ge}_{23}\text{Sb}_7\text{S}_{70}}$ is the bulk material absorption in $\text{Ge}_{23}\text{Sb}_7\text{S}_{70}$ film. Similarly, we can define the power confinement factor Γ_{surface} near the waveguide surface, which is correlated to the surface absorption loss by:

$$\text{Eq. 25: } \alpha_{\text{surface_absorption}} = \Gamma_{\text{surface}} \alpha_{\text{surface}}$$

Note that here Γ_{surface} denotes the optical power confined in a thin depth on the waveguide surface and thus has the dimension of inverse length (nm^{-1}). $\alpha_{\text{sidewall_roughness}}$ and $\alpha_{\text{top_roughness}}$ characterize the optical loss due to scattering and thus is a strong function of waveguide sidewall RMS roughness values and correlation length. Contribution from scattering from top surface roughness is negligible, given the much smaller surface RMS roughness measured by AFM. Therefore, Eq. 23 can be expressed as a linear combination from the different contributions:

$$\text{Eq. 26: } \alpha_{\text{tot}} = \sum \alpha = \Gamma_{\text{core}} \alpha_{\text{Ge}_{23}\text{Sb}_7\text{S}_{70}} + \alpha_{\text{sidewall_roughness}} + \Gamma_{\text{surface}} \alpha_{\text{surface}} + \alpha_{\text{substrate}}$$

Values of Γ_{core} , Γ_{surface} and $\alpha_{\text{substrate}}$ for the waveguide geometries and modes in this study are calculated in a way similar to integrated the power flux density in the areas of interest and tabulated in Table 2. It is clear that substrate leakage ($\alpha_{\text{substrate}}$) hardly contributes to the waveguide loss due to the large index contrast between waveguide core and oxide under cladding. Low substrate leakage loss is also confirmed from Figure 11, which

shows that propagation loss in these waveguides increases rather than decreases at the shorter wavelengths. Another observation from Table 2 is that Γ_{surface} is larger for TM modes compared to TE modes, which suggests that surface absorption is not the dominant source of loss since TE modes typically exhibit higher loss despite the smaller modal overlap with the waveguide surface. Γ_{sidewall} , defined in a way similar to that of Γ_{surface} for optical field intensity near the waveguide sidewall, gives an estimate of the interaction strength between the optical mode and waveguide sidewall roughness. The very small values of Γ_{sidewall} in rib waveguides indicate that optical loss in rib waveguides is solely induced by bulk and surface absorption. Thus the optical loss arising from bulk and surface absorption in strip waveguides can be extracted from rib waveguide loss figures using Eq. 24 and Eq. 25. Since the TE mode confinement factor in the rib waveguide is close to unity, the upper limit of material loss in thermally evaporated $\text{Ge}_{23}\text{Sb}_7\text{S}_{70}$ films is thus ~ 0.5 dB/cm for these modest purity materials. Therefore, we conclude that optical loss in these high-index-contrast strip waveguides mainly arises from sidewall roughness scattering.

4.3. Comparison of lift-off and plasma etching techniques

Since plasma etching is probably the most commonly used patterning technique in microelectronics and microphotonics, it is important to draw a direct comparison between plasma etching-patterned waveguides and those fabricated by lift-off. Towards this end, waveguides from thermally evaporated $\text{Ge}_{23}\text{Sb}_7\text{S}_{70}$ films have been fabricated using both plasma etching and lift-off techniques. The two methods have been compared in their ability to provide high quality, low-loss waveguides for microphotonics applications.

In plasma etching fabrication, $\text{Ge}_{23}\text{Sb}_7\text{S}_{70}$ coated wafers are first spin-coated with commercial photoresist (OCG-825) on a Headway spinner at 2000 rpm. No photoresist adhesion promoter is used during the processing, since the adhesion of the baked resist to the glass is sufficient to survive development and subsequent glass etching without peeling. A 10 min bake at 130 °C follows. The purpose of the relatively high temperature bake (with respect to the regular soft bake temperature of 90 °C) is to decrease the photosensitivity of the photoresist and thus allows accurate control of the resist dissolution rate during development. Optical microscope inspection of the resist layer reveals no cracking after baking. Subsequent UV exposure is carried out on a Karl Suss MJB3 aligner. A commercially available developer (OCG 934 1:1) is used to develop the resist. In order to prevent wet etching by the developer and the resulting undercut and film peeling, the development is stopped before the resist layer is fully developed by controlling the development time. The remaining thin layer of undeveloped photoresist is then etched by an oxygen plasma in a dual chamber PlasmaTherm plasma etcher, followed by a reactive fluorine ion etch in the same chamber to define the waveguide patterns.

To fabricate the waveguide using plasma etching, four different gas chemistries, O_2 , Ar, CHF_3 and SF_6 , are tested. Etch rates of the recipes are monitored off-line using a Dektak IIA surface profiler and are tabulated in Table 3. The gas flow rate, pressure and incident RF power are optimized to yield vertical sidewall profiles and good pattern fidelity. Both

fluorine chemistries are effective in glass etching, while $\text{Ge}_{23}\text{Sb}_7\text{S}_{70}$ is almost inert in an oxygen plasma.

Table 3 Plasma etching conditions and etch rates of $\text{Ge}_{23}\text{Sb}_7\text{S}_{70}$ film in CHF_3 , SF_6 , Ar and O_2 gas chemistries

| Gas Chemistry | Flow Rate (sccm) | Pressure (mTorr) | Incident Power (W) | Etch Rate (nm/min) |
|----------------|---------------------|---------------------|-----------------------|-----------------------|
| CHF_3 | 40 | 30 | 350 | 60 ± 10 |
| SF_6 | 40 | 30 | 350 | 300 ± 30 |
| O_2 | 40 | 30 | 350 | ~ 3 |
| Ar | 40 | 40 | 250 | 23 ± 3 |

After extended exposure (e.g. ~ 15 min) to reactive plasma (except for O_2 , which ashes the photoresist), the photoresist denatures and becomes virtually impossible to remove after etching. Neither oxygen plasma nor sonication in organic solvents such as acetone removes the layer, which was confirmed by other similar studies⁸². Thus even though Ar ion milling has previously been used to pattern ridge waveguides in GeS_2 film⁸³, our study reveals that it is an inefficient method for etching $\text{Ge}_{23}\text{Sb}_7\text{S}_{70}$ films, which only allows fabrication of shallow ridge waveguides due to its slow etch rate. Based on this consideration, the CHF_3 and SF_6 recipes in Table 3 are employed for actual waveguide fabrication in this study. Channel waveguides with two different core widths, 3 μm and 4 μm , are patterned using both plasma etching recipes. Residual photoresist is removed by an oxygen plasma. A 20 μm thick layer of SU8 (SU8 2015, Microchem Inc.) is then spin-coated onto the wafer to serve as the waveguide upper cladding.

The lift-off procedures are slightly modified from the description in the section 4.2, to allow a side-by-side comparison with plasma etching, the major difference being that the whole photolithography process is now carried out on the same Karl Suss MJB3 aligner. Commercially available negative photoresist NR7-1000P is used for Ge₂₃Sb₇S₇₀ lift-off due to its negative-sloping sidewall profile, which facilitates the lift-off process.

Raman spectroscopy is used as a powerful tool to probe the structure of the glass network. The Raman spectra are recorded with a Kaiser Hololab 5000R Raman spectrometer with Raman microprobe attachment in backscattering geometry. This system has a typical resolution of 2-3 cm⁻¹ at room temperature. The system consists of a holographic notch filter for Rayleigh rejection, a microscope equipped with 10x, 50x and 100x objectives (the latter allowing Raman spectra to be collected from spot sized down to 5-7 μm), and a CCD detector. A 785 nm NIR semiconductor diode laser is used for excitation. The use of a 785 nm source with a low excitation power of ~5 mW is specific to our study to avoid photo-structural changes which the laser beam may induce in the samples during measurement. The spectral measurements are repeated on several different locations on the films and the resultant spectra are numerically averaged to eliminate any impact from minor film non-uniformity.

The amorphous nature, of the as-deposited and patterned films, is confirmed by X-ray diffraction. Neither crystallization peaks nor diffraction spectra changes are observed for patterned films, indicating the absence of major crystallization and structural

modification induced by processing. Wavelength Dispersive Spectroscopy (WDS) composition analysis carried out on a JEOL JXA-733 superprobe reveals that the resulting waveguides have the same composition as the as-deposited film within the accuracy of the measurement.

The measured Raman spectra of the as-deposited and patterned $\text{Ge}_{23}\text{Sb}_7\text{S}_{70}$ films, shown in Figure 14, are in good agreement with previous studies of the Ge-Sb-S glass system⁸⁴. The Raman spectra present a broad band with 2 bands of low amplitude in the 200-250 cm^{-1} . In accordance with Mei *et al*, the bands at 330 and 402 cm^{-1} have been assigned to the A_1 and T_2 modes of corner sharing $\text{GeS}_{4/2}$ groups⁸⁵. The bands at 340, 375 and 427 cm^{-1} have been attributed, respectively to A_1 mode of the GeS_4 molecular units, to the T_2 mode of 2 edge-sharing $\text{GeS}_{4/2}$ tetrahedra and to the vibration of two tetrahedra connected through a bridging sulfur $\text{S}_3\text{Ge} - \text{S} - \text{GeS}_3$. The shoulder at around 302 cm^{-1} has been assigned to the E modes of SbS_3 pyramids⁸⁶, which, however, in this case becomes indistinguishable with the contribution from the Si wafer substrate band at $\sim 305 \text{ cm}^{-1}$. The bands in the range 175-225 cm^{-1} have been attributed to A'_1 mode of a six-membered ring and also to the vibration of Ge-S-Ge dithiogermanate. The shoulder at 250 cm^{-1} in the films can be attributed the vibrations of “wrong-bonds” in the glass network, such the Ge-Ge bond in the ethane-like unit $\text{S}_3\text{Ge}-\text{GeS}_3$. As one would expect, lift-off does not lead to observable structural modifications in the waveguide, since no thermal or chemical processing steps are involved in the patterning process. In contrast, one can notice slight variations of the Raman spectrum after both plasma etching processes. Figure 15 shows an example of the deconvoluted Raman spectra, taken from as-deposited

$\text{Ge}_{23}\text{Sb}_7\text{S}_{70}$ film. One can notice that the ratio of the band at 295 cm^{-1} decreases and the band at 340 cm^{-1} increases when the waveguide is made by plasma etching suggesting a lower number of SbS_3 units and higher number of isolated GeS_4 units in the structure of the waveguide. Nevertheless, we believe that such structural variations are not a major concern for waveguide loss reduction, given the small degree of Raman spectra variation.

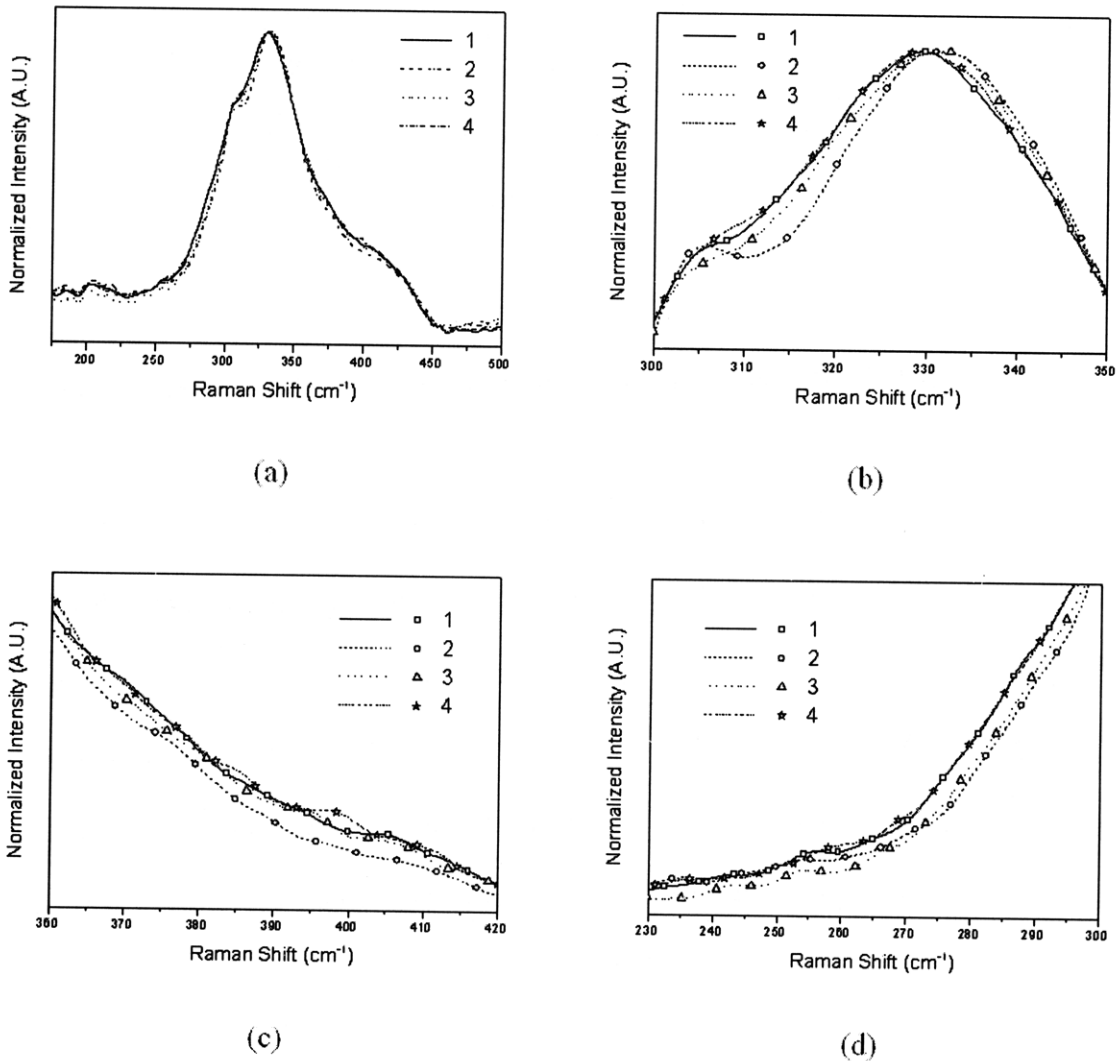
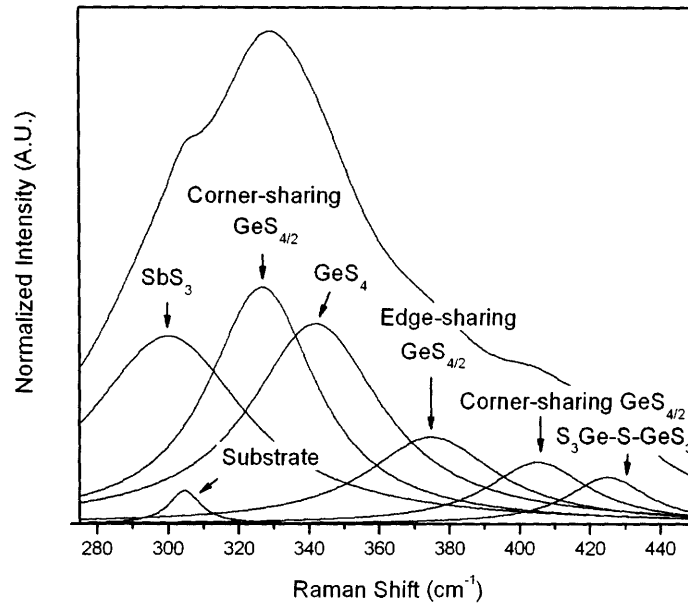


Figure 14 (a) – (d) Raman spectra of (1) as-deposited $\text{Ge}_{23}\text{Sb}_7\text{S}_{70}$ film; (2) $\text{Ge}_{23}\text{Sb}_7\text{S}_{70}$ waveguide patterned by CHF_3 plasma etching; (3) $\text{Ge}_{23}\text{Sb}_7\text{S}_{70}$ waveguide defined by SF_6 plasma etching; (4) $\text{Ge}_{23}\text{Sb}_7\text{S}_{70}$ waveguide fabricated by lift-off.



(e)

Figure 15 As-deposited $\text{Ge}_{23}\text{Sb}_7\text{S}_{70}$ film with peak deconvolution result.

The sidewall angles of the fabricated waveguides are observed using SEM and the pictures are exhibited in Figure 16. The waveguides fabricated using plasma etching have similar sidewall angles. As seen in Figure 16, the waveguides patterned by fluorine ion etching showed vertical sidewall angle which can be attributed to the formation of polymer protective coatings on feature sidewalls during plasma etching⁸⁷. In contrast, lift-off features lead to a sidewall angle of $\sim 70^\circ$, as demonstrated by rounded corners in Figure 16.

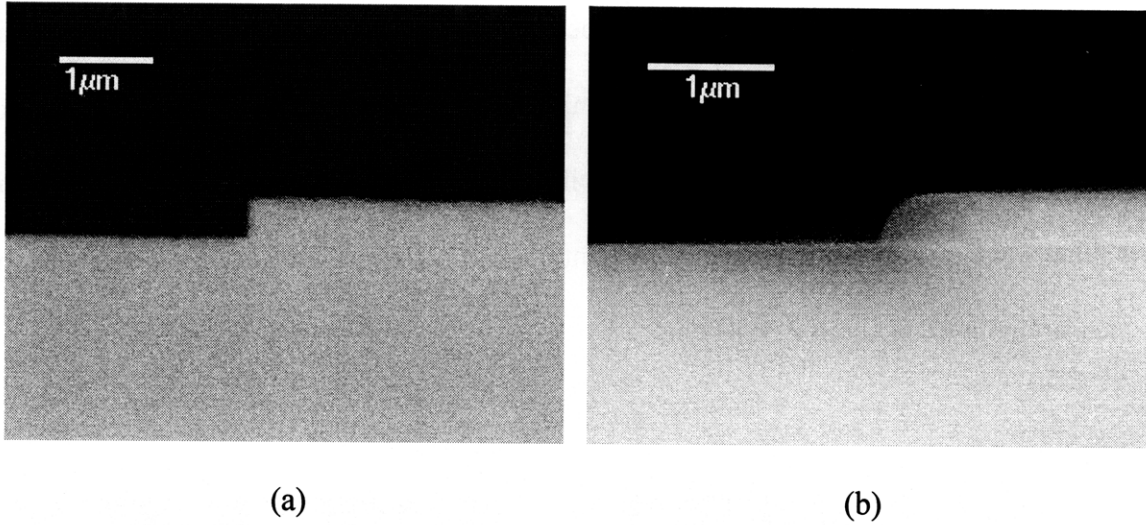


Figure 16 Cross-sectional image of $\text{Ge}_{23}\text{Sb}_7\text{S}_{70}$ channel waveguide sidewall profile patterned by (a) SF_6 plasma etching, indicating vertical sidewall; and (b) lift-off, showing a sidewall angle of $\sim 70^\circ$ and rounded corners.

Surface profiles of as-fabricated waveguides are measured by AFM and analyzed using the Digital Instruments Nanoscope Software. The RMS sidewall roughness values for $\text{Ge}_{23}\text{Sb}_7\text{S}_{70}$ waveguides patterned by CHF_3 plasma etching, SF_6 plasma etching and lift-off are 20 ± 5 nm, 17 ± 4 nm and 10 ± 2 nm, respectively.

As an example, Figure 17 shows the measured optical modal profile from a $3 \mu\text{m}$ wide channel waveguide patterned by SF_6 plasma etching, and the numerically simulated optical mode in the same waveguide obtained from a finite-difference technique⁸⁸. Similarly good agreement between simulation and experiment is observed for a $3 \mu\text{m}$ wide waveguide. The measured mode size (defined as the area where the optical field intensity is greater than $1/e$ of the peak intensity, where $e = 2.718$) is $2.5 \mu\text{m} \times 1.1 \mu\text{m}$, in contrast to the simulation result of $2.7 \mu\text{m} \times 0.9 \mu\text{m}$. The slight deviation can be

attributed to both, the finite size of the fiber tip, as well as a spatial shift of the fiber tip during mode profile measurement. Transmission losses at a wavelength of 1550 nm for waveguides with two different widths are listed in Table 4. Given the small aspect ratio of the waveguides, polarization dependent losses are expected and are confirmed by measurement to be about 2-3 dB/cm.

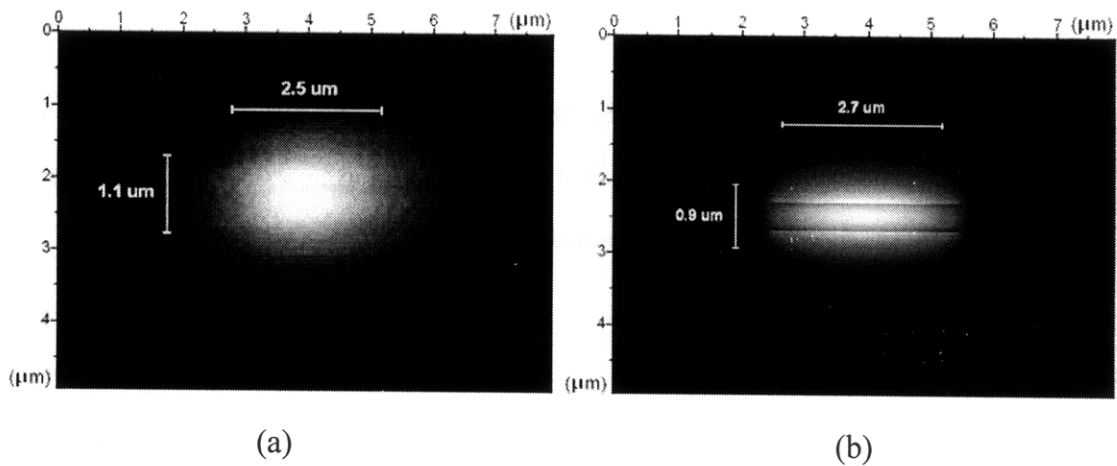


Figure 17 (a) Measured TM-like mode profile of a 3 μm wide $\text{Ge}_{23}\text{Sb}_7\text{S}_{70}$ channel waveguide defined by SF_6 plasma etching, showing single mode operation; (b) Numerically simulated optical mode in 3 μm wide waveguide using finite-domain technique, showing good agreement with the measured results.

As seen in Table 4, when the width of the waveguide increases, the optical propagation loss increases. This can be attributed to the increased coupling into lossy higher order modes in wider waveguides. In addition, channel waveguides patterned by lift-off show lower loss compared to the channel waveguides defined by plasma etching techniques and this is attributed to better waveguide quality. Material absorption accounts for < 0.5 dB/cm optical loss as is confirmed by the loss measured in $\text{Ge}_{23}\text{Sb}_7\text{S}_{70}$ shallow rib waveguides detailed in the section 4.2; the residual loss excluding materials absorption is

~ 4 dB/cm in waveguides defined by SF₆ plasma etching and ~ 3 dB/cm for lift-off patterned waveguides. The lower loss in waveguide defined by lift-off has to be related to the better waveguide quality (e.g. smaller sidewall roughness, less defects from fabrication) resulting from lift-off technique. This conclusion is also consistent with our sidewall roughness measurement results.

Table 4 Transmission loss (± 0.4 dB/cm) and sidewall roughness (± 2 nm) of Ge₂₃Sb₇S₇₀ channel waveguides patterned by different techniques (measured at 1550nm by cutback technique): CHF₃ plasma etching, SF₆ plasma etching and lift-off. The waveguides in this study have the same core height of 400 nm.

| | CHF ₃ plasma etching | SF ₆ plasma etching | Lift-off |
|---|---------------------------------|--------------------------------|---------------|
| Transmission loss of 3 μ m wide channel waveguides (± 0.4 dB/cm) | 4.1 dB/cm | 4.1 dB/cm | 3.0 dB/cm |
| Transmission loss of 4 μ m wide channel waveguides (± 0.4 dB/cm) | 4.8 dB/cm | 4.5 dB/cm | 3.6 dB/cm |
| Waveguide RMS sidewall roughness | 20 \pm 5 nm | 17 \pm 4 nm | 10 \pm 2 nm |

4.4. Optical loss reduction in high index contrast (HIC) chalcogenide glass waveguides via thermal reflow

Thermal reflow has been demonstrated to be the most effective technique for completely eliminating surface roughness and associated scattering loss in silica glass photonic devices. In this section, we present thermal reflow as an effective approach for sidewall

roughness and optical loss reduction in HIC chalcogenide waveguide devices. Analogous to a fiber drawing process, the action of surface tension leads to smoothing of roughness and thus creation of a negligible scattering loss surface. Compared to a silica glass reflow process, chalcogenide glass reflow does not require thermal processing at elevated temperatures given the lower softening temperature of chalcogenides. Such a tolerant thermal budget is compatible with CMOS backend processes and imposes minimal adverse effect on other on-chip devices, an advantage for electronic and photonic integration.

4.4.1. Kinetic theory of roughness and optical loss evolution during reflow

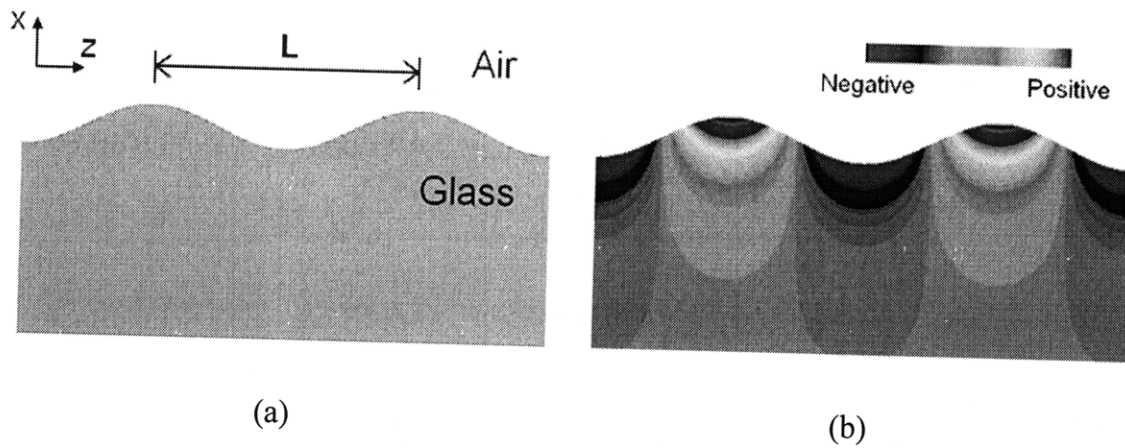


Figure 18 (a) Schematic illustration of a glass surface with sinusoidal roughness characterized by a spatial period L ; (b) calculated internal pressure due to surface tension in glass with a rough surface.

Sidewall roughness reduction during reflow is driven by surface tension of glass towards minimization of surface energy, and therefore the kinetics of this process is determined by the interaction between the surface tension force and glass viscosity. We first consider a glass surface perpendicular to the y -axis and featured by roughness described by a 1-d sinusoidal wave with a characteristic wavelength L (Figure 18a):

$$\text{Eq. 27: } H'(z) = H_L \sin\left(\frac{2\pi}{L}z\right)$$

where H is the y -coordinate of the glass surface, and H_L gives the roughness amplitude.

Since glass typically exhibits relatively high viscosity, we can assume Newtonian behavior of glass with low Reynold number. Further, gravity is much smaller compared to surface tension and thus can be neglected. In this case, the reflow process is governed by the following equations:

$$\text{Continuity equation Eq. 28: } \frac{\partial v_z}{\partial z} + \frac{\partial v_x}{\partial x} = 0$$

$$\text{Force equilibrium Eq. 29: } -\mu \frac{\partial^2 v_x}{\partial z^2} = \frac{\partial p}{\partial x} \text{ and } \mu \frac{\partial^2 v_z}{\partial x^2} = \frac{\partial p}{\partial z}$$

Here the continuity equation imposes the mass conservation constraint on viscous flow in the glass, where v_x and v_z are both functions of x and z spatial coordinates, denoting the flow velocity in the glass. Since v_x and v_z are typically very small given the short length scale under investigation, a quasi-static approximation applies and the force equilibrium conditions hold, where μ is the glass kinetic viscosity and p represents the internal pressure in the glass due to surface tension. In addition, the internal pressure on the glass surface arising from surface tension given by:

$$\text{Eq. 30: } p_{\text{surface}} = -T \frac{\partial^2 H'}{\partial z^2} = \frac{4\pi^2}{L^2} T H_L \sin\left(\frac{2\pi}{L}z\right)$$

specifies the boundary condition of this 2-d problem, where T is the surface tension (N/m) of glass at the reflow temperature.

Due to the phase matching constraint, the roughness wavelengths contributing to scattering loss lie in a range given by:

$$\text{Eq. 31: } \beta - \frac{2\pi}{\lambda_{\text{clad}}} < L < \beta + \frac{2\pi}{\lambda_{\text{clad}}}$$

where β is the propagation constant in the waveguide, and λ_{clad} is the wavelength in the cladding. For HIC waveguides, typically this represents spatial periods between 100 nm to a few microns at telecommunication wavelengths. Meanwhile, waveguide sidewall RMS roughness usually ranges from a few to a few tenths of nanometers. Consequently, with the valid approximation $H_0 \ll L$, the equations have a closed form solution:

$$\text{Eq. 32: } v_z = \frac{2\pi}{L} \frac{TH_L}{\mu} \times \exp\left(-\frac{2\pi}{L}x\right) \times \cos\left(\frac{2\pi}{L}z\right)$$

$$\text{Eq. 33: } v_x = -\frac{2\pi}{L} \frac{TH_L}{\mu} \times \exp\left(-\frac{2\pi}{L}x\right) \times \sin\left(\frac{2\pi}{L}z\right)$$

$$\text{Eq. 34: } p = \frac{4\pi^2}{L^2} TH_L \times \exp\left(-\frac{2\pi}{L}x\right) \times \sin\left(\frac{2\pi}{L}z\right)$$

A color contour map in Figure 18b illustrates the internal pressure p distribution in the glass according to the above equations. Decay rate of roughness amplitude H_L is thus given by v_x at the glass surface, which yields an exponential decay with a time constant:

$$\text{Eq. 35: } t = \frac{L\mu}{2\pi T}$$

This time constant provides an estimation on the reflow time duration necessary for significant roughness reduction to take place. For example, assuming the reflow process is performed within the fiber drawing viscosity window (10^3 to 10^6 Pa·s⁸⁹), the time it takes for a 10-fold decrease of roughness with a characteristic wavelength of 1 μm is approximately 10^{-3} to 0.1 s. Such a time scale is much shorter compared to the dwelling

time of glass preform in a fiber drawing furnace. We note that state-of-the-art chalcogenide glass fibers can achieve the very low optical loss (\sim dB/m) near 1550 nm wavelength⁹⁰, which indicates that precipitation of crystallites leading to optical scattering loss can be suppressed in the fiber drawing thermal process. Thus this analogy suggests that it is possible to achieve low loss chalcogenide waveguides via thermal reflow without compromising the glass material quality, given the short reflow time required and hence low crystallization tendency.

In general, since the boundary condition Eq. 30 is linear, the analytical solution for a surface with a random roughness distribution can be obtained through simple harmonic analysis. An arbitrary 1-d roughness distribution along the z-axis between $[-z_0, z_0]$ can be described using a function $H(z)$. The time evolution of $H(z, t)$ can then be characterized by the amplitude decay of its Fourier components:

$$\text{Eq. 36: } h_k(t = 0) = \frac{1}{2z_0} \int_{-z_0}^{z_0} H(z, t = 0) \cdot \exp(-i \frac{\pi k}{z_0} z) dz$$

$$\text{Eq. 37: } H(z, t) = \sum_{k=-\infty}^{+\infty} h_k(t = 0) \cdot \exp(-i \frac{\pi k}{z_0} z - \frac{\pi T k}{z_0 \mu} t)$$

In an ideal viscous glass melt free of crystallization, this evolution trend continues until an ultimate roughness limit is reached. This ultimate roughness limit that can possibly be achieved via thermal reflow is set forth by the equi-partition of energy in surface capillary wave modes at glass transition⁹¹.

The kinetic theory also establishes the quantitative relation between roughness evolution during reflow and optical waveguide loss reduction. For any given sidewall roughness

distribution described by a roughness autocorrelation function $R(z')$, the kinetic analysis above provides a method to quantitatively predict the time evolution of $R(z')$ during reflow. As an example, we assume the starting roughness on the top surface of a slab waveguide can be described by an exponential model⁹², which yields a roughness autocorrelation function in the form:

$$\text{Eq. 38: } R(z') = \sigma^2 \cdot \exp\left(-\frac{|z'|}{L_c}\right)$$

where L_c denotes the correlation length and σ^2 is the roughness variance. Figure 19a compares autocorrelation functions before and after reflow treatment, as is predicted by the kinetic reflow model (see Appendix III for details). Notably $R(z')$ is significantly modified after reflow. If we still use an exponential model as an approximation, the reflow treatment results in reduction of roughness variance and increased correlation length, factors that need to be taken into account when making waveguide loss predictions. According to the Payne-Lacey model⁹³, the scattering loss in a slab waveguide with a rough surface can be calculated from the autocorrelation function:

$$\text{Eq. 39: } \alpha_s = \phi^2\left(\frac{d}{2}\right) \cdot (n_1^2 - n_2^2) \cdot \frac{k_0^3}{8\pi \cdot n_1} \cdot \int_0^\pi \overline{R}(\beta - n_2 k_0 \cos \theta) d\theta$$

where n_1 and n_2 are the core and cladding refractive indices, respectively, k_0 is the free space wave vector, d represents the waveguide thickness, β denotes the waveguide modal propagation constant, $\phi(d/2)$ is the modal field amplitude at the waveguide surface and is normalized so that:

$$\text{Eq. 40: } \int_{-\infty}^{\infty} \phi(x) dx = 1$$

and \bar{R} is the roughness spectral density, which is given by the Fourier transform of the autocorrelation function:

$$\text{Eq. 41: } \bar{R}(\xi) = \int_{-\infty}^{\infty} R(z') \cdot \exp(i\xi \cdot z') dz'$$

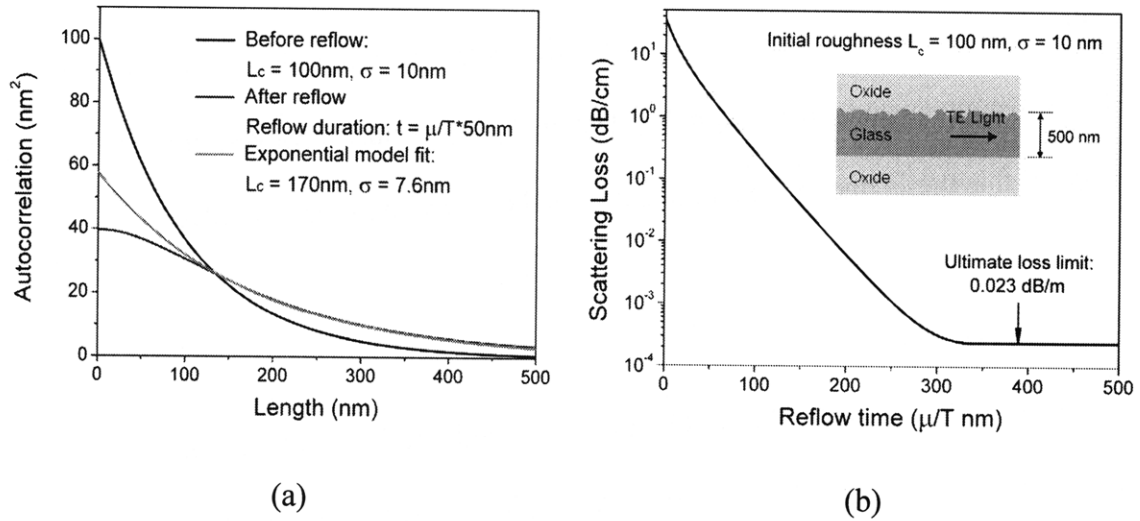


Figure 19 (a) Autocorrelation functions of waveguide sidewall roughness before and after reflow treatment predicted by the kinetic analysis: the black curve is the initial roughness in as-patterned waveguide (assume a correlation length $L_c = 100$ nm and roughness variance $\sigma = 10$ nm), the red curve corresponds to roughness after reflow treatment for a duration $t_0 = \mu/T \cdot 50$ nm, and the green curve is the numerical fit of the roughness autocorrelation after reflow using an exponential model; (b) scattering loss evolution as a function of reflow time (given in $\mu/T \cdot \text{nm}$) for TE polarization light in a 500 nm thick As_2S_3 slab waveguide (index contrast $\Delta n = 0.92$) with a rough top surface, calculated using the Payne-Lacey model and the autocorrelation functions predicted by the reflow kinetic theory. The ultimate loss is limited by equi-partition of energy in surface capillary wave modes. The inset gives the assumed initial roughness parameters and the slab waveguide configuration.

Figure 19b plots the calculated TE polarization scattering loss in an As_2S_3 slab waveguide embedded in oxide claddings as a function of reflow time. The faster decay in the initial stage is a consequence of rapidly vanishing roughness components with short

spatial wavelengths. The ultimate low loss bounded by frozen-in surface capillary wave is represented by the horizontal line at long time limit.

More rigorous scattering loss models⁹⁴ may be employed to quantitatively evaluate loss reduction after thermal reflow in waveguides with more complex geometries, such as strip waveguides and rib waveguides. Detailed discussions, however, are not within the scope of this thesis due to the complicated mathematical treatment involved.

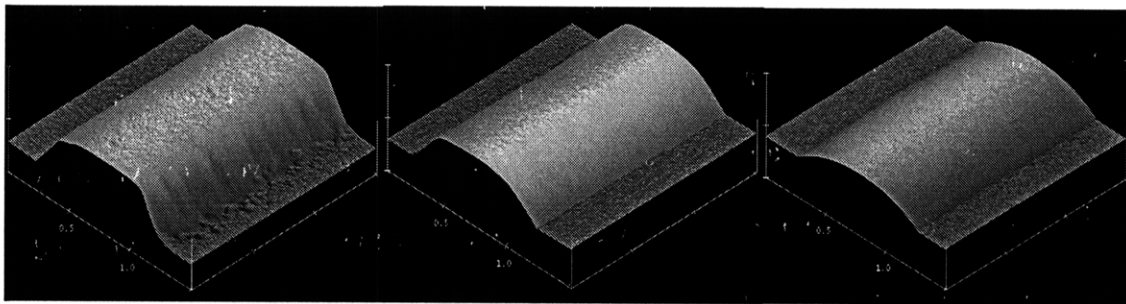
4.4.2. Experiment

Strip waveguides with a width of 800 nm and a height of 400 nm in thermally evaporated As₂S₃ films ($n = 2.37$ at 1550 nm) are patterned via lift-off on 3 μm thermal oxide coated Si wafers. The bulk glass preparation and film deposition process are described in detail in section 4.1 and 4.2. Thermal reflow of the as-patterned waveguide devices has been carried out at different temperatures (± 5 °C) on a pre-heated hotplate in a nitrogen filled glove box (oxygen and water vapor impurity < 1 ppm). Given the relatively low viscosity of As₂S₃ glass at the reflow temperatures, we choose to vary the reflow temperature and fix the reflow time to 15 s. After heat treatment, the samples are immediately transferred onto an aluminum heat sink held at room temperature to minimize dwelling time at intermediate temperatures. The time to reach thermal equilibrium in the rapid annealing and quenching process is estimated to be < 3 s via a simple multi-layer heat transfer simulation.

Before characterizing optical properties, the as-patterned and reflowed devices were spin coated with a 3 μm thick layer of SU8 polymer to prevent surface oxidation. Cavity quality factors (Q-factors) of racetrack micro-resonators with a bending radius of 50 μm comprising of strip As_2S_3 waveguides are measured using a fiber end-fire technique. The corresponding optical loss in the waveguides is calculated via:

$$\text{Eq. 42: } Q_{cr} = \frac{\lambda_0}{(\Delta\lambda)_{3dB}} = \frac{\pi n_g}{\alpha\lambda_0}$$

Here Q_{cr} denotes the cavity Q-factor at critical coupling, λ_0 denotes the resonant wavelength, n_{eff} stands for the waveguide effective index, and α represents the linear waveguide optical loss coefficient in cm^{-1} . Eq. 42 can be derived from Eq. 88. in Appendix I considering the critical coupling condition $Q_{\text{in}} = Q_{\text{ex}}$. Since our measurement gives a low material absorption of < 2 dB/cm in SU8 polymer, we can state that contributions to the waveguide loss figures measured from Eq. 42 come from surface roughness scattering and radiative loss due to waveguide bending and substrate leakage.



(a)

(b)

(c)

Figure 20 Surface morphology of As_2S_3 chalcogenide waveguides measured by AFM: (a) as-patterned; (b) reflowed at 230 $^{\circ}\text{C}$ for 15 s exhibiting reduced sidewall roughness; and (c) reflowed at 245 $^{\circ}\text{C}$ for 15 s showing significant cross-sectional geometry modification.

Figure 20 shows the surface morphology of chalcogenide glass waveguides before and after reflow at two different temperatures (> 50 °C above glass transition) for 15 s. It is clear that the sidewall roughness is significantly reduced after reflow, and at the same time the waveguide cross-sectional geometry is also modified towards a dome shape due to surface tension. The origin of such sidewall roughness in the chalcogenide waveguides is attributed to the edge roughness of photoresist mask prior to lift-off. Further optimization of the lift-off process including fine-tuning the exposure dose and applying an anti-reflection coating during lithography will help reduce the roughness. Sidewall roughness amplitude as functions of different spatial periods is plotted in Fig. 4b. Roughness with smaller spatial wavelength exhibits more significant amplitude reduction, which agrees with the kinetic theory analysis. Quantitatively, the olive curve in Figure 21 gives the roughness amplitude after 15 s reflow at 220 °C predicted by the reflow kinetic theory based on as-patterned roughness values. The deviation from theoretical predictions at short spatial wavelengths suggests the presence of limiting mechanisms to roughness reduction. Such an observation could be attributed to the local surface oxidation of As_2S_3 glass and the possible formation of As_2O_x nanocrystals, since patterned As_2S_3 films are highly susceptible to surface oxidation. Our XPS study has confirmed the presence of surface As_2O_x oxides on as-patterned As_2S_3 waveguides exposed in ambient air for just a few hours.

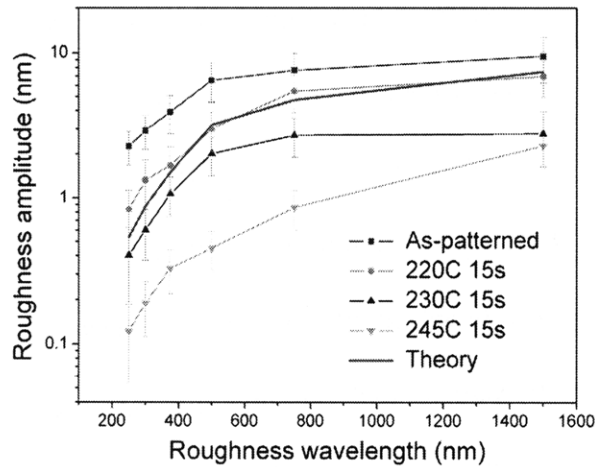


Figure 21 Waveguide roughness amplitude as a function of roughness wavelength for different reflow temperatures: the olive curve is the roughness amplitude after 15 s reflow at 220 °C predicted by the reflow kinetic theory based on as-patterned roughness values.

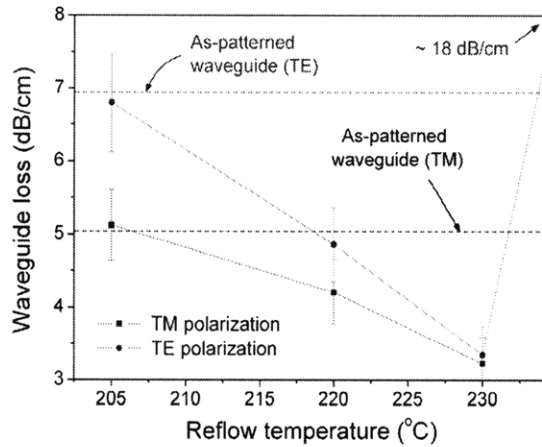


Figure 22 Measured As_2S_3 waveguide loss ($\pm 10\%$) after 15 s reflow treatment at different temperatures. The optical loss values in as-patterned As_2S_3 waveguides are represented by the two horizontal lines.

Figure 22 plots the transmission loss in As_2S_3 waveguides after reflow treatment at different temperatures. The optical loss decrease after 15 s reflow at 220 °C and 230 °C is consistent with the trend of sidewall roughness smoothing. In addition, waveguide loss

due to As_2S_3 material absorption is estimated to be < 0.6 dB/cm based on our loss measurement results in As_2S_3 microdisk resonators (Chapter 5). Therefore the observed loss decrease can be attributed to scattering loss reduction due to reflow. However, despite the continuing trend of roughness reduction at increased reflow temperature, optical loss in As_2S_3 waveguides sharply increases to $\sim (18 \pm 5)$ dB/cm after 15 s reflow at 245 °C. Here we investigate two possible mechanisms for the loss increase: 1) formation of crystal precipitates from As_2S_3 glass and the ensuing optical scattering; and/or 2) radiative loss increase due to waveguide cross-section modification. In investigating the first hypothesis of nanocrystallite scattering being the major loss-contributor: previous work has shown that annealing As_2S_3 films leads to partial crystallization of the glass, a process that is accelerated at elevated temperatures⁹⁵. Since no distinctive sharp crystalline peak is resolved in X-ray diffraction (XRD) analysis of blanket As_2S_3 films reflowed at 245 °C, we exclude the presence of large-size, ordered crystalline precipitates throughout the bulk structure of the waveguide. As a simple estimation, if we assume the scattering centers are uniformly distributed in As_2S_3 glass, the resulting waveguide loss due to Rayleigh scattering is given by:

$$\text{Eq. 43: } \alpha_R = 24\pi^3 N_p V^2 \left(\frac{n^2 - n_0^2}{n^2 + 2n_0^2} \right)^2 \cdot \left(\frac{n_0}{\lambda} \right)^4 \cdot \Gamma$$

where N_p is the volume density of scattering centers, V is the volume of crystallites, λ gives the free-space wavelength, Γ is the waveguide confinement factor, and $n = 2.74$ and $n_0 = 2.37$ represent the refractive indices of crystallites (taken as the ensemble averaged index of randomly oriented As_2S_3 orpiment crystalline particles) and As_2S_3 glass matrix at 1550 nm, respectively. Eq. 43 is originally derived for scattering events in free space, and thus actually overestimates the scattering loss in a waveguide since the presence of

optical confinement modifies the dipole radiation pattern and reduces radiation efficiency. Assuming an average crystallite size of 10 nm, Eq. 43 gives a scattering center volume fraction exceeding unity, a physically impractical result. Therefore, the high loss of waveguides reflowed at 245 °C cannot be solely explained by scattering due to nano-crystallization.

Table 5: Simulated optical radiative loss at 1550 nm in as-patterned and reflowed As₂S₃ waveguides

| Type of loss | Polarization | As-patterned waveguide | Waveguide reflowed at 230 °C for 15 s | Waveguide reflowed at 245 °C for 15 s |
|--------------------------------|--------------|------------------------|---------------------------------------|---------------------------------------|
| Bending loss (dB/cm) | TE | 8.6×10^{-10} | 2.9×10^{-9} | 4.9 |
| | TM | 7.6×10^{-5} | 5.9×10^{-2} | Cut off |
| Substrate leakage loss (dB/cm) | TE | 1.7×10^{-10} | 2.6×10^{-9} | 3.6×10^{-3} |
| | TM | 1.6×10^{-7} | 9.0×10^{-3} | Cut off |
| Modal mismatch loss (dB/cm) | TE | 4.0×10^{-3} | 4.6×10^{-3} | 8.6 |
| | TM | 1.1×10^{-2} | 2.7×10^{-2} | Cut off |

Alternatively, while investigating the second hypothesis of radiative loss being the major loss-contributor, we notice that the waveguide height decreases from 400 nm to ~ 200 nm after a reflow treatment at 245 °C, which may be attributed to the partial evaporation of As₂S₃ glass. Such film thickness decrease due to partial evaporation also visually manifests as apparent color change in blanket As₂S₃ glass films reflowed at 245 °C. We perform waveguide modal simulations to quantitatively evaluate the optical radiative loss increase due to such waveguide cross-section modification. Experimentally measured waveguide cross-sectional geometry is used as the input for finite difference (FD) modal

simulations. The resulting waveguide bending loss and substrate leakage loss are calculated by full-vectorial bending mode solver incorporating cylindrical perfectly matching boundary layers (CPML) in the FD simulations⁹⁶. Modal mismatch loss between the straight and curved sections in a racetrack resonator is simulated using a mode-matching technique. The simulated loss values are tabulated in Table 5. Notably, the waveguide reflowed at 245 °C becomes highly susceptible to the three radiative loss mechanisms, whose simulated loss figures also exhibit strong dependence on the actual thickness value.

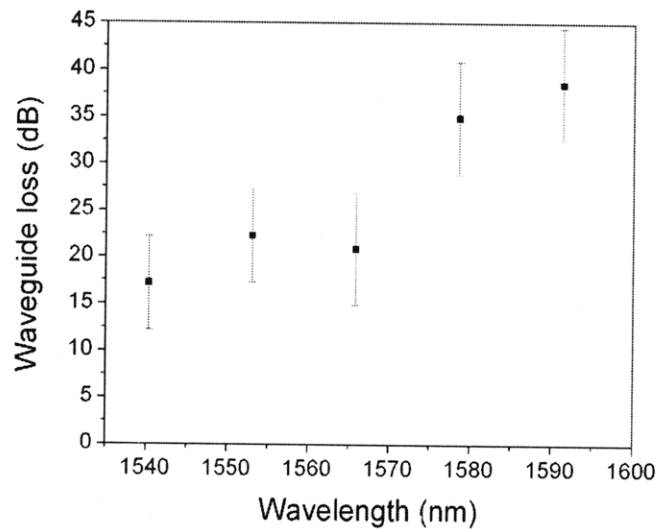


Figure 23 Measured As_2S_3 waveguide loss after 15 s reflow at 245 °C: the increased optical loss at longer wavelength is characteristic of radiative loss mechanisms but is not expected by the crystalline precipitation scattering hypothesis.

In addition, we observe monotonically increasing optical loss at longer wavelengths in waveguides reflowed at 245 °C as is shown in Figure 23, a phenomenon which is expected if radiative loss is the major loss contributor but inconsistent with the crystal

precipitate scattering hypothesis. For practical applications, the radiative loss, proven here as the primary source of loss in our lift-off patterned waveguides, may be further reduced by appropriate waveguide engineering, leading to a larger optical loss reduction via thermal reflow.

4.5. Optofluidic integration

We have tested two types of microfluidic-microphtononic integration schemes in our work. In the first process, a hybrid SU8-PDMS (polydimethylsiloxane) channel is used. In the second approach, a replica-molded PDMS channels is directly bonded over the photonic component.

In the SU8-PDMS hybrid approach, microfluidic channels as well as fluid reservoirs were defined in a 25 μm -thick layer of SU8 (SU8 2025, Microchem Inc.) photocurable resin that was spun coated onto the wafer, in a second photolithography step after the photonic components have been fabricated. The SU8 channels were then sealed using a PDMS cover. Before bonding, the wafer was cleaved into 12 mm \times 8 mm dies. Due to differences in chemical composition, PDMS cannot be irreversibly bonded onto SU8 even after oxygen plasma surface treatment. To improve the adhesion between PDMS and SU8, a two-stage curing procedure was employed. PDMS monomer (Sylgard 184 Silicone Elastomer Kit, Dow Corning Inc.) was mixed with its curing agent at a 15:1 ratio. The mixture was degassed in a dessiccator and then partially cured at 65°C for 1 h. Partially cured PDMS exhibits improved adhesion to SU8 due to uncross-linked dangling bonds on partially cured PDMS surface. Fluid inlet and outlet holes were punched into

the PDMS cover using a syringe prior to its bonding to SU8 channels. Finally, the assembled device was heated at 65°C for 3 h to fully cross-link the monomer to form the polymer. Plastic tubing systems were added to the liquid inlet and outlet to allow pressure injection of fluids.

In the other process, PDMS microfluidic channels with a width of 100 μm and a height of 30 μm are fabricated via replica molding. In the replica molding process, a SU8 pattern on silicon wafer fabricated by standard lithography is used as the mold. The surface of the mold is pre-treated using a silanizing agent to facilitate mold releasing. Then PDMS monomer is poured over the mold and allowed to cure at 65°C for 3 h, which completes the channel fabrication after cutting the PDMS channels from the mold. After oxygen plasma treatment, the channels are irreversibly bonded onto the chips on which the microdisks are patterned. Liquid inlet and outlet access holes are punched prior to bonding, and PTFE (polytetrafluoroethene) tubing is attached into the access holes to complete the microfluidic chip fabrication. Compared to the first approach, this direct bonding process provides improved mechanical robustness and better adhesion between the channels and the substrate.

4.6. Summary

In this Chapter, we describe the lift-off process we have developed. The advantage of this lift-off technique compared to conventional plasma etching is three-fold: 1) compatibility with Si-CMOS backend process; 2) reduced sidewall roughness due to elimination of lateral etching effect; and 3) non-composition specific ideal for rapid prototyping.

Although it has been shown that waveguides patterned using lift-off exhibit reduced sidewall roughness, scattering loss associated with roughness scattering is still a major loss contributor in high-index-contrast (HIC) chalcogenide glass waveguides. To overcome scattering loss, we devise two loss reduction strategies by incorporating graded-index cladding layers and by performing a thermal reflow treatment. Both approaches are experimentally demonstrated to effectively reduce scattering loss arising from waveguide sidewall roughness.

Building on the chalcogenide waveguide processing technology, microfluidic-microphtonic integration is achieved by integration of microfluidic channels with chalcogenide glass photonic devices. The resulting optofluidic device is the platform for biochemical sensing we will discuss in Chapter 7 and Chapter 8.

Chapter 5. Chalcogenide glass optical resonators

Although chalcogenide glasses possess superior optical properties ideal for a range of applications that involve photon-matter interactions and optical micro-resonators such as micro-ring and micro-disks are uniquely suited for such applications, micro-ring or micro-disk resonators had not previously been fabricated in chalcogenide glass until our first demonstration of As_2S_3 racetrack resonators. This is largely due to the lack of fine-line patterning techniques applicable to chalcogenide glasses, since these glasses are not traditionally considered CMOS-compatible and no access to the fine-line lithography tools in CMOS fabrication lines would be granted. Further, in high-index-contrast material systems including chalcogenide glasses, the gap between the resonator and its bus waveguide typically has to be smaller than a few hundred nanometers to guarantee sufficient coupling, a requirement very difficult to fulfill using conventional aligner lithography techniques. Therefore the lift-off technique detailed in Chapter 4 bears significance in this regard and we have employed this technique for the fabrication of chalcogenide glass resonators, as we will describe in this chapter.

5.1. Racetrack resonators

Racetrack resonators are named after their resemblance to a stadium racetrack in shape. The straight portion of its circumference provides improved coupling to the bus waveguide and hence allows a relatively tolerant fabrication process. However, the abrupt curvature change at the junction between the straight and curved sections in a racetrack resonator can induce additional loss due to modal mismatch (especially in the

case of a small-radius racetrack resonator), and possibly leads resonator cavity Q-factor deterioration. Nevertheless, we selected the racetrack design for our first chalcogenide glass resonator demonstration given its fabrication tolerance.

The bulk preparation and film deposition process are described in Chapter 4. These devices were patterned by lift-off, and the whole patterning process has been carried out on a 500 nm CMOS line, following the lift-off procedures detailed in Chapter 4. The CMOS-compatibility allows this process to be scaled up for mass production. The racetracks are comprised of strip waveguides with a width of 800 nm and a height of 450 nm. After patterning, a layer of 3 μm thick SU8 polymer was spin-coated to serve as the top cladding. The device was subsequently annealed at 130°C for 3 hours to stabilize the glass structure. Figure 24 shows the top view of a fabricated resonator. The fabricated device has a small footprint of 0.012 mm^2 , and the total cavity length is $\sim 409 \mu\text{m}$.

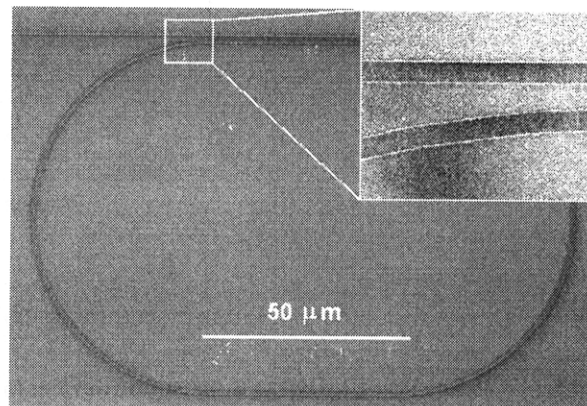


Figure 24 Optical micrograph of a fabricated resonator device; inset SEM micrograph shows the coupling region between the coupling (bus) waveguide and the racetrack.

Figure 25 shows a measured transmission spectrum of TM polarization. The resonator has a Free Spectral Range (FSR) of 2.5 nm and a maximum extinction ratio of 32 dB near 1550 nm. Such a high extinction ratio indicates that the resonator works near the critical coupling regime. Cavity Q, defined as the ratio of wavelength against 3 dB resonant peak width, was determined to be $\sim 10,000$ in this first demonstration. This Q value corresponds to an equivalent waveguide loss of 16.5 dB/cm. This relatively high loss value, however, is not intrinsic to the glass material or resonator design, but due to a data digitization error in the photomask fabrication process. In a second iteration, we digitize the bend section in a racetrack with a large number of segments (> 256), and obtain a Q-factor of $\sim 30,000$ in the new batch of devices.

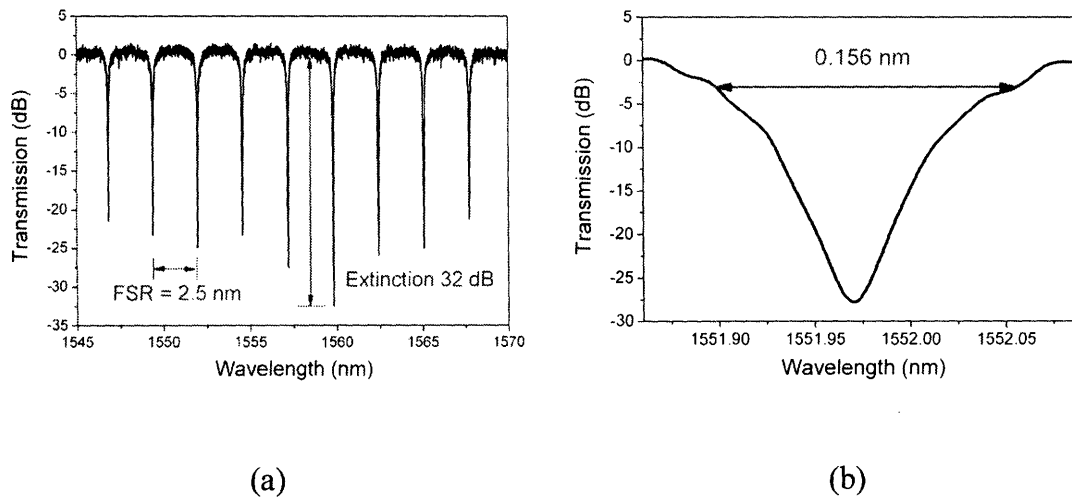


Figure 25 Transmission spectra of TM polarization in a resonator device: (a) the resonator exhibits an FSR of 2.5 nm and an extinction ratio of 32 dB; (b) the resultant spectrum averaged over 64 consecutive scans.

5.2. Micro-disk and micro-ring resonators

5.2.1. Modal properties

It is interesting to compare the modal properties of micro-ring and micro-disk resonators, since they are probably the two types of planar travelling wave resonator geometries most commonly adopted. Understanding the difference between their modal characteristics is also critical to analyzing their different optical properties, such as impact of sidewall roughness scattering in both cases. Here we perform simulations using a complex film mode matching (FMM) technique⁹⁷ to solve for resonator mode in As_2S_3 ($n = 2.37$) micro-rings and micro-disks on oxide ($n = 1.45$) with an SU8 over cladding ($n = 1.57$), near the wavelength of 1550 nm. Both resonators have a height of 450 nm and a radius of 20 μm . The waveguides comprised of the micro-ring have a width of 800 nm, and we assume a vertical sidewall profile without losing generality.

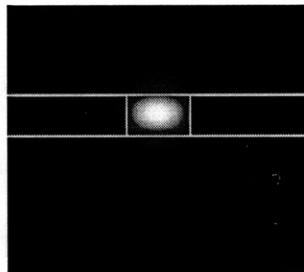


Figure 26 Simulated TM mode profile in an As_2S_3 micro-ring resonator; the rectangle in the center corresponds to the As_2S_3 core.

Figure 26 shows the simulated TM mode profile in an As_2S_3 micro-ring resonator. Optical modes in a micro-ring resonator closely resemble those in a straight waveguide with the same cross-sectional geometry, especially when the bending radius is large and the mode distortion due to bending is negligible. When the bending radius is small,

significant radiative loss is introduced and the mode profile is also distorted towards the centrifugal direction.

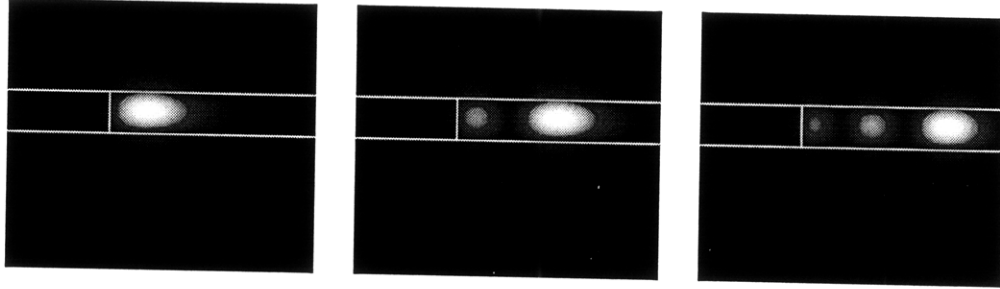


Figure 27 Simulated mode profiles for the first three TM modes in an As_2S_3 micro-disk resonator; the rectangle in the middle right-hand side of the figures represents the As_2S_3 core.

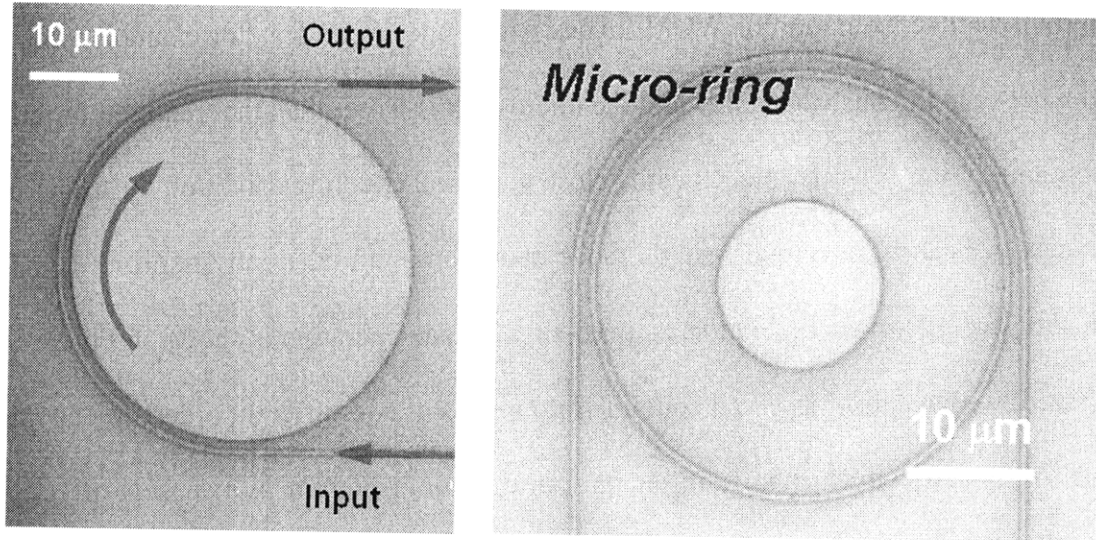
In comparison, Figure 27 shows the mode profiles for the first three TM whispery gallery modes (WGMs) in an As_2S_3 micro-disk resonator. From an approximate ray optics perspective, these different WGMs correspond to light travelling at different angles with respect to the tangent of the micro-disk. Importantly, the modal overlap with sidewalls in a micro-disk is much smaller compared to that in the case of a micro-ring: this is not only due to that there is only one sidewall present in a micro-disk, but also due to different optical modal field distributions. If we define a Γ_{sidewall} parameter in a way similar to that used in Table 2, it is found that the Γ_{sidewall} parameter for TM polarization is four-fold smaller in a micro-disk than in a micro-ring. This fact partially accounts for the higher cavity Q-factor measured in micro-disks compared to micro-rings (Table 6).

Another feature we can see from Figure 27 is that the higher order modes in a micro-disk show improved confinement in the As_2S_3 core and consequently less overlap with the mode of a bus waveguide. This observation has been leveraged in our experiments to

allow selective excitation of WGM modes with a specific order. For example, when the gap between the bus waveguide and the micro-disk is larger than that required for critical coupling of the 2nd order modes while close to critical coupling condition for the 1st order modes, we can achieve quasi-single mode operation in an inherently multi-mode micro-disk resonator. An example of such quasi-single mode operation is shown in Figure 30(a). Indeed, we have also observed coupling into modes of two different orders in one micro-disk resonator, which manifests on its transmission spectrum as two sets of resonant peaks with two distinctive FSR values. Another application we envision is that by comparing the cavity Q-factor between different orders of modes, contributions from different sources of optical loss (e.g. sidewall roughness scattering and material attenuation) can be separately identified, a technique that may be critically important for optimizing micro-disk resonator fabrication process.

5.2.2. Pulley-type coupler

As we mentioned in the previous section, a racetrack ring design partially resolves the resonator fabrication issue due to the increased coupling length; however, it also increases cavity mode volume and induces additional loss due to abrupt changes of waveguide bending curvature. Therefore, we propose a new pulley coupler design, which improves coupling efficiency and relieves the stringent fabrication tolerances, potentially allowing the fabrication of HIC glass resonators using simple, low-cost standard UV aligner lithography.



(a)

(b)

Figure 28 Optical micrographs of 20- μm -radius pulley-type As_2S_3 (a) micro-disk and (b) micro-ring resonators: the gap separating the bus waveguide and the disk is ~ 800 nm wide.

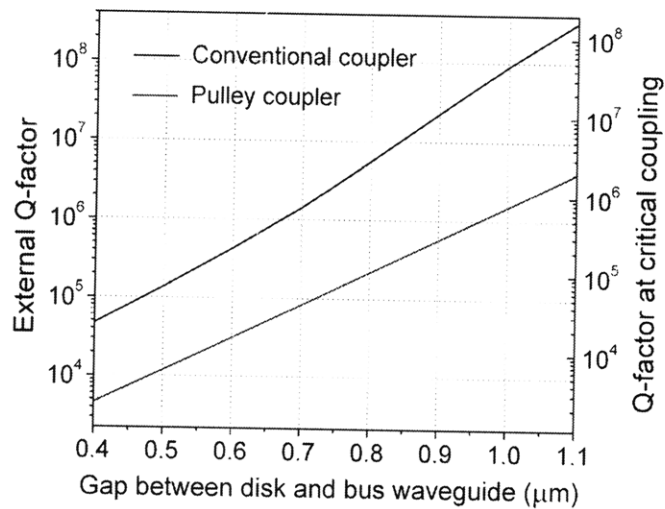


Figure 29 Simulated TE mode external Q-factor and corresponding coupled Q-factor at critical coupling at a wavelength of 1550 nm as a function of gap width between the microdisk and a bus waveguide. In this simulation, the $\text{Ge}_{17}\text{Sb}_{12}\text{S}_{71}$ (refractive index 2.06) microdisk sits on an oxide (refractive index 1.45) under cladding and is immersed in water (refractive index 1.33). The disk has a radius of 20 μm , and both the bus waveguide and the disk have a height of 450 nm.

Figure 28 shows the top views of fabricated As_2S_3 micro-disk and micro-ring resonators with a bus waveguide in a “pulley-type” coupling configuration. Compared to a conventional microdisk/micro-ring coupler, the pulley coupler design increases the coupling length leading to stronger coupling. As an example, Figure 29 shows the simulated TE polarization external Q-factor (i.e. Q-factor due to coupling) and the corresponding coupled Q-factor at critical coupling (twice the external Q due to coupling alone) when the gap width is varied. The optical bending modes of the disk and the waveguide are calculated using a full-vectorial bending mode solver⁹⁶. The computed fields are then substituted into the coupled-mode equation to calculate the coupling coefficients⁹⁸, and Q-factors are extracted based on the coupling coefficients using Little’s formulation⁶⁹. Figure 29 clearly shows that in order to achieve the same coupling strength as a conventional coupler design, a wider gap between a resonator and a bus waveguide is possible when a pulley coupler is employed. The smaller slope of the curve corresponding to the pulley coupler also suggests improved fabrication tolerance to gap width variations. With such performance constraints reduced, lower cost lithography techniques can be used to fabricate the structures.

5.2.3. Experimental characterizations

As_2S_3 and $\text{Ge}_{17}\text{Sb}_{12}\text{S}_{71}$ microdisks with a radius of 20 μm and varied waveguide-resonator gap separation from 500 nm to 1200 nm have been tested. Table 6 summarizes the optical properties of the resonators, and measured transmission spectra of an As_2S_3 microdisk with a gap separation of ~ 800 nm between bus waveguide and micro-disk is shown in Figure 30 as an example. Notably the cavity Q-factors of As_2S_3 micro-disks is

much higher than those of micro-rings in the same glass composition; this is probably due to the increased interactions of optical modes with sidewall roughness in the case of micro-ring resonators, as is described in the previous section. The transmission spectra feature a set of resonant peaks evenly spaced by a well-defined free spectral range, indicative of single-mode resonator operation. The microdisk operates near critical coupling regime for both TE and TM polarizations around 1550 nm wavelength, an important advantage for applications in the telecommunication bands. The higher Q factor of TM polarization suggests that bending loss is insignificant in the microdisk, and thus it is possible to achieve an even smaller cavity mode volume without suffering excess radiative loss.

Table 6 Coupled cavity Q-factor and free spectral range (FSR) of As_2S_3 and $\text{Ge}_{17}\text{Sb}_{12}\text{S}_{71}$ micro-disk and micro-ring resonators with a 20 μm radius measured at critical coupling (quoted for resonant peaks with extinction ratios > 15 dB) near 1550 nm wavelength.

| Composition and device | Cavity Q ($\pm 10\%$) | | FSR (nm) | |
|---|-------------------------|---------|----------|-----|
| | TM | TE | TM | TE |
| As_2S_3 disk (SU8 clad) | 210,000 | 150,000 | 7.6 | 7.8 |
| As_2S_3 ring (SU8 clad) | 30,000 | 20,000 | 6.2 | 6.7 |
| $\text{Ge}_{17}\text{Sb}_{12}\text{S}_{71}$ disk (in air) | 110,000 | 100,000 | 8.3 | 8.9 |

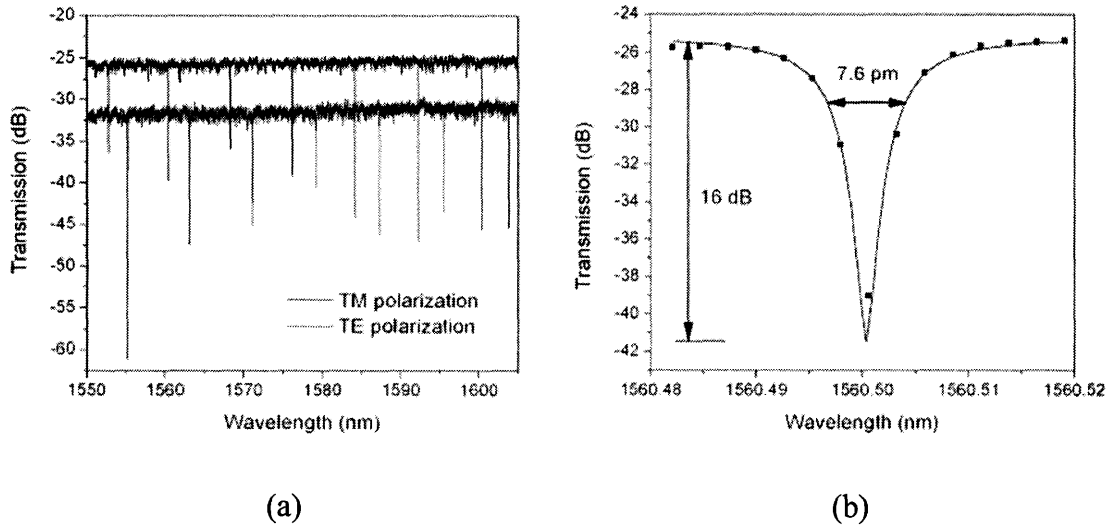


Figure 30 (a) Measured transmission spectra of a 20- μm -radius microdisk resonator; (b) A TM-polarization transmission spectrum averaged over 32 wavelength-sweeping scans near a resonant peak: the black dots are experimental data points and the red curve is the Lorentzian peak fitted in linear scale.

As we can see from Table 6, the whispering-gallery-mode (WGM) in an As_2S_3 microdisk resonators exhibits cavity Q factors as high as 210,000. The Q value represents a 20-fold improvement compared to chalcogenide glass photonic crystal cavities⁹⁹, and is 2.5 times that of Ga:La:S chalcogenide glass microspheres¹⁰⁰.

5.3. Summary

In this chapter, we experimentally demonstrate the first racetrack, micro-ring and micro-disk resonators in chalcogenide glasses, important device platforms for an array of applications that involve photon-matter interactions. The micro-disk resonators exhibit a high Q-factor exceeding 2×10^5 , the highest Q-factor realized in planar chalcogenide glass resonators.

Chapter 6. Design guidelines for optical resonator sensors

As we introduced in Chapter 1, there has been an increased interest in using dielectric optical resonators as miniaturized sensors for detecting surface binding of biological molecules. Despite a large body of published literature on resonator-based sensors, rigorous quantification of their performance matrices has been scarce¹⁰¹. Comparison between different sensor technologies and/or device configurations is impractical due to the absence of a widely accepted figure of merit (FOM). The quantity refractive index (RI) sensitivity, defined as the resonant peak wavelength shift (nm) per unit refractive index change (refractive index unit, RIU), has often been used to quantify surface plasmon resonance (SPR) sensor performance¹⁰², and has also been quoted as a figure of merit for resonator refractometry sensors¹⁰³. However, this criterion fails to take into account factors that can significantly affect resonator sensor performance, in particular resonant peak full width at half maximum (FWHM) which largely affects the wavelength resolution. Refractive index limit of detection (RI LOD), i.e. the minimum resolvable refractive index change of a sensor, offers an alternative description of sensor system performance. It depends on the measurement instrumentation (light source spectral width, which leads to a finite wavelength resolution of light source, and system noise characteristics) as well as on the noise bandwidth in a measurement. For instance, most types of noise can be effectively reduced by applying multiple scan averaging, and therefore even the *same* sensor system can yield very *different* RI LOD values. As a consequence, RI LOD is not an ideal performance measure for comparison between

different sensing technology platforms. Therefore, an appropriate sensor system FOM is highly desirable for performance optimization of optical resonator sensors.

Figure 31 schematically illustrates an optical resonator refractive index sensor *system* we discuss in this paper, which consists of a sensor *device* (a waveguide-coupled optical resonator), a light source, and signal read-out components. Notably here we clearly distinguish a sensor *system* from a sensor *device* for the convenience of discussion.

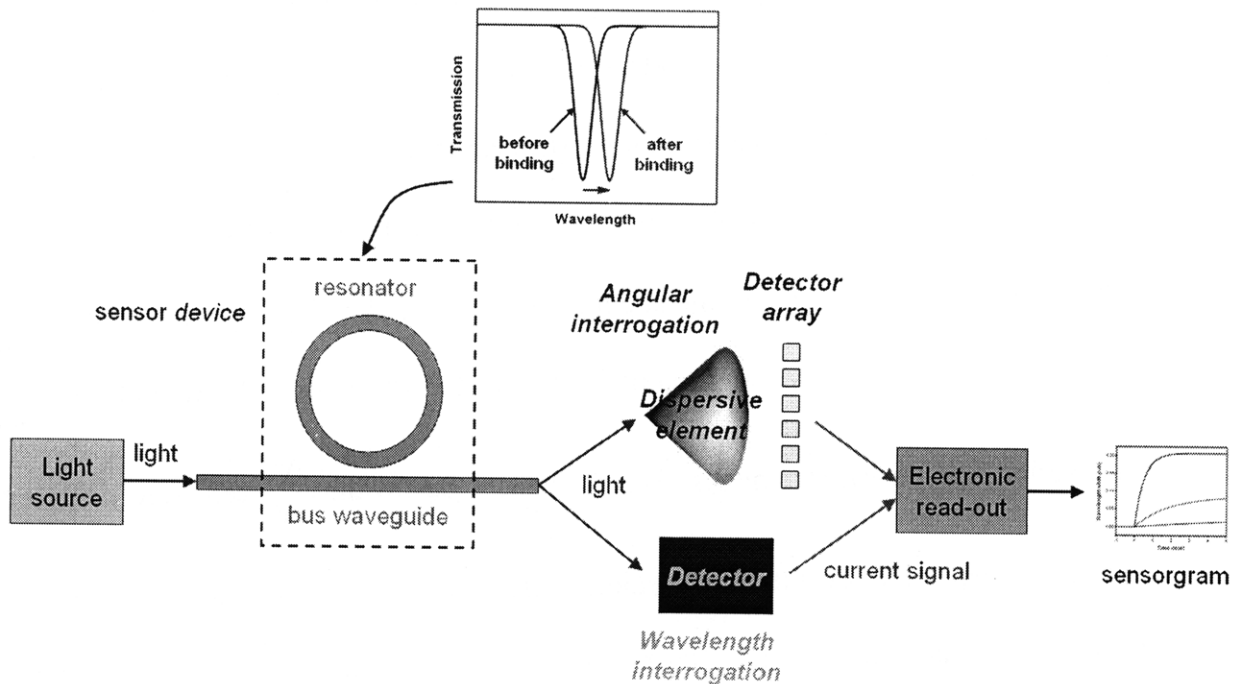


Figure 31 Schematic illustration of an optical resonator sensor system discussed in this paper, comprised of a light source, a coupled optical resonator and read-out components; note that angular and wavelength interrogation schemes employ slightly different configurations; the top inset illustrates the operation principle of refractive index sensors (refractometry).

6.1. Introduction of the time-normalized sensitivity S^*

We define time-normalized sensitivity S^* of a sensor system as inverse of the index change Δn_{\min} that produces a SNR of unity, normalized to square root unit equivalent bandwidth $\frac{\Delta f}{N}$, i.e.

$$\text{Eq. 44: } S^* = \sqrt{\frac{\Delta f}{N}} \cdot \frac{1}{\Delta n_{\min}} = \sqrt{\frac{\Delta f}{2N}} \cdot \frac{\text{Sensitivity}_{RI}}{\Delta \lambda_{\min}} = \sqrt{\frac{\Delta f}{2N}} \cdot \frac{\Gamma_{iv}}{n_g} \cdot \frac{\lambda}{\Delta \lambda_{\min}}$$

with a unit of $\text{Hz}^{1/2}/\text{RIU}$ for refractive index sensors. Importantly, the term “time-normalized” suggests that S^* is independent of noise bandwidth and hence measurement integration time, a necessary feature for a measurement system FOM (similar to detectivity D^* , the FOM for photodetectors). In Eq. 44, n_g is the group index of the resonator mode, λ stands for the operating wavelength, Γ_{iv} represents the optical power confinement factor in the interrogation volume (denoted as iv) since only a fraction of optical energy is interacting with the target molecules, and the $\sqrt{2}$ factor comes in since we are looking into a wavelength shift by taking the difference of two independent transmission spectra measurements. The equivalent bandwidth $\frac{\Delta f}{N}$ can have different expressions depending on the interrogation configuration. Three common interrogation configurations are wavelength interrogation, angular interrogation and intensity interrogation. In a wavelength interrogation scheme, transmission spectra of the resonator sensor are repeatedly measured to determine the time evolution of the resonant wavelength. As shown in Figure 32, a spectroscopic scan of the transmission spectra usually is comprised of transmitted intensity measurements at N discrete wavelength values (and hence the name “wavelength interrogation”). If each transmitted intensity measurement at a single wavelength has an integration time τ and a corresponding single-

measurement noise bandwidth Δf ($\Delta f \sim 2\pi/\tau$), the equivalent bandwidth of the sensor measurement becomes $\frac{\Delta f}{N}$ (with the implicit and usually valid assumption that measurement rate is much smaller than laser scanning rate). In this case, N becomes inversely proportional to resonant cavity Q-factor if the light source spectral width $\delta\lambda_s$ is kept constant, and the definition of equivalent bandwidth eliminates the dependence of S^* on factors not inherent to the sensor system (integration time and light source spectral width), which is verified in our simulations as we will show in the following sections. In contrast, transmitted intensity as a function of wavelength can be measured by a linear array of photodetectors simultaneously provided that the transmitted light is spatially separated via a dispersive element (spatial or angular interrogation), and in this case $N = 1$. Most resonator sensors adopt the wavelength interrogation method, since few dispersive elements are able to attain the wavelength resolution required to characterize a high-Q resonant peak. Finally, we exclude intensity interrogation scheme in our discussion, since it is susceptible to baseline drift (e.g. due to $1/f$ noise) and typically has inferior signal-to-noise ratio compared to the other two configurations.

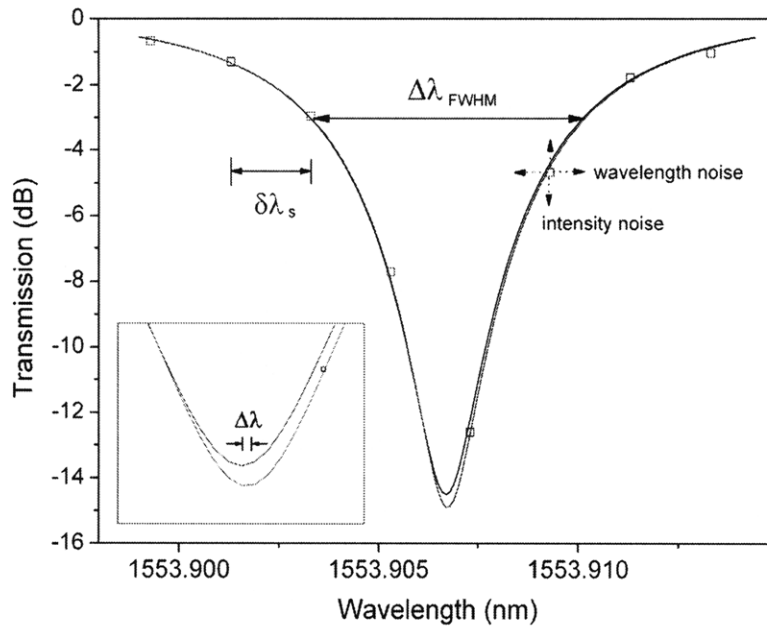


Figure 32 Exemplary transmission spectra of a resonator sensor: The black curve is the analytically calculated spectra obtained using the coupling matrix method. The open squares are the spectral data points obtained, after super-imposing Gaussian-type intensity and wavelength noises using a Monte-Carlo method in the analytical calculation. The open square data points are spaced by a finite spectral width $\delta\lambda_s$. Finally, the red curve is the Lorentzian peak fit based on the data points. The inset shows the analytical and the fitted spectra near their minima: the ensemble average of $\Delta\lambda$ was taken as the minimum resolvable wavelength (wavelength resolution) $\Delta\lambda_{\min}$ of a sensor.

6.2. Noise analysis

We categorize the noise sources into two types: intensity noise and wavelength noise.

6.2.1. Intensity noise and wavelength noise

Intensity noise affects the transmitted optical signal intensity, and wavelength noise leads to a spectral shift of both the incident light signal and the resonant wavelength (see Figure 32). The former category includes photodetector noise, light source intensity fluctuation and possible fiber-to-chip coupling variation, whereas the latter is mainly due

to light source wavelength shift (i.e. source wavelength repeatability) and resonant wavelength change of the optical resonator often due to temperature fluctuations. An implicit assumption in the definition of time-normalized sensitivity S^* is that the sensor system works in a white-noise limited regime, i.e. the noise of the sensor system has no frequency dependence in the noise bandwidth range of interest. Such a noise characteristics can be described with a constant sensor noise spectral density function (NSD, which can be defined as the Fourier transform of the signal autocorrelation function in analogy to power spectral density function in statistical signal processing). For a typical sensor system, the noise bandwidth Δf of transmitted intensity measurement at a single wavelength point usually varies from 100 Hz to 10 kHz depending on the application scenario. Within this bandwidth range the noise spectral density for most of the aforementioned noise sources is approximately constant. In this case, S^* can also serve as a general FOM for many classes of optical sensors, including SPR sensors and fiber-optic sensors. Temperature fluctuations may have non-white noise characteristics depending on the thermal mass and temperature stabilization scheme and therefore need to be considered separately.

6.2.2. Noise simulation results

According to Eq. 44, S^* of a resonator sensor is determined by the minimum wavelength shift $\Delta\lambda_{\min}$ that can be resolved by the system. Therefore, we focus on the impact of resonator parameters and instrumentation factors (light source spectral width and noise characteristics) on $\Delta\lambda_{\min}$. Monte-Carlo simulations are performed for cavity Q-factors in the range of 10^3 to 10^6 , light source spectral width $\Delta\lambda_{\min}$ from 0.01 pm to 10 pm and

different noise amplitude. Details of the simulation methodology are presented in the Appendix II section.

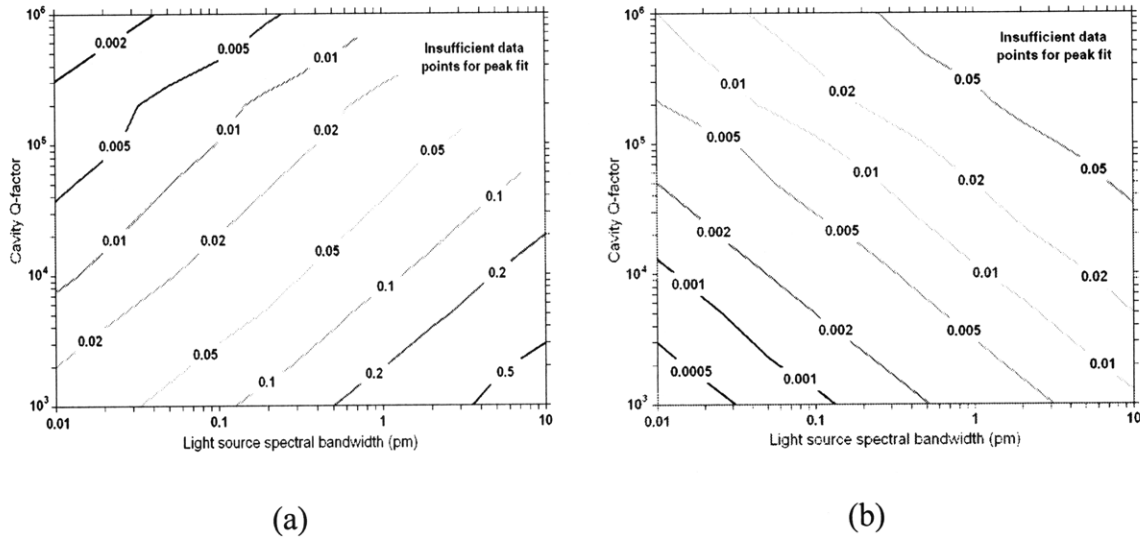


Figure 33 Resonant wavelength resolution $\Delta\lambda_{\min}$ of optical resonator sensors at (a) intensity noise amplitude of 0.1 dB and (b) wavelength noise amplitude of 0.1 pm. The wavelength resolution values can be read out from the iso-resolution curves (unit: pm).

The numerical simulation results are plotted in two design maps in Figure 33. The resonator sensor wavelength resolution $\Delta\lambda_{\min}$ is given at fixed intensity and wavelength noise amplitude of 0.1 dB and 0.1 pm, respectively. Noise-limited resolution at any given noise level can be thereby determined using conclusions (1) and (2) detailed below. The simulation results suggest that it is possible to obtain wavelength resolution much smaller than both the light source line width and resonant peak FWHM using the peak fitting algorithm, provided that wavelength and intensity noises are suppressed.

A few general conclusions can be drawn from the simulation results:

(1) Intensity noise and wavelength noise are orthogonal in terms of their impact on the sensor wavelength resolution $\Delta\lambda_{\min}$, i.e.

$$\text{Eq. 45: } \Delta\lambda_{\min} = \sqrt{\Delta\lambda_{\min, \text{intensity}}^2 + \Delta\lambda_{\min, \text{wavelength}}^2}$$

where $\Delta\lambda_{\min, \text{intensity}}$ and $\Delta\lambda_{\min, \text{wavelength}}$ denote the wavelength resolution when only intensity or wavelength noise is present, respectively;

(2) $\Delta\lambda_{\min}$ is linearly proportional to the noise amplitude for both types of noises;

(3) At a given noise amplitude, $\Delta\lambda_{\min}$ scales with the square root of light source spectral width $\delta\lambda_s$ at a given cavity Q for both types of noises, i.e.

$$\text{Eq. 46: } \Delta\lambda_{\min} \propto \sqrt{\delta\lambda_s} \propto \begin{cases} \sqrt{\Delta\lambda_{FWHM} / N} & \text{wavelength} \\ \sqrt{\Delta\lambda_{FWHM}} & \text{angular} \end{cases}$$

where $\Delta\lambda_{FWHM}$ is the resonant peak spectral width (FWHM), N stands for the number of discrete spectral data points that comprises a spectral scan across the resonant peak, and λ_0 represents the resonant wavelength. Note that the specific form of this expression can be dependent on the interrogation scheme employed. Empirically this proportionality relationship stands for $\delta\lambda_s$ values up to about 20% of the resonant peak FWHM, beyond which the peak fitting algorithm becomes inapplicable since there are too few data points available.

(4) At a given noise amplitude, $\Delta\lambda_{\min, \text{intensity}}$ is inversely proportional to the square root of cavity Q, i.e.

$$\text{Eq. 47: } \Delta\lambda_{\min, \text{intensity}} \propto \frac{1}{\sqrt{Q}} = \sqrt{\frac{\Delta\lambda_{FWHM}}{\lambda_0}}$$

(5) At a given noise amplitude, $\Delta\lambda_{\min, \text{wavelength}}$ is proportional to the square root of cavity Q, i.e.

$$\text{Eq. 48: } \Delta\lambda_{\min, \text{wavelength}} \propto \sqrt{Q} = \sqrt{\frac{\lambda_0}{\Delta\lambda_{FWHM}}}$$

Figure 34, Figure 35 and Figure 36 show some examples of simulation results indicating the functional dependence of wavelength resolution $\Delta\lambda_{\min}$ on noise amplitude, light source spectral width $\delta\lambda_s$ and cavity Q, respectively. Conclusion (1) basically states that intensity noise and wavelength noise are independent and can be separately considered in sensor performance evaluation, and conclusion (2) establishes the linear proportionality between noise amplitude and sensor resolution. Therefore, $\Delta\lambda_{\min}$ and S^* of a given resonator sensor device at any given noise levels can be completely defined if the corresponding values at one arbitrary intensity noise level and at one arbitrary wavelength noise level is determined.

Conclusions (3) can be intuitively understood by noticing that fixed noise amplitude implies the same single-measurement noise bandwidth Δf for transmission measurement at each individual wavelength point comprising a wavelength-sweeping scan. For a resonator with a given cavity Q-factor, smaller light source spectral width $\delta\lambda_s$ means more data points are involved comprising a spectral scan across the resonant peak, giving a more accurate description of the resonant peak. In a wavelength-interrogation scheme,

S^* becomes independent of the source spectral width $\delta\lambda_s$, since the improved wavelength resolution is cancelled out by decrease of equivalent noise bandwidth $\frac{\Delta f}{N}$. However, in a spatial or angular interrogation configuration, the equivalent noise bandwidth remains constant ($N = 1$) and narrow line width sources do lead to S^* improvement.

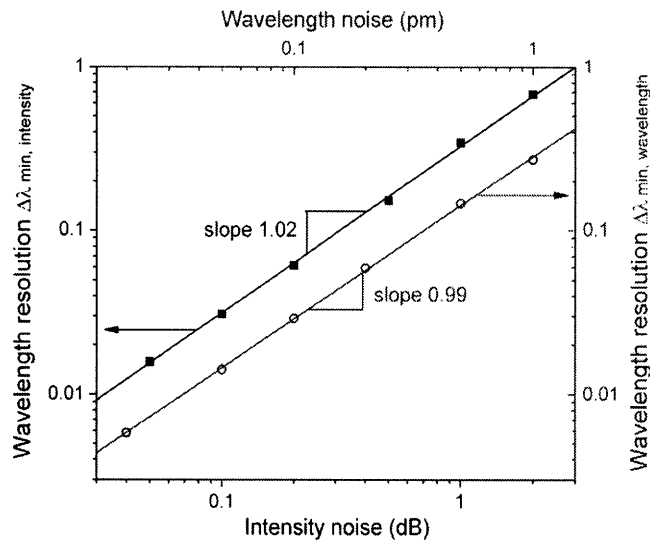


Figure 34 Simulated resonator sensor wavelength resolution $\Delta\lambda_{min}$ at different noise levels, showing linear dependence on noise amplitude for both wavelength and intensity noise: the resonator has a cavity $Q = 10^5$, the light source spectral width $\delta\lambda_s = 1$ pm and both types of noises are of white Gaussian nature.

Conclusion (4) phrases that time-normalized sensitivity S^* is linearly proportional to cavity Q-factor when a wavelength interrogation scheme is used, since N is proportional to the resonant peak FWHM. Intuitively high Q-factor leads to sharp resonant peaks and hence improved wavelength resolution.

Intuitively, wavelength noise translates to intensity noise with increased amplitude in a sharp (high-Q) resonant peak due to the large curve slope involved. Such an intuitive notion is reflected in conclusion (5), which states that high-Q resonator sensors are more susceptible to wavelength noise interference. Moreover, according conclusion (5), S^* of a wavelength-interrogation sensor system becomes independent of cavity Q-factor under wavelength noise-limited operation, which is often associated with scenarios where temperature fluctuation becomes significant. As we will see in the next section, such a limitation eventually imposes a limit to performance improvement by increasing cavity Q-factor.

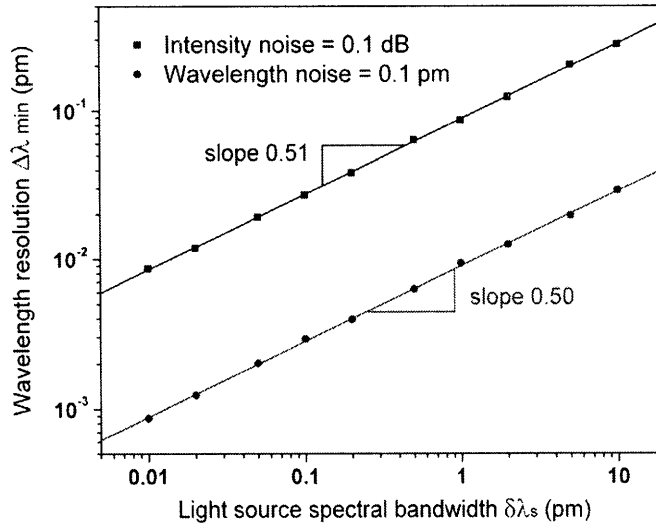


Figure 35 Simulated resonant wavelength resolution ($\Delta\lambda_{min}$) in a $Q = 10,000$ resonator, which is proportional to the square root of light source spectral width $\delta\lambda_s$: the black dots correspond to $\Delta\lambda_{min, intensity}$ at the intensity noise amplitude of 0.1 dB and the red dots correspond to $\Delta\lambda_{min, wavelength}$ at the wavelength noise amplitude of 0.1 pm. Linear fittings are represented by the solid lines.

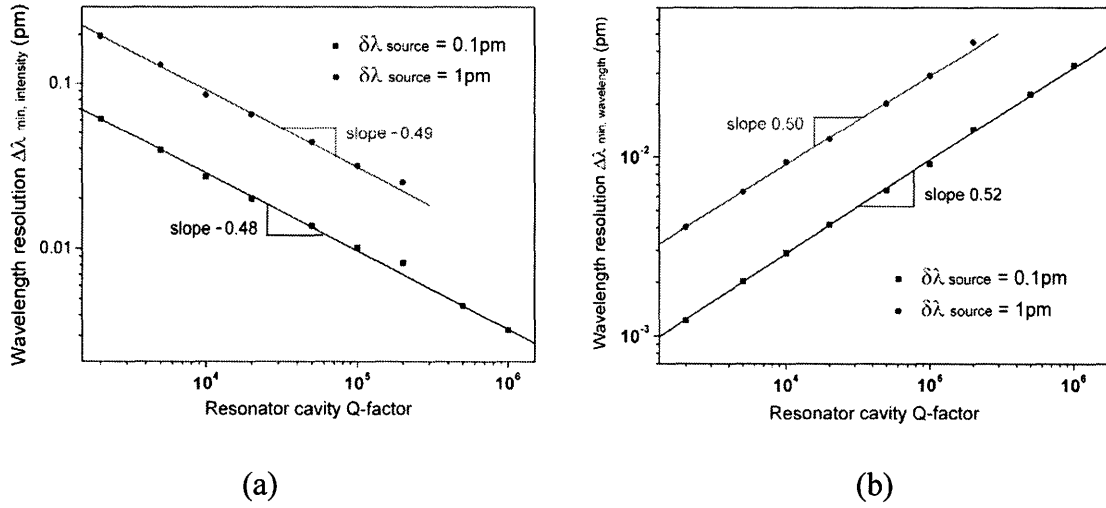


Figure 36 Simulated resonant wavelength resolution ($\Delta\lambda_{\min}$) of resonator sensors with different cavity Q-factors at a given (a) intensity noise amplitude of 0.1 dB and (b) wavelength noise amplitude of 0.1 pm. The dots are simulated $\Delta\lambda_{\min}$ results and the lines are corresponding fitted curves. $\Delta\lambda_{\min}$ is inversely proportional to the square root of resonator cavity Q-factor when the sensor performance is mainly limited by intensity noise; in contrast, $\Delta\lambda_{\min}$ becomes directly proportional to the square root of resonator cavity Q-factor when wavelength noise dominates.

6.3. Design optimization of resonator sensors

6.3.1. Sensor device figure-of-merit

Based on the simulation results, a wavelength-interrogated optical resonator sensor working in the intensity-noise-limited regime can be characterized by a *device* figure of merit solely dependent on resonator parameters:

$$\text{Eq. 49: } FOM = \frac{Q\Gamma_{iv}\lambda_0}{n_g} = 2\pi \frac{\Gamma_{iv}}{\alpha} \propto S^* \quad \text{for wavelength interrogation}$$

where α is the equivalent linear waveguide loss in the cavity and the second equality holds for critically coupled resonators.

Similarly, an intensity-noise-limited *device* FOM can be derived when an angular interrogation configuration is used (in this case $N = 1$):

$$\text{Eq. 50: } FOM = \frac{\sqrt{Q}\Gamma_{iv}\lambda_0}{n_g} \propto S^* \quad \text{for angular interrogation}$$

6.3.2. Parameter dependence of S^*

Table 7 Functional dependence of time-normalized sensitivity on resonator sensor device parameters derived from Monte-Carlo numerical simulations summarizes the functional dependence of S^* on the device parameters in different noise-limited regimes and interrogation schemes, derived from the simulation results presented in the previous section.

Table 7 Functional dependence of time-normalized sensitivity on resonator sensor device parameters derived from Monte-Carlo numerical simulations

| | Wavelength interrogation | | Angular interrogation | |
|---|--------------------------|--------------------------|--|--------------------------|
| | Intensity noise limited | Wavelength noise limited | Intensity noise limited | Wavelength noise limited |
| Cavity Q-factor | $S^* \propto Q$ | → | $S^* \propto \sqrt{Q}$ | |
| Resonance extinction ratio | Weak dependence | Weak dependence | Weak dependence | |
| Light source spectral width $\delta\lambda_s$ | → | → | $S^* \propto 1/\sqrt{\delta\lambda_s}$ | |
| Equivalent measurement bandwidth (integration time) | → | → | → | |

1. → denotes no dependence of S^* on the parameter;
2. Performance of angular-interrogated sensors typically are not limited by wavelength noise due to their large resonant peak width;
3. Noise spectra affect the specific functional form of S^* dependence on extinction ratio

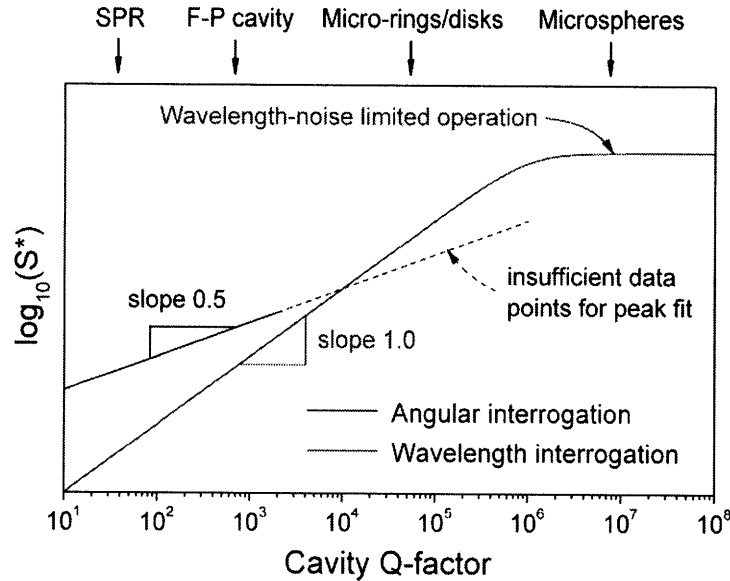


Figure 37 Logarithm of time-normalized sensitivity S^* plotted as a function of cavity Q-factor, assuming: a constant RI sensitivity independent of Q-factor, angular dispersion of dispersive element 0.002 rad/nm, distance between linear photodetector pixel array and the dispersive element 10 cm, pixel linear size 5 μm , device TO coefficient 10^{-6} K^{-1} and operating temperature fluctuation $< 0.01 \text{ K}$. The typical Q-factor values of four different types of resonant structures are indicated by arrows. A moderately high Q-factor ($\sim 10^6$) is sufficient to deliver the desirable wavelength-noise-limited operation (in analogy to background limited performance of infrared detectors).

Table 7 shows that cavity Q-factor is a key parameter determining the sensitivity S^* of resonator sensors. Figure 37 gives an example that illustrates the complex dependence of the logarithm of time-normalized sensitivity S^* on cavity Q-factor in different regimes. Notably, angular interrogation provides improved S^* over wavelength interrogation for low-Q resonator sensors ($Q < 10^3$) whereas wavelength interrogation becomes the preferred configuration for resonator sensors with higher Q-factors ($Q > 10^4$) due to the limited angular dispersion capability. Such an observation is consistent with the fact that most commercial SPR sensor systems adopt the angular interrogation scheme. In addition,

S^* of high-Q resonator sensors is largely bounded by wavelength noise, and a moderately high Q-factor ($\sim 10^6$) is sufficient to deliver wavelength-noise-limited operation (in analogy to background limited performance of infrared detectors).

6.3.3. Origin and mitigation of thermally-induced refractive index fluctuation

In the previous sections, we have focused our discussions on white noises which describe a lot of noise sources such as photodetector noise and light source intensity fluctuation in the bandwidth range of interest. Temperature fluctuation is another important noise source for resonator sensors since it leads to random variation of resonant wavelength. According to conclusion (5), wavelength noise due to temperature fluctuations cannot be alleviated by improving the cavity Q-factor; therefore effectively temperature fluctuations pose a limit to the sensitivity of sensors using high-Q optical resonators. Further, in certain sensor system configurations and application scenarios, a sensor device with finite thermal mass may have a characteristic time constant comparable to the measurement time, and in this case the frequency dependence of noise spectral density becomes significant and needs to be taken into account. The performance of a non-white-noise-limited sensor cannot be appropriately quantified by S^* and a rigorous description involves specifying the noise spectral density of thermal noise and the measurement noise bandwidth. However, a simple estimation can be made based on the thermo-optic properties of the sensor device and the system temperature stabilization/compensation capability using the following formula:

$$\text{Eq. 51: } \Delta n_T = \sqrt{2} \cdot \left(\frac{dn}{dT}\right)_{\text{device}} \cdot \Delta T_{\text{system}}$$

where Δn_T gives the refractive index change resolution limited by temperature noise, $(\frac{dn}{dT})_{device}$ is the thermo-optic coefficient of the optical resonator and ΔT_{system} denotes the average temperature fluctuation with the given temperature stabilization/compensation scheme.

Two approaches can be pursued to reduce Δn_T : using a reference channel in close proximity to the sensor device to provide compensation for the temperature variations, which effectively is equivalent to the reduction of ΔT_{system} . However, this technique requires that the reference channel and the actual sensor device have identical thermo-optic characteristics and yet distinctive response to analyte solution, which is difficult to realize. Therefore this scheme cannot completely eliminate the system temperature sensitivity. Alternatively, it is necessary to decrease the resonator thermo-optic coefficient $(\frac{dn}{dT})_{device}$, which favors dielectric materials with low thermo-optic coefficients over semiconductors as the resonator material. The device TO coefficient for a resonator sitting on a substrate and immersed in water solution is given by the summation of contributions from the resonator itself, the substrate and the solution in the interrogation volume:

$$\text{Eq. 52: } (\frac{dn}{dT})_{device} = \sum \Gamma \cdot (\frac{dn}{dT}) = \Gamma_{core} (\frac{dn}{dT})_{core} + \Gamma_{substrate} (\frac{dn}{dT})_{substrate} + \Gamma_{clad} (\frac{dn}{dT})_{clad}$$

where Γ is the optical confinement factor. In addition, we notice that water has a negative thermo-optic coefficient of -10^{-4} K^{-1} , whereas most dielectric materials have positive thermo-optic coefficients in the range of 10^{-6} to 10^{-4} K^{-1} . Such a combination of TO coefficients with opposite signs allows temperature-insensitive (athermal) designs for

sensors working in an aqueous environment, essentially canceling out the material TO effect. According to Eq. 52, dielectric materials with a moderate positive TO coefficient (on the order of 10^{-5} K^{-1}) is particularly suitable for minimizing the TO coefficient of sensor devices operating in water, while maintaining high optical confinement in the interrogation volume and hence high RI sensitivity without inducing excess radiative loss. It has been experimentally established that athermal designs can decrease the temperature sensitivity of silica waveguide devices up to almost two orders of magnitude compared to devices without such designs¹⁰⁴.

6.3.4. Application to S^* optimization

As an example, let's consider a sensor system comprised of an optical resonator with a moderate cavity Q-factor of 10^5 . When a laser with a spectral line width of 0.1 pm (corresponding to ~ 10 MHz at 1550 nm wavelength, which can be obtained in several types of single-frequency semiconductor lasers such as distributed feedback lasers) is used for wavelength interrogation, Fig. 3a predicts a resonant wavelength resolution of 0.01 pm when the sensor is working in the intensity-noise-limited regime with an intensity noise amplitude of 0.1 dB, equivalent to a signal-to-noise ratio of 16.3 dB. Such a SNR is readily achievable in photonic systems (good photonic link systems can achieve SNR well above 30 dB even at megahertz operation bandwidth¹⁰⁵). Similarly, Fig. 3b points to a wavelength-noise-limited resonant wavelength resolution of 0.01 pm given a wavelength noise amplitude of 0.1 pm. Consider a dielectric material with a TO coefficient of 10^{-5} K^{-1} (similar to that of silica), a resonator sensor can possibly reduce the device TO coefficient to 10^{-6} K^{-1} by incorporating temperature-insensitive designs.

Therefore, if the sensor was to operate in the wavelength-noise-limited regime, it is necessary to stabilize/compensate temperature fluctuations down to < 0.05 K. In resonators with even higher Q-factors (optical resonators with Q-factors exceeding 10^8 have been demonstrated^{65, 66}), temperature control and/or compensation are critical issues that need to be addressed for high-Q optical resonator sensors before their intensity-noise-limited detection capability can be achieved.

Take an RI sensitivity of 200 nm/RIU [21], 0.1 pm wavelength resolution points to a refractive index LOD of 5×10^{-8} RIU and a time-normalized sensitivity $S^* = 2 \times 10^8$ Hz^{1/2}/RIU (assuming an equivalent measurement bandwidth $\frac{\Delta f}{N} = 100$ Hz, a typical value used in our sensor tests), representing at least one to two orders of magnitude performance improvement over SPR sensors. Such high sensitivity is directly attributed to the narrow spectral width of resonant peaks in a high-Q optical resonator (in contrast to the broad resonant band stretching tenths of nanometers wavelength in SPR sensors) and the resulting fine wavelength resolution.

In biological applications, it is often convenient to convert the bulk RI LOD and S^* to observables such as molecular area density, molecular mass LOD or solution concentration¹⁰⁶. If we use human serum albumin (HSA, molecular weight $\sim 66,000$) as a model molecule and a planar glass resonator as the sensing device, 0.1 pm wavelength resolution leads to a molecular area density of approximately 1 pg/cm². Assume a microdisk resonator with a radius of 20 μm , this corresponds to a molecular mass LOD of ~ 13 attograms (~ 120 HSA molecules). Understandably, sensors with small sensing area

are advantageous in achieving a low molecular mass LOD. Nevertheless, small sensing area (e.g. $< 10 \mu\text{m}^2$) often leads to inefficient molecular capturing and large statistical variations of measurement results, design trade-offs that need to be taken into account. Further LOD improvement is possible by reducing system temperature fluctuations and instrument noise figures.

6.4. Experiment

6.4.1. Wavelength resolution dependence on cavity Q-factor

Racetrack, micro-ring, and microdisk optical resonators in $\text{Ge}_{17}\text{Sb}_{12}\text{S}_{71}$ chalcogenide glass with different cavity Q values are used to verify the wavelength resolution predictions shown in Figure 33. Fabrication process of the resonator devices has been described in detail in Chapter 4. The transmission spectra of the fabricated devices are measured on a Newport AutoAlign workstation in combination with a LUNA tunable laser (optical vector analyzer, LUNA Technologies, Inc.). According to the instrument specification, the laser has wavelength repeatability (i.e. wavelength noise amplitude) of 0.1 pm, and the wavelength step size we use in the measurement (i.e. light source spectral width $\delta\lambda_s$) is ~ 2.6 pm. The sample is mounted on a thermostat stage and kept at 25 °C for all measurements. Short-term temperature fluctuation of the thermostat stage is estimated to be < 0.03 °C, corresponding to a temperature-fluctuation-limited RI LOD of $\sim 10^{-7}$ RIU, which is an order of magnitude smaller than intensity-noise-limited RI LOD and is thus not taken into account in the analysis. The transmission spectra through a resonator are measured multiple times, and Lorentzian peak fit is applied to each measured spectrum to derive the resonant wavelength. The experimentally measured resonant

wavelength resolution $\Delta\lambda_{\min}$ is defined as the statistical standard deviation of the resonant wavelength values from each peak fit, and is compared with simulation results taking into account the actual noise characteristics of the measurement instrumentation. Since the amplitude of intensity noise is dependent on the transmitted optical signal intensity in the measurement, experimentally measured noise amplitudes in a single scan and after multiple wavelength-sweeping scan averaging are used in the simulations for direct comparison with experimental results. Our simulations indicate that the resonant wavelength resolution is primarily limited by intensity noise, and thus is inversely proportional to the cavity Q-factor.

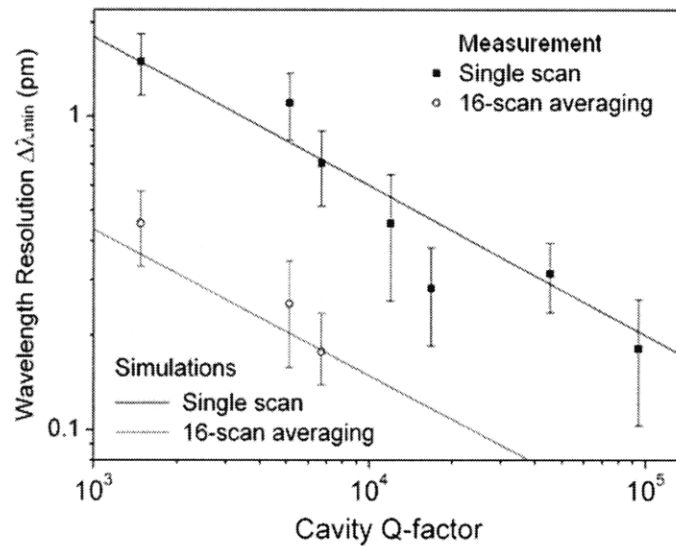


Figure 38 Resonant wavelength resolution $\Delta\lambda_{\min}$ in resonators with different cavity Q-factors: the filled squares are experimentally measured values fitted using transmission spectra from single wavelength-sweeping scans, the open circles are measured values after 16-scan averaging, and the lines are simulation results using the Lorentzian fit algorithm taking into account the actual noise characteristics of the measurement instrumentation.

The experimentally measured resonant wavelength resolution $\Delta\lambda_{\min}$ obtained from single wavelength-sweeping scans and 16-scan averaging is shown in Figure 38, along with the simulation results. Good agreement between experiment and the theoretical predictions supports the validity of our simulation methodology, and confirms the inverse proportionality relationship between $\Delta\lambda_{\min}$ and cavity Q-factor. The four-fold reduction of $\Delta\lambda_{\min}$ after 16-scan averaging as is verified by our measurement indicates that the intensity noise limiting resonant wavelength resolution can be approximated by a white distribution. This result suggests possible further improvement of wavelength resolution and hence refractive index LOD by using increased number of averaging scans before temperature fluctuations become the performance limiting factor.

6.4.2. Impact of humidity and mitigation

We find that the resonant wavelengths of $\text{Ge}_{23}\text{Sb}_7\text{S}_{70}$ resonator are highly sensitive to humidity changes when the uncladded device is exposed to the ambient atmosphere. This sensitivity to humidity is probably due to partial condensation of humidity on resonator surface that leads to the formation of a few water molecule monolayers. To mitigate this issue, all resonators used in refractometry biological sensing are immersed in water prior to testing for ~ 1 hr to stabilize the resonant peak position.

6.5. Summary

In this Chapter, we propose a new refractometry sensor *system* figure of merit: time-normalized sensitivity S^* . Compared to refractive index limit of detection Δn_{\min} , time-normalized sensitivity S^* eliminates the dependence on noise bandwidth, a factor not

inherent to a sensor system. Therefore, S^* is a more appropriate performance measure when comparing different optical sensor technologies.

Based on Monte-Carlo simulations, we show that there are two distinctive operation regimes for optical resonator sensors: intensity-noise-limited operation and wavelength-noise-limited operation. In addition, according to the *device* FOM's Eq. 49 and Eq. 50, which comprising solely of resonator device parameters, cavity Q-factor is the key design variable for improving S^* (Figure 37). Our analysis suggests that resonators with a moderately high Q-factor of $\sim 10^5$ are capable of delivering the desirable wavelength-noise-limited performance (in analogous to background limited operation of photodetectors). We further propose to incorporate temperature-insensitive designs to reduce wavelength noise due to temperature fluctuations. We show through an example that a refractive index LOD of 5×10^{-8} RIU and a time-normalized sensitivity $S^* = 2 \times 10^8 \text{ Hz}^{1/2}/\text{RIU}$ is well within reach of current resonator sensors. Such sensitivity already represents one to two orders of magnitude improvement over SPR sensors, which is attributed to the narrow spectral width of resonant peaks in dielectric resonators and the resulting fine spectral resolution.

We perform experiments to verify the theoretical predictions of resonant wavelength resolution $\Delta\lambda_{\text{min}}$. Good agreement between experiment and simulation is observed, which confirms the validity of our simulation approach and theoretical framework. The impact of humidity is quantitatively evaluated, and a resonant peak stabilization strategy via water immersion is discussed for practical applications.

Chapter 7. Biological sensing using resonator refractometry

In a resonator biosensor, the resonator surface is functionalized with antibodies conjugate to the target molecules to be detected. When the resonator is exposed to liquid samples containing the target species, specific surface molecular binding occurs. The refractive index change resulting from surface molecular binding leads to a resonant frequency change of the optical resonator that can be detected by a photodiode. In this chapter, I will present our results on the sensing performance testing of optofluidic chalcogenide glass resonators.

7.1. Measurement of refractive index sensitivity

Bulk refractive index sensitivity is measured via injecting liquids with different refractive indices into the microfluidic channel and measuring the resonant wavelength shift as a function of liquid index change. In our testing procedure, deionized (DI) water solutions of isopropanol (IPA) of varying concentrations are injected into the channels through a syringe pump, and the resonant peak shift due to ambient refractive index change is monitored *in situ*. The measurements with different concentrations of solutions are repeated twice to confirm reproducibility. TM polarization transmission spectra of a $\text{Ge}_{17}\text{Sb}_{12}\text{S}_{71}$ resonator in IPA solutions of various concentrations are shown in Figure 39(a). The resonant wavelength shift as a function of IPA concentration and corresponding solution refractive index is plotted in Figure 39(b), and a refractive index (RI) sensitivity of (182 ± 5) nm/RIU is inferred from the fitted curve slope. The RI sensitivity can be also predicted using the equation below:

$$\text{Eq. 53: } \text{Sensitivity}_{RI} = \frac{\lambda}{n_g} \times \Gamma_{iv}$$

where λ is the operating wavelength, Γ_{iv} denoted the TM mode power confinement factor in the interrogation volume (water solution in this case) estimated to be 0.204 using finite difference simulations. Based on the simulation results, an RI sensitivity of 194 nm/RIU is predicted. The difference between experimentally measured RI sensitivity and theoretical prediction is probably due to a slight deviation in waveguide dimension from the target design values.

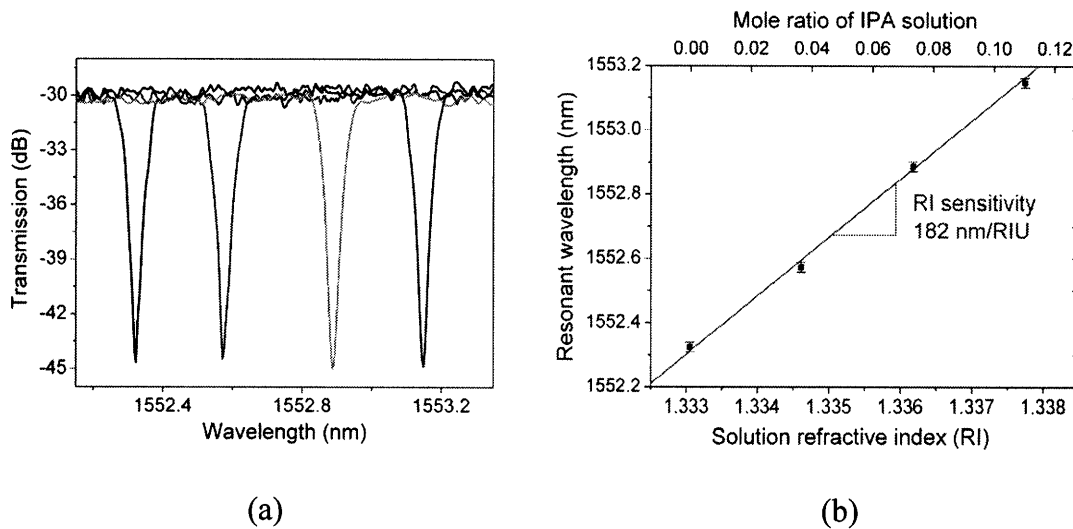


Figure 39 (a) TM polarization transmission spectra of a $\text{Ge}_{17}\text{Sb}_{12}\text{S}_{71}$ microdisk in IPA solutions with four different concentrations; (b) Measured resonant peak wavelength shift as a function of IPA solution mole ratio concentration and corresponding solution refractive index.

By applying a Lorentzian fit to the resonant peaks, we show that the resonant wavelength can be determined to an accuracy of ~ 0.1 pm limited by noise. Besides resonant wavelength shift, we observed that the cavity Q-factor decreased from 110,000 to 20,000 after solution injection, which can be directly attributed to the optical absorption of water.

Using the absorption coefficient of water at 1550 nm wavelength ($\alpha = 9.6 \text{ cm}^{-1}$)¹⁰⁷, we estimate the absorption-limited Q-factor to be $\sim 19,000$, in excellent agreement with our measurement result. By shifting the operating wavelength to near infrared water transparency windows (e.g. 1.06 μm wavelength), we can expect minimized Q deterioration due to water absorption, which should lead to much higher sensor sensitivity.

7.2. Quantitative theory of molecular binding and resonant wavelength shift

The resonant wavelength shift is directly proportional to the additional polarizability of molecules bound on the resonator. Assuming that the polarizability of a single molecule in water solution is α , the resonant wavelength shift of a resonant cavity $\Delta\lambda_s$ when a single molecule is bound onto its surface is:

$$\text{Eq. 54: } \Delta\lambda_s = \frac{\lambda_r |E|^2}{2L \cdot \int \epsilon_c |E|^2 ds} \cdot \alpha$$

where λ_r is the unperturbed resonant wavelength, ϵ_c is the dielectric constant (distribution) of the resonant cavity, E is the resonant mode electric field, L the cavity length, and the integration in the numerator is carried out over the whole resonant cavity cross-section (including evanescent field). If we assume that the protein geometrical conformation in water can be approximated by a spherical shape with a volume V_p , the polarizability of a single molecule can analytically given by¹⁰⁸:

$$\text{Eq. 55: } \alpha = \frac{\epsilon - \epsilon_m}{\epsilon + 2\epsilon_m} \cdot 3\epsilon_m V_p$$

Here ϵ_m and ϵ correspond to the dielectric constant of water and protein molecule, respectively.

Now if we consider a resonator surface with a binding site density of N (in $1/\text{m}^2$ for SI units), the maximum resonant wavelength shift $\Delta\lambda_m$ will be:

$$\text{Eq. 56: } \Delta\lambda_m = N \cdot A \cdot \Delta\lambda_s = N \cdot A \cdot \frac{\lambda_r |E|^2}{2L \cdot \int_S \epsilon_c |E|^2 ds} \cdot \alpha$$

where A denotes the sensing area of the resonator device. $\Delta\lambda_m$ gives the resonant wavelength shift when the concentration of protein in the solution is sufficiently high so that all binding sites are occupied. When the protein concentration is low, we write the fraction of binding sites occupied as f , which is determined by the protein concentration c (given in mol/L) and the affinity constant a_c of the antibody receptor on the resonator surface. If we neglect the depletion of proteins in the solution due to binding to sensor surface (i.e. when the solution concentration remains a constant during the binding process), when the binding reaction reaches equilibrium we have:

$$\text{Eq. 57: } a_c = \frac{f}{(1-f) \cdot c}$$

Solving for f from Eq. 57, we have:

$$\text{Eq. 58: } f = \frac{a_c c}{a_c c + 1}$$

Therefore, the wavelength shift as a function of protein concentration can be given by:

$$\text{Eq. 59: } f \cdot \Delta\lambda_m = \frac{a_c c}{a_c c + 1} \cdot \frac{\lambda_r |E|^2}{2L \cdot \int_S \epsilon_c |E|^2 ds} \cdot N \cdot A \cdot \alpha$$

Note that since we neglect protein depletion in the analyte solution, Eq. 59 only applies when the solution contains sufficient protein molecules so that the amount of bound protein on sensor surface is negligibly small. Mathematically, this condition translates to:

$$\text{Eq. 60: } N \cdot A \ll N_A \cdot c \cdot V_s$$

where V_s is the volume of analyte solution used in the test, and N_A is the Avogadro constant. Eq. 60 holds in two scenarios: 1) the sensor has a small sensing area; or 2) the analyte transport to the sensor works in a continuous flow mode, or in other words, the solution over the sensor is constantly replenished. When these conditions are not met, we have to re-derive Eq. 58 under the constraint:

$$\text{Eq. 61: } (c - c') \cdot V_s \cdot N_A = f \cdot N \cdot A$$

Here c' denotes the solution concentration after the binding-dissociation equilibrium is attained. Solve for f using Eq. 61 in conjunction with the chemical equilibrium condition, we obtain:

$$\text{Eq. 62: } a_c = \frac{f}{(1-f) \cdot c'} = \frac{fV_sN_A}{(1-f) \cdot (cV_sN_A - fNA)}$$

The f solved from Eq. 62 can then be used to calculate the resonant wavelength shift $f \cdot \Delta\lambda_m$. As we will see in the next section, the resonant peak shift is clearly divided into two regions: a linear region for low protein concentrations and a plateau regime for high concentrations. In the former regime, $f \ll 1$, and Eq. 62 can be approximated by:

$$\text{Eq. 63: } a_c = \frac{fV_sN_A}{cV_sN_A - fNA}$$

This leads to a linear functional dependence of f on the solution concentration c :

$$\text{Eq. 64: } f = \frac{a_c V_s N_A}{a_c N A + V_s N_A} \cdot c$$

In the latter case, $f \sim 1$, and Eq. 62 becomes:

$$\text{Eq. 65: } f = 1 - \frac{V_s N_A}{a_c (c V_s N_A - N A)}$$

Clearly, f approaches unity as the solution concentration c is sufficiently large.

7.3. Protein detection test

7.3.1. Glass surface functionalization

We use aldehyde chemistry to functionalize the surface of resonators for protein binding. The procedures start with coating the chalcogenide glass resonator with a thin layer of silicon oxide (30 ~ 50 nm). Prior to surface chemistry treatment, the chips are spin-coated with SU8 polymer and windows (typically of a size 100 μm \times 100 μm) are opened at the resonator locations. The purpose of such a step is to limit the surface functionalization region on the chips and avoid unnecessary waste of antigens due to binding at locations other than the resonator surface; further, the coating also improves the robustness of resonator devices. The oxide surface is then grafted with amine or carboxyl group termination. The surface is then activated in glutaraldehyde, followed by antibody coupling using a surplus of sodium cyanoborohydride and antibody (from Abcam Inc.) solutions. Finally, unreacted aldehyde surface groups are passivated by reaction with a blocking buffer (ethanolamine).

During the testing, serial dilutions of protein solutions are either pipetted down on the chips or injected into the microfluidic channels in a continuous flow mode, and the resonant wavelength change is monitored in-situ.

7.3.2. Prostate specific antigen testing

We selected prostate specific antigen (PSA) as the target species for our test. PSA has been clinically verified as a biomarker for prostate cancer in men; and PSA tests using ELISA have become a widely accepted early screening technique for prostate cancer.

Clinically when the concentration of PSA in human blood is greater than 4 to 10 ng/mL, it possible suggests elevated risk of prostate cancer.

In the test, serial dilutions in phosphate buffer (pH = 7.4) of PSA protein is prepared at nominal concentrations of 0.5, 2, 5, 20, 50 ng/mL. Prior to protein tests, the resonator is immersed in phosphate buffer solution for ~ 1 hour until the resonant peak position is stabilized. The solution is then pipetted onto the antibody-coated resonator and the resonant wavelength change is monitored. During the tests, the solution on resonator is replenished at 10-minute intervals due to evaporation. The total amount of solution used in each serial dilution test is ~ 120 μ L.

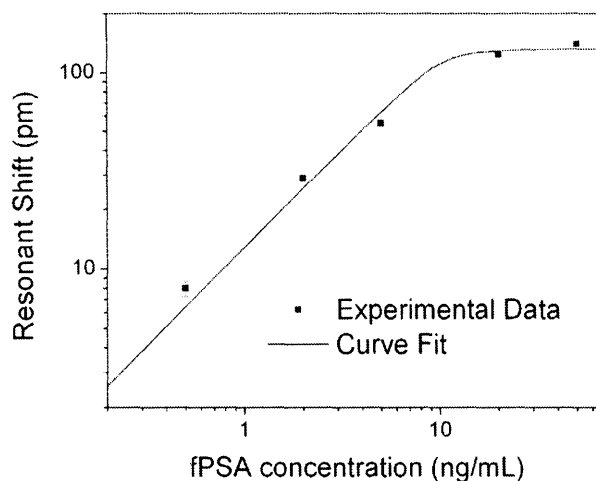


Figure 40 Resonant wavelength shift due to binding in PSA solutions with different concentrations; the wavelength shift is taken as the value record ~ 70 min after solution application and after buffer solution wash. The red curve is fitted using Eq. 62.

Figure 40 shows the resonant wavelength shift due to binding in PSA solutions with different concentrations; the wavelength shift is taken as the value record ~ 70 min after

solution application and after buffer solution wash. The experimental data are fitted to a theoretical curve using Eq. 62 with excellent agreement.

Table 8 Fitting parameters used for PSA measurement data

| Affinity constant | Molecular weight | Molecular density | Refractive index of molecule |
|-------------------|------------------|--------------------------------------|------------------------------|
| 10^{11} L/mol | 34,000 Da | 1.0 g/cm ³ (estimated) | 1.5 (estimated) |

The relatively long waiting time is due to the slow molecular diffusion from the bulk of the solution to the resonator surface. The diffusion time t can be estimated by:

$$\text{Eq. 66: } t \sim \frac{L^2}{2D}$$

where L is the length scale of the bulk solution (~ 1 mm), and D is the diffusion coefficient of PSA molecule. A simple estimation of diffusion coefficient of macromolecules can be made using the Stokes-Einstein law:

$$\text{Eq. 67: } D = \frac{k_B T}{6\pi\eta r}$$

where k_B is the Boltzmann constant, T is the temperature in Kelvin, η is water viscosity, and r is the effective radius of molecule. The calculated diffusion time in our tests is in the order of 1 hour, which determines the waiting time in our experiments. This long waiting time can be reduced by using a microfluidic design (Chapter 4) and is not intrinsic to our resonator device. As we can see from Figure 40, the resonant peak shift saturates at high PSA concentrations, which is an indication of complete occupation of binding sites on the resonator surface. This is consistent with our analysis in the previous section. Based on the noise floor measured in the tests (~ 0.8 pm), we can extract an

detection limit down to 0.05 ng/mL, which compares favorably with the detection limit of ELISA tests (~ 0.2 ng/mL). Cross-reactivity is tested by performing the same test with human serum albumin protein (HSA, from Sigma-Aldrich) solution at concentrations up to 50 $\mu\text{g/mL}$. No significant resonant peak shift is observed after buffer wash.

7.3. Summary

In this chapter, we performed tests to confirm the biological sensing capability of the chalcogenide glass resonator sensors. The resonators are measured to have a refractive index sensitivity of 182 nm/RIU and a detection limit of refractive index change down to 8×10^{-7} RIU.

A theoretical framework relating resonant wavelength shift to the concentration of protein analyte solution is established. We show that the functional dependence of resonant peak shift on protein concentration is divided into two regimes, a linear regime where the shift is proportional to the concentration and a saturation regime where most binding sites are occupied by the protein molecules.

We use the resonator to detect PSA in buffer solutions. The detection limit of the test is estimated to be ~ 0.05 ng/mL, which compares favorably with the detection limit of ELISA tests (~ 0.2 ng/mL).

Chapter 8. Infrared absorption spectroscopy

In this chapter, we will describe our work on the development of chip-based, miniaturized photonic devices for infrared absorption spectroscopy. The emphasis will be placed on two types of devices: an microfluidic waveguide evanescent sensor, and a chalcogenide glass optofluidic resonator for resonant cavity enhanced infrared absorption spectroscopy. While the former device draws an direct analogy to conventional free-space infrared spectrophotometer and is physically simple, and latter type of device combines small device footprint with improved sensitivity, a design that is highly appropriate for future generations of on-chip spectrophotometers.

8.1. Waveguide evanescent wave sensor

8.1.1. Theory

The theory of a waveguide evanescent sensor is relatively straightforward. In the configuration we have adopted, the minimum detectable medium absorption coefficient change α_e can be derived by comparing the sensor signal (output power decrease due to analyte absorption) to noise (signal output fluctuations) and thus is given as follows:

$$\text{Eq. 68: } \alpha_e = \frac{1}{L} \cdot \frac{\sqrt{2}}{\Gamma_{iv}} \sqrt{\left(\frac{\Delta F_0}{F_0}\right)^2 + \left(\frac{\sigma_j}{RF_0 \exp(-\alpha L)}\right)^2}$$

where R is the photodetector responsivity, F_0 is the input laser photon flux coupled into the waveguide, α stands for intrinsic waveguide loss not considering analyte absorption, L represents the length of the waveguide immersed in analyte solution, Γ_{iv} represents the waveguide power confinement factor in solution (i.e. the interrogation volume), and σ_j denotes dark current noise from the detector.

The terms in Eq. 68 under the square root correspond to two major noise sources: input laser power fluctuation and photodetector noise at the output. The latter term is of significance only when the analyte solution has strong absorption or is highly concentrated, which limits the dynamic range of detection. The former term, i.e. fluctuation of input laser power, primarily stems from the spatial shift of input/output fibers in our case, which leads to approximately a 5% fluctuation of optical power effectively passing through the analyte solution.

Importantly, as we can see from Eq. 68, the detection limit of analyte absorption coefficient α_e is inversely proportional to the optical path length L : this relation suggests that in order to increase the waveguide evanescent sensor sensitivity, it is necessary to use a design with a long optical path length, a situation similarly faced by conventional single-pass spectrophotometers as we mentioned in Chapter 1. To resolve this apparent physical limit, we need to resort to cavity enhanced absorption spectroscopy, as we will describe in section 8.2.

8.1.2. Experiment

In this demonstration, channel waveguides with a 6 μm width and a 400 nm height were defined using traditional lithography, and patterned subsequently via SF_6 plasma etching. An SU8-PDMS hybrid microfluidic channel structure is subsequently fabricated on top of the chalcogenide glass waveguide to complete the sensor chip fabrication. Details of the plasma etching process and the hybrid microfluidic channel fabrication are provided in

Chapter 4. Figure 41 shows a photo of the assembled microfluidic chip with fluid inlet and outlet tubing.

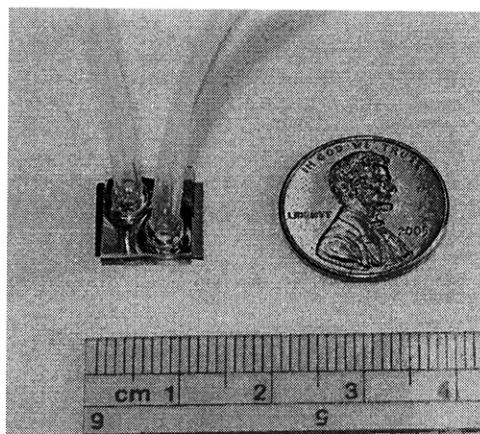


Figure 41 Photograph of the assembled microfluidic chip with fluid inlet and outlet tubing; the microfluidic channels and $\text{Ge}_{23}\text{Sb}_7\text{S}_{70}$ waveguides are too small to resolve in the image.

A small film thickness is desirable, since a large fraction of the optical power then strays outside the glass core as an evanescent field. Since the waveguides have a small core height of 400 nm (compared to the 1550 nm wavelength), the interaction of the optical mode with the fluidic analyte surrounding the waveguide is enhanced, leading to improved sensitivity of the evanescent sensor. For this reason, $\text{Ge}_{23}\text{Sb}_7\text{S}_{70}$ film has been deposited with a $400 \text{ nm} \pm 2.5\%$ thickness across the entire 6" wafer. The thickness of the film was measured using a Tencor P10 surface profiler. Using a Metricon 2010 Prism Coupler, the refractive index of the as-evaporated film was determined to be (2.24 ± 0.02) at 1550 nm.

$\text{Ge}_{23}\text{Sb}_7\text{S}_{70}$ waveguide transmission loss was measured using paper-clip waveguide patterns defined on the same wafer as the sensor devices. The loss measurement yielded a

transmission loss of (2.3 ± 0.3) dB/cm at 1550 nm wavelength for as-fabricated channel waveguides.

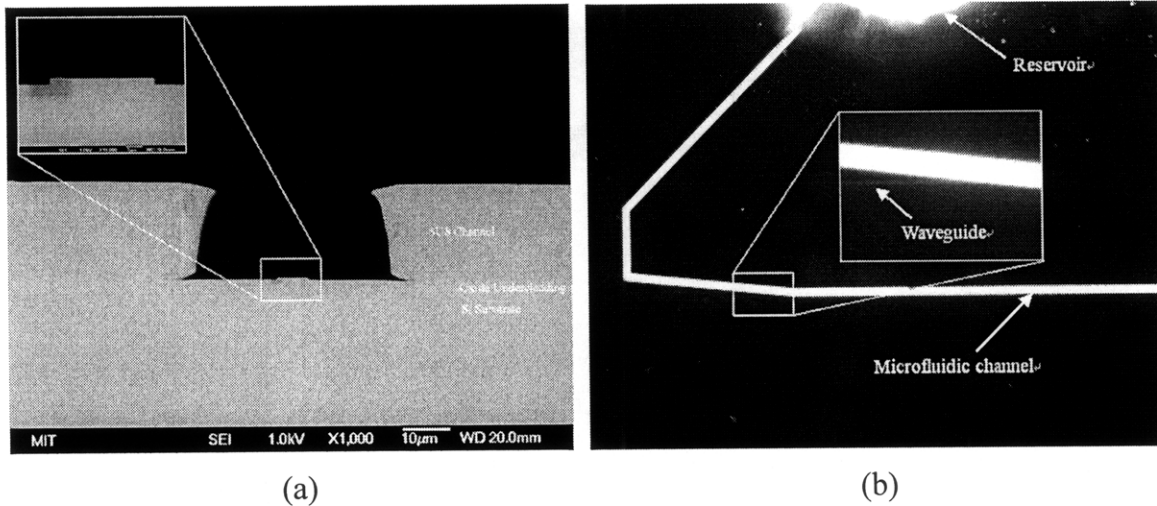


Figure 42 (a) SEM cross-section of a 50 μm wide SU8 microfluidic channel before being capped with a PDMS cover; Insets: the high magnification cross-sectional micrographs of the $\text{Ge}_{23}\text{Sb}_7\text{S}_{70}$ waveguides formed by SF_6 plasma etching sitting at the bottom of the channel, showing a vertical sidewall profile. The slightly darker area on the left side is an artifact due to electronic charge accumulation during SEM observation; (b) Fluorescent image of a microfluidic channel filled with FITC (fluorescein isothiocyanate) solution on a sensor chip, indicating successful fluid injection into the channel free of leakage.

SEM cross-sectional images (taken on a JEOL 6320FV field-emission high-resolution SEM) of the waveguides in Fig. 4(a) exhibited a vertical sidewall profile and excellent feature size fidelity. In order to test the mechanical strength of the bonding between SU8 channels and the PDMS cover, FITC (fluorescein isothiocyanate, green fluorescence emission at 525 nm wavelength) solution was injected into the capped channels via pressure applied using a syringe. A fluorescence image in Fig. 4(b) (taken on an Olympus

BX51 fluorescence microscope) indicates that the solution successfully filled the channels without leakage.

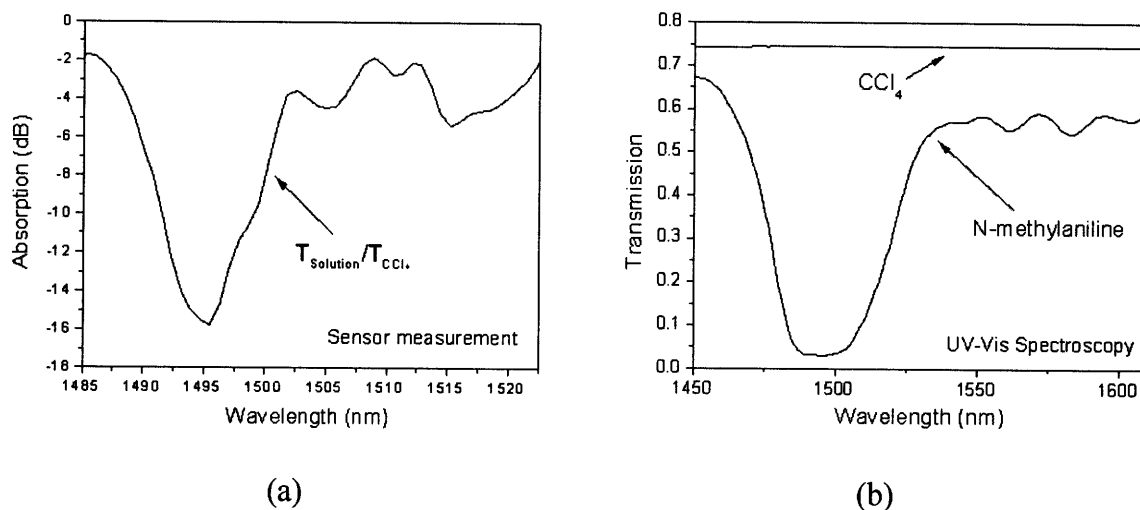


Figure 43 (a) Absorption spectrum showing the N-H bond absorption at 1496 nm wavelength in N-methylaniline measured using our integrated evanescent sensor. The absorption is defined by taking the ratio of light transmission in the case of a microfluidic channel filled with pure carbon tetrachloride against the case when the channel is filled with N-methylaniline solution in carbon tetrachloride (0.33, volumetric concentration). (b) Transmission spectra of pure N-methylaniline and carbon tetrachloride (CCl₄) measured using traditional UV-Vis spectroscopy. The absorption spectrum of N-methylaniline shows the same N-H absorption peak near 1496 nm while carbon tetrachloride is transparent in the wavelength range of interest.

Sensor performance was tested by monitoring the optical output while injecting a solution of N-methylaniline mixed with a solution of carbon tetrachloride into the microfluidic channel. The N-H bond in N-methylaniline is known to exhibit an absorption peak near 1500 nm¹⁰⁹, which was used as the characteristic fingerprint for chemical identification in our test. The absorption (in dB), αL , induced by N-methylaniline in our microfluidic channel was calculated by taking the ratio of light intensity transmitted through a

microfluidic channel filled with pure carbon tetrachloride (I_{solvent}) and through a channel filled with N-methylaniline solution in carbon tetrachloride (I_{analyte}) (0.33, volumetric concentration), i.e.:

$$\text{Eq. 69: } \alpha L = 10 \log_{10} \frac{I_{\text{solvent}}}{I_{\text{analyte}}}$$

with L the length of the waveguide immersed in analyte solution (cm). The same waveguide was used throughout the experiment to eliminate any uniformity issue associated with waveguide intrinsic loss. The resultant absorption spectrum shown in Figure 43 exhibits a well-defined absorption peak at 1496 nm, which is in excellent agreement with a traditional absorption measurement carried out on a Cary 5E UV-Vis-NIR dual-beam spectrophotometer. As is seen in Figure 43, since carbon tetrachloride has no absorption band and is transparent in the investigated range, this spectral peak is unambiguously assigned to N-H bond vibrational absorption.

The peak absorption in dB at 1496 nm was measured for different concentrations of N-methylaniline solution in carbon tetrachloride and the result is shown in Figure 44. The excellent linear fit suggests that the sensor exhibits linear response when varying analyte concentrations in the range investigated.

Moreover, the absorbance at 1496 nm of a solution with a concentration of 0.33 volume % has been determined to be ~14.3 dB (signal) according to Fig. 5(a). As seen in Fig. 6, the sensor response is linear with concentration, and thus the absorption peak height scales with concentration. For this reason, at concentration x, the absorbance (dB) will be given by $14.3 \cdot (x/0.33)$. The noise induced by the power fluctuations has been estimated

to be ~5% which corresponds to 0.21 dB. The minimum detectable concentration (denoted by x here) is reached when the signal is equal to the noise. For this reason, the sensor sensitivity to N-methylaniline in carbon tetrachloride is estimated to be 0.7% (given by $14.3*(x/0.33) = \sqrt{2}*0.21$) by comparing the absorption peak height (signal) with fiber output power. The lower limit actually measured in our experiment is 6.25% volumetric concentration.

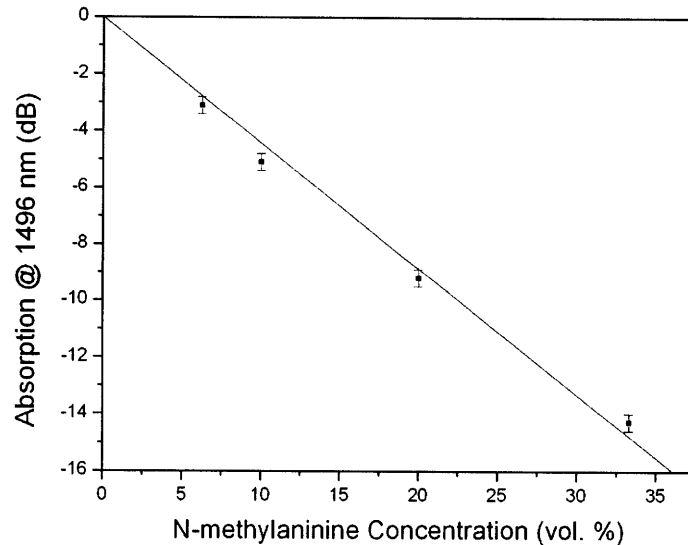


Figure 44 Peak absorption of N-methylaniline solution in carbon tetrachloride measured using the waveguide evanescent sensor as a function of N-methylaniline volume concentration, indicating good linearity of the sensor response.

8.2. Resonant cavity enhanced infrared absorption spectroscopy

8.2.1. Theory

The transmission spectra through a waveguide-coupled resonant cavity can be generically derived using two mathematically equivalent approaches: the coupled mode theory⁶⁹ or the generalized coupling matrix formalism⁶⁸. When the resonant condition is met, the

power transmission coefficient T (in dB) measured from the output end of the bus waveguide can be written as:

$$\text{Eq. 70: } T(\text{dB}) = 10 \cdot \log_{10} \frac{(\sqrt{A_i A_e} - \sqrt{1 - |k|^2})^2}{(1 - \sqrt{A_i A_e} \cdot \sqrt{1 - |k|^2})^2}$$

where k is the amplitude coupling coefficient from the bus waveguide to the resonator, $A_i A_e$ represents round-trip transmission coefficient around the resonator (i.e. $1 - A_i A_e$ corresponds to the round-trip fractional energy loss inside the resonator), and the contributions from intrinsic resonant cavity optical loss and analyte solution absorption are denoted as A_i and A_e , respectively. The intrinsic linear optical loss α_i in a resonator of physical length L is related to A_i by:

$$\text{Eq. 71: } \alpha_i = -\frac{1}{L} \ln A_i$$

The values of k and A_i can be analytically solved using the generalized coupling matrix approach from the transmission spectra of the resonator in pure solvent. Since the refractive index change from pure solvent to analyte solution is relatively small in our experiment ($\Delta n < 0.01$), the coupling coefficient k can be practically regarded as a constant. The experimentally fitted k values typically differ by less than 2% before and after analyte solution injection in our tests, which confirms this assumption.

The additional optical loss due to introduction of analyte α_e can be solved by linearizing the equation above near $\Delta T = 0$:

$$\text{Eq. 72: } A_e = 1 - 0.23 \cdot \left[\frac{(A_i + 1) \cdot \sqrt{1 - |k|^2} - 2\sqrt{A_i}}{\sqrt{A_i} \cdot |k|^2} + 1 \right] \cdot \Delta T$$

and ΔT is the change of resonant peak extinction ratio in dB. The linear optical extinction coefficient α_e of the analyte solution can then be analytically represented as:

$$\begin{aligned} \Gamma \cdot \alpha_e &= -\frac{1}{L} \ln A_e \\ \text{Eq. 73: } &= 0.23 \cdot \frac{1}{L} \cdot \left[\frac{(A_i + 1) \cdot \sqrt{1 - |k|^2} - 2\sqrt{A_i}}{\sqrt{A_i} \cdot |k|^2} + 1 \right] \cdot \Delta T \\ &= \frac{1}{S} \cdot \Delta T \end{aligned}$$

where

$$\text{Eq. 74: } S = 0.434 \cdot L \cdot \left[\frac{\sqrt{A_i} \cdot |k|^2}{(A_i + 1) \cdot \sqrt{1 - |k|^2} + \sqrt{A_i} \cdot (|k|^2 - 2)} \right]$$

and Γ denotes the confinement factor in the solution¹¹⁰, which can be numerically computed based on the resonator dimensions.

The equations above correlate the absorption coefficient of solution α with the experimental observable ΔT . The factor $\Gamma \cdot S$ can be defined as the “effective sensitivity” of the device, which specifies the extinction ratio change per unit solution absorption increase. Therefore, we can infer from the equations that three factors contribute to detection limit improvement of resonator absorption sensors: fine resolution of extinction ratio change ΔT , high optical confinement Γ in the solution, and a large S factor which parametrically depends on intrinsic and extrinsic optical loss of the resonator (α_i and k , respectively).

Based on the discussion, here we use Monte-Carlo simulations to quantitatively evaluate cavity-enhanced sensor design optimization towards improved detection limit of optical

absorption in solutions. We note that even relatively small refractive index change in the solution leads to significant resonant wavelength shift, usually in a short time frame (< 1 s). For example, even a refractive index change of 0.001 can lead to a resonant wavelength shift in the order of 1 nm (~ 200 GHz), almost 100 times that of the resonant peak 3dB bandwidth. Such a large peak shift can pose a challenge to active locking of the probing wavelength to the resonant peak. Further, accurate aligning of the probing wavelength to the exact resonant wavelength can be technically difficult in high-Q resonators given the narrow spectral width of resonance. Instead, we adopt a wavelength interrogation scheme in our simulations and experiments. In a sensor measurement, transmission spectra of the resonator are monitored *in situ*, and the resonant peak extinction ratio is tracked to detect the presence of optical absorption in the solution. In a typical step spectral scan, the transmission spectrum actually consists of data points at discrete wavelength values, usually evenly spaced by a step size $\Delta\lambda_s$. In order to simulate the impact of measurement noise in this wavelength-interrogation process, a Monte-Carlo approach is employed to predict the resolution of extinction ratio change ΔT . Randomly generated Gaussian-type white noise is superimposed onto the spectral data points calculated using a generalized coupling matrix method. We then perform a Lorentzian fit to the data points in a linear scale near a resonant peak to extract the peak parameters including extinction ratio. The minimum resolvable extinction ratio change ΔT_{\min} is statistically defined as the ensemble average of deviations of the “measured” values from the actual resonant wavelength over 1,000 Monte-Carlo iterations. Relative numerical error arising from the random nature of the Monte-Carlo method was estimated to be $\sim \pm 5\%$. More details of the simulation method are described in Appendix II. Since the factor

S and confinement factor Γ can be calculated using given device parameters, the detection limit of solution optical absorption α can be calculated by substituting the simulated ΔT_{\min} value into Eq. 73.

Our simulations indicate that there are four factors affecting the detection limit of resonant cavity-enhanced optical absorption sensors, represented by $\Gamma \cdot \alpha$, the product of confinement factor in the solution, and the minimum detectable solution optical absorption to achieve a signal-to-noise ratio of unity: the wavelength step $\Delta \lambda_s$ used in a spectral scan across the resonant peak; the signal-to-noise ratio (SNR) of resonator transmission measurements at each discrete wavelength point, which is proportional to the square root of integration time in a white noise limit; the intrinsic linear optical loss inside the resonator (e.g. due to roughness scattering or absorption of the resonator material); and the ratio between extrinsic loss (i.e. cavity loss arising from coupling to bus waveguides) and the intrinsic optical loss. The former two factors are related to the measurement instrumentation, whereas the latter two are intrinsic properties of the optical resonator.

According to the simulation results, the detection limit $\Gamma \cdot \alpha$ of absorption sensors is proportional to the square root of the spectral scan wavelength step $\Delta \lambda_s$. Intuitively, spectral scans with fine wavelength steps provide a more accurate description of the transmission spectra and hence smaller ΔT_{\min} ; more rigorous analysis shows that this is a direct consequence of the white noise distribution used in our Monte-Carlo simulations, an assumption that holds for most types of noise sources in a spectral measurement.

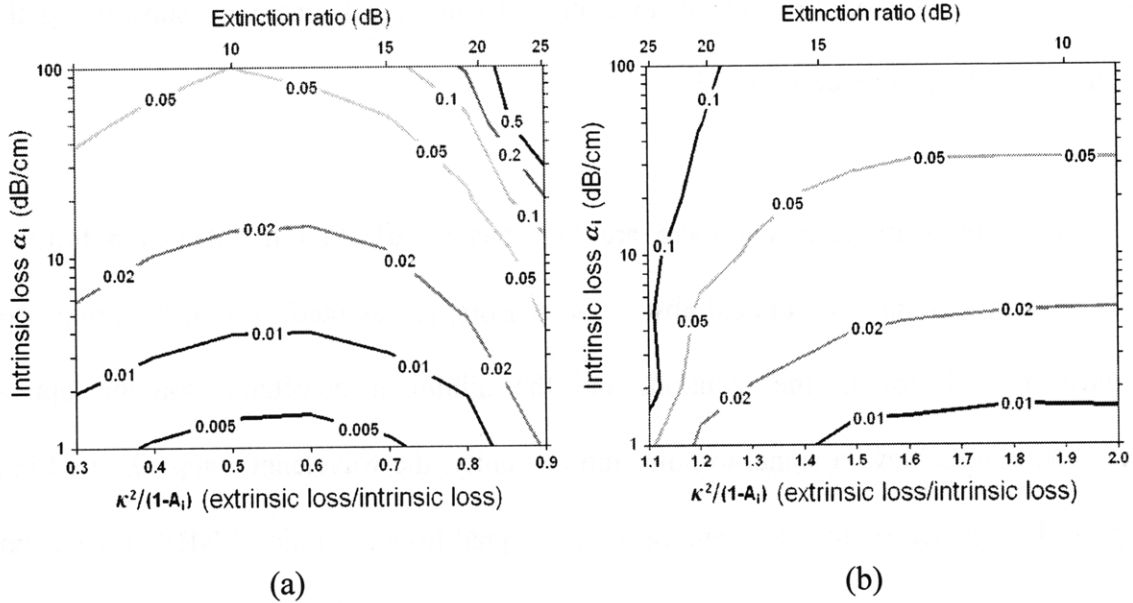


Figure 45 Detection limit $\Gamma \cdot \alpha$ of optical resonator sensors simulated using a Monte-Carlo approach. The vertical axis represents the intrinsic linear optical loss inside the resonator, the horizontal axis is the ratio between round-trip extrinsic loss (coupling loss) k^2 and intrinsic loss $1-A_i$, and the detection limit values of $\Gamma \cdot \alpha$ can be read out from the iso-resolution curves (unit: cm^{-1}). When $k^2/(1-A_i) < 1$: (a) the resonator is under coupled, and when $k^2/(1-A_i) > 1$: (b) the resonator is over coupled. The simulation assumes an SNR of 20 dB for transmission measurements at each discrete wavelength and a spectral scan step of 1 pm.

The detection limit $\Gamma \cdot \alpha$ of absorption sensors is also inversely proportional to the transmission measurement SNR. This result suggests that improved sensor detection limit can be achieved through suppressing noise in the resonator transmission spectrum measurement, for example, by using light source with superior power stability and read-out electronics with reduced circuit noise.

Figure 45 plots the simulated detection limit of $\Gamma \cdot \alpha$ as functions of the intrinsic resonator loss and the ratio between extrinsic and intrinsic loss in two different regimes, under-coupling (a) and over-coupling (b). In the Monte-Carlo simulations we assume an SNR of 20 dB for transmission measurements at each discrete wavelength and a spectral scan step of 1 pm. The detection limit of sensors with different measurement instrumentation parameters can thus be calculated according to the proportionality relations described above. As we can see from the plots, resonators with low intrinsic loss and a medium extrinsic loss to intrinsic loss ratio (corresponding to an extinction ratio of ~ 12 dB) gives the lowest detection limit and hence an optimal sensor design. This optimal extinction ratio value arises from the trade-off between maximizing the S factor and improving the extinction ratio change resolution ΔT_{\min} : although resonant peaks with a high extinction ratio show more sensitive response to changes in optical absorption (i.e. larger ΔT for the same optical absorption in the solution α_e), even small deviations in Lorentzian peak fit translate to a significant error of extinction ratio estimation. In addition, Figure 45 suggests that under-coupled resonator sensors exhibit improved detection limit compared to over-coupled resonators with the same intrinsic loss figures, which possibly can be attributed to the lower extrinsic loss and hence higher loaded cavity Q-factors of under-coupled resonators.

To summarize, slightly under-coupled (extinction ratio ~ 12 dB), low loss resonant cavities lead to superior detection limit of optical absorption in the solution.

8.2.2. Experiment

The optofluidic resonator device fabrication process is described in detail in Chapter 4. A top view micrograph of the fabricated microfluidic channel overlaid with a linear array of Ge-Sb-S microdisks is shown in Figure 46(a). We test different microdisks with radii of 20 μm , 30 μm and 50 μm for cavity-enhanced spectroscopy; the similar spectroscopic results obtained from the tests suggest excellent fabrication uniformity and reproducibility, as well as the general applicability of the spectroscopic device operation principle.

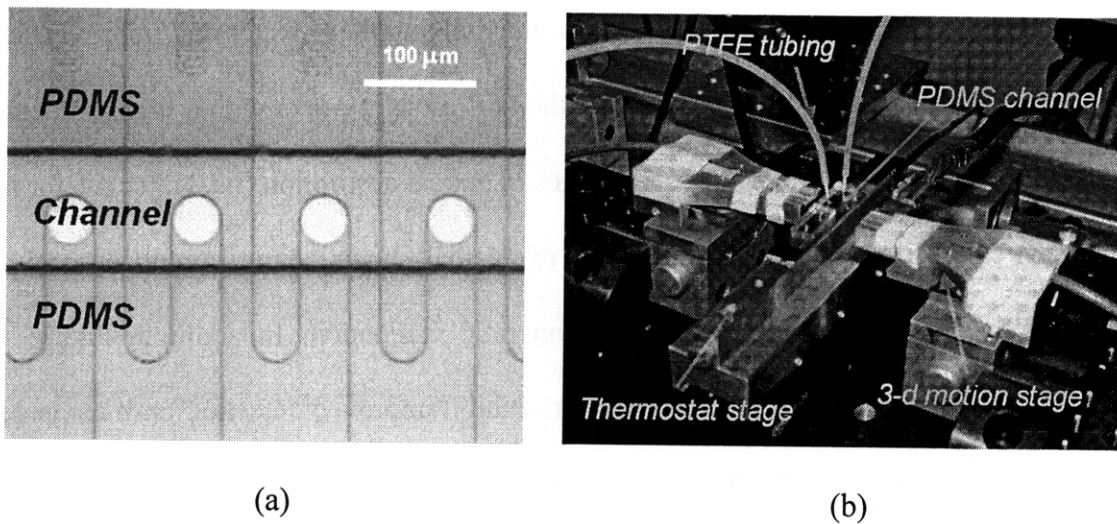


Figure 46 (a) Top view micrograph of a PDMS microfluidic channel overlaid with a linear array of 20 μm radius Ge-Sb-S microdisks; (b) photograph of an optofluidic chip under testing.

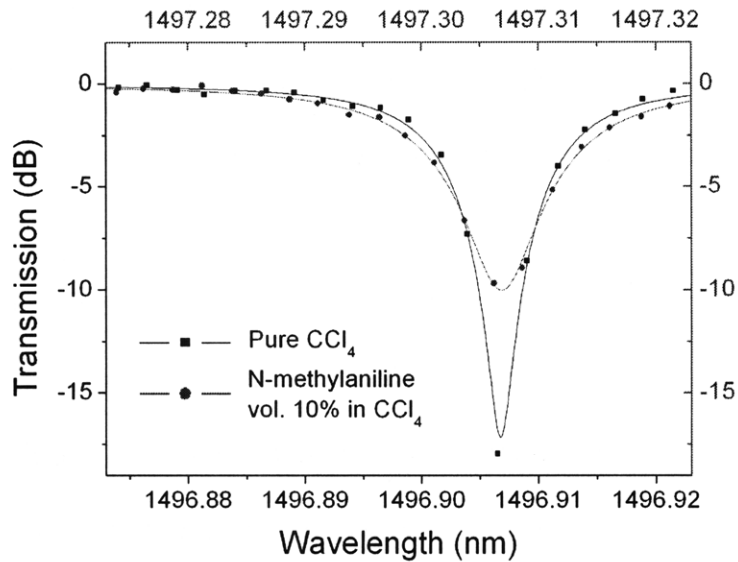


Figure 47 Microdisk transmission spectra around a resonant peak before and after N-methylaniline solution injection: the dots are experimentally measured data points and the lines are theoretical fitting results based on the generalized coupling matrix formalism; the extinction ratio change and resonant peak broadening are due to the optical absorption of N-methylaniline near 1500 nm.

We use the optofluidic resonator device to measure the well-defined absorption peak of N-methylaniline near 1500 nm. The laser wavelength scanning step used in our tests is ~ 2.6 pm. Multiple scan averaging is employed to reduce noise and improve measurement resolution. Figure 46(b) is a photograph of the optofluidic resonator device under testing. Prior to device testing using N-methylaniline solutions, transmission spectra of the resonators are measured when the microfluidic channels are filled with pure carbon tetrachloride. The “baseline” spectra are then used to derive intrinsic device parameters (α_i and k) of the resonators. Quality factors (Q) of the resonators under testing is within the range of 130,000 ($\pm 15\%$) in pure CCl_4 , which corresponds to a linear waveguide loss of ~ 1.5 dB/cm. Note that this Q -factor figure is slightly higher compared to the values in Table 6, possibly due to improved fabrication control. During the cavity-enhanced

spectroscopic test, N-methylaniline solutions in carbon tetrachloride of varying concentrations are injected into the channels using a syringe pump and the optical transmission spectra of the resonators are monitored *in situ*.

Figure 47 shows the transmission spectra around a resonant peak, both before and after injection of 10% vol. N-methylaniline solution in CCl_4 into the microfluidic channel. The resonator works in an under-coupling regime; therefore the additional optical loss due to N-methylaniline absorption results in a decrease of the extinction ratio along with a broadening of the resonant peak.

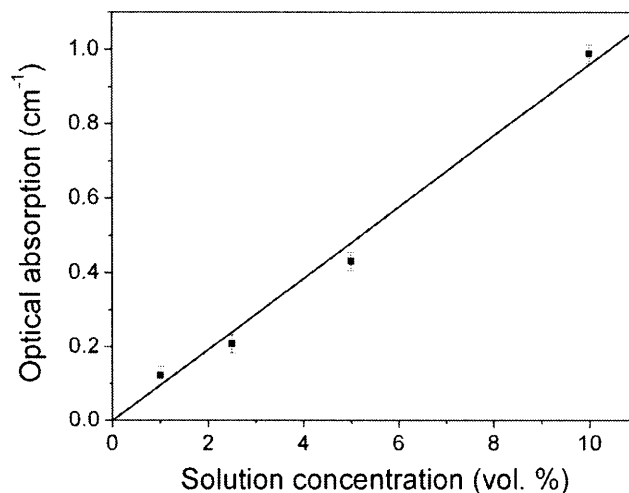


Figure 48 Measured optical absorption of N-methylaniline solutions in carbon tetrachloride as a function of N-methylaniline concentration near the wavelength of 1500 nm.

Using the formula we present in the previous section, the optical absorption of N-methylaniline solution can be extracted based on the resonant peak extinction ratio change. Figure 48 plots the optical absorption of N-methylaniline solutions with different

concentrations, measured using the optofluidic resonator. The lowest concentration we test in our experiment is 1%, which corresponds to $\sim 0.1 \text{ cm}^{-1}$ absorption coefficient. To evaluate the absorption detection limit of the device, we performed multiple measurements and the standard deviation of the resulting data is taken as the noise floor of our experimental setup. If we define the detection limit as the solution optical absorption that generates a signal-to-noise ratio of unity, the detection limit of a resonator with 17.2 dB extinction ratio (Figure 47) is approximately 0.02 cm^{-1} based on experimentally determined noise floor. This is attained with 64 wavelength-sweeping scan averaging across the resonant peak and an effective 64-scan total integration time of 0.6 s. The 0.02 cm^{-1} detection limit is in good agreement with the theoretically simulated value of 0.016 cm^{-1} , using the Monte-Carlo method. The present study result features a three-fold improvement compared to our previous result attained with the straight waveguide sensor with centimeter-long optical path length we show in section 8.1. ($\sim 0.07 \text{ cm}^{-1}$), while the physical device length is decreased by 40-fold. Such comparison clearly demonstrates the competitive advantage of using optical resonators for “sensor-on-a-chip” type infrared absorption spectroscopy.

8.3. Summary

In this chapter, we have experimentally demonstrated two types of on-chip sensor devices for measuring infrared absorption. The devices are tested for N-methylaniline sensing. The evanescent waveguide sensor yields transmission spectra in good agreement with traditional UV-Vis spectroscopy, and features an absorption detection limit down to 0.07 cm^{-1} . To resolve the physical limit between sensitivity and device footprint in evanescent

waveguide sensors, we demonstrate cavity-enhanced infrared absorption spectroscopy using optofluidic micro-resonators in Ge-Sb-S chalcogenide glass. We show that slightly under-coupled (extinction ratio ~ 12 dB), low loss resonant cavities lead to optimized detection limit of optical absorption in the solution. We achieve a detection limit of $\sim 0.02 \text{ cm}^{-1}$ to optical absorption in N-methylaniline solutions, using micro-disk resonators with a cavity Q-factor of $\sim 130,000$. This detection limit represents a three-fold improvement as compared to the evanescent waveguide sensor, while the physical device length is reduced by 40-fold. This result clearly proves the competitive advantage of using optical resonators for on-chip infrared absorption spectroscopic sensing.

Chapter 9. Resonant cavity refractometry for precision glass metrology

An important feature of resonators is their extreme sensitivity to refractive index and optical absorption change. Besides its application in biochemical sensing, this property can also be utilized to probe micro-structural evolution in chalcogenide glasses, since structural modifications in these glasses are often accompanied by an optical property change¹¹¹. In addition, accurate determination of optical property change (e.g. refractive index modification) is also technically important for applications that are sensitive to small index variations, and the examples include direct laser writing and sub- T_g structural relaxation (aging). Therefore, in this chapter, we highlight the application of glass resonators as highly sensitive metrology tools capable of extracting kinetic structural evolution information otherwise difficult or even impossible to obtain using conventional techniques. We believe that this *resonant cavity refractometry* technique holds huge promise for high precision glass metrology, accurate process control, and fundamental glass science investigation.

9.1. Photosensitivity kinetics of chalcogenide glass to near-band gap illumination

Chalcogenide glasses are well-known for their photosensitivity to near-band gap illumination, which leads to an index modification typically in the order of ~ 0.01 . In the first application example of resonant cavity refractometry, the resonators are applied to derive photosensitive response of As_2S_3 to $\lambda \sim 550$ nm light. To study the photosensitivity of As_2S_3 , an As_2S_3 racetrack resonator device is exposed to timed near-bandgap light (~ 550 nm wavelength with an irradiance of 6.2 mW/cm^2 from a band pass filtered halogen lamp) to induce a controlled refractive index change using a setup schematically

shown in Figure 49(a), and the resulting peak shift was monitored in-situ. A Lorentzian fit has been used to extract the accurate peak position. Refractive index change in the As₂S₃ core can be calculated using a formula derived from Eq. 96:

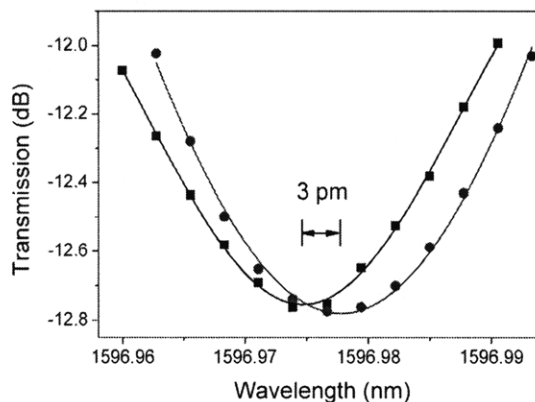
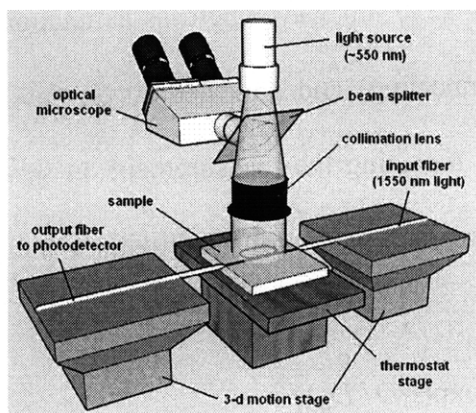
$$\text{Eq. 75: } \Delta n = \frac{\Delta\lambda}{\lambda} \times n_g / \Gamma_{core}$$

where $\Delta\lambda$ stands for the resonant peak shift, n_{eff} is the waveguide effective index, and Γ is the confinement factor in As₂S₃ core defined by¹¹⁰:

$$\text{Eq. 76: } \Gamma_{core} = \frac{n_{core} c \epsilon_0 \iint_A |\mathbf{E}|^2 dx dy}{\iint_{\infty} \text{Re}\{\mathbf{E} \times \mathbf{H}^*\} \cdot \hat{\mathbf{z}} dx dy}$$

Finite-difference simulations give n_{eff} and Γ of TM polarization to be 1.88 and 0.77, respectively. The group index n_g can be calculated from the resonator circumference and FSR to be 2.31.

Figure 49(b) gives an example of two spectra with a peak shift of (3 ± 0.3) pm after light exposure, corresponding to an index increase of $4.5 \times 10^{-6} \pm 10\%$ in As₂S₃ at 1597 nm wavelength. The wavelength resolution of 0.3 pm was statistically determined by repeating the experiment and comparing multiple measurement results. Such a high sensitivity is essential especially for accurate photosensitivity measurement in annealed glass, which exhibits much smaller photo-induced index change compared to its as-deposited counterpart.



(a)

(b)

Figure 49 (a) Photosensitivity measurement setup; (b) Transmission spectra of a resonator in the proximity of its resonant peak. Black dots represent experimental data points, and the red dots are data measured in the same device after exposure to ~ 550 nm wavelength light; the curves are fitted Lorentzian peaks. A wavelength shift of (3 ± 0.3) pm is determined by peak fit, corresponding to an index change of $(4.5 \times 10^{-6} \pm 10\%)$ RIU in As_2S_3 at 1597 nm wavelength.

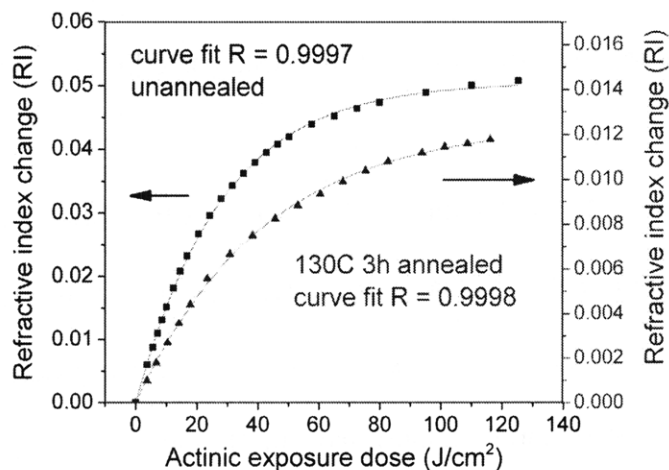


Figure 50 Photo-induced refractive index change as a function of exposure dose ($\lambda \sim 550$ nm) in an as-deposited, unannealed resonator and in a resonator annealed at 130°C for 3 hours

Figure 50 shows the refractive index increase at 1550 nm wavelength as a function of exposure dose for both as-deposited (without annealing) and annealed As₂S₃ devices. Excellent data reproducibility was confirmed by repeating the measurement on several resonators. In both cases the index increase can be well described with a single-exponential function:

$$\text{Eq. 77: } \Delta n = \Delta n_{\text{sat}} \times [1 - \exp(-D / D_0)]$$

where Δn_{sat} is the maximum index change when the photorefractive effect has been fully saturated, D represents the exposure dose in J/cm² and D_0 is a material constant which depends on processing history. Our results confirm the validity of exponential empirical fit in previous reports^{112, 113}. For unannealed As₂S₃, $\Delta n_{\text{sat}} = 0.0505 \pm 0.0002$, $D_0 = (0.036 \pm 0.001) \text{ J/cm}^2$, whereas for annealed As₂S₃, $\Delta n_{\text{sat}} = 0.0125 \pm 0.0001$, $D_0 = (0.024 \pm 0.001) \text{ J/cm}^2$. The smaller photo-induced index change in annealed glass has also been observed by C. Lopez et al. in As₂S₃ films prepared by the same deposition technique, irradiated with an 800 nm femtosecond laser and measured using an ellipsometer⁶².

It is also important to note that the annealed and unannealed samples have distinctive D_0 values. This observation suggests that even though both annealing and photosensitivity lead to a refractive index increase in As₂S₃ glass¹¹⁴, these two processes actually result from distinctive micro-structural changes and thus follow very different kinetic paths. Therefore, even though photosensitivity in chalcogenide glasses is a process accompanied by entropy increase¹¹⁵, it is dissimilar from thermal annealing from a glass micro-structure point of view. This conclusion also confirms the previous findings by other authors^{43, 116, 117}.

9.2. Measuring nonlinear absorption in chalcogenide glass using cavity enhanced absorption spectroscopy

Besides their extreme sensitivity to refractive index change, high-Q optical resonators can also serve as sensitive sensors to optical absorption variations, as we have shown in Chapter 8. In this section, we aim at leveraging this property to develop a technique for accurate measurement of nonlinear optical absorption in chalcogenide glasses.

The resonator device used in this study is an As_2S_3 micro-disk resonator with SU8 over cladding. Details of the glass bulk preparation and device fabrication are described in Chapter 4. Prior to measurement, the resonators are aged at room temperature until the resonant wavelength is stabilized. Table 9 lists the linear optical parameters of the micro-disk resonators near 1550 nm wavelength, specifically measured at low input power levels to avoid nonlinear effects. Notably the resonators exhibit a negative thermo-optic (TO) coefficient as a result of the SU8 polymer over cladding, from which we infer an As_2S_3 material TO coefficient of $\sim 4 \times 10^{-5} \text{ K}^{-1}$, in good agreement with a previous report¹¹⁸. The Q-factor for the resonator used in this study is lower compared to the ones reported in Chapter 5 mainly due to fabrication variations.

Table 9 Linear optical parameters of the As_2S_3 micro-disk resonators used in this study

| Cavity Q-factor | FSR | Optical power enhancement | Equivalent loss | Thermo-optic coefficient |
|-------------------|---------|-----------------------------|-----------------|------------------------------------|
| $60,000 \pm 10\%$ | 626 GHz | $(15.2 \pm 0.5) \text{ dB}$ | 2.4 dB/cm | $-5 \times 10^{-6} \text{ K}^{-1}$ |

In the first set of nonlinear optical measurements, TM polarization light from a tunable laser is first amplified using an erbium-doped fiber amplifier (EDFA) and then end coupled into a bus waveguide through a silica optical fiber. The output light from the bus waveguide is fiber coupled and its power recorded using an optical spectrum analyzer (OSA). The unoptimized coupling loss per facet is estimated to be (4.5 ± 1) dB. Figure 51 plots the transmission spectra of the micro-disks measured at different input power levels; the arrows connecting the resonant peaks indicate the temporal sequence of the measurements, i.e. the measurement starts with a low input power (linear regime), and then the coupled power into the bus waveguide is increased up to 18.6 dBm and finally decreased back to the linear regime.

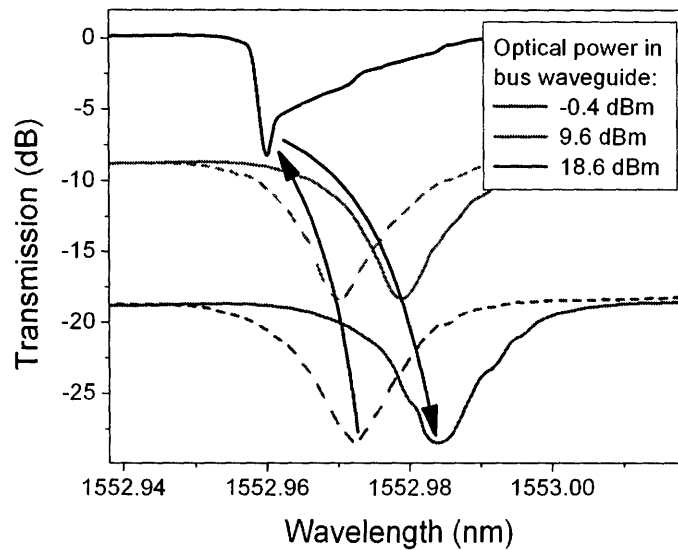


Figure 51 Transmission spectra of an As_2S_3 micro-disk resonator near a resonant peak measured at different power levels coupled into its bus waveguide; the arrows indicate the temporal sequence of measurements. The resonant peak red shift after high power measurement manifests the cavity enhanced photosensitivity effect, and the peak shape distortion at high optical power is a consequence of thermo-optic cavity instability.

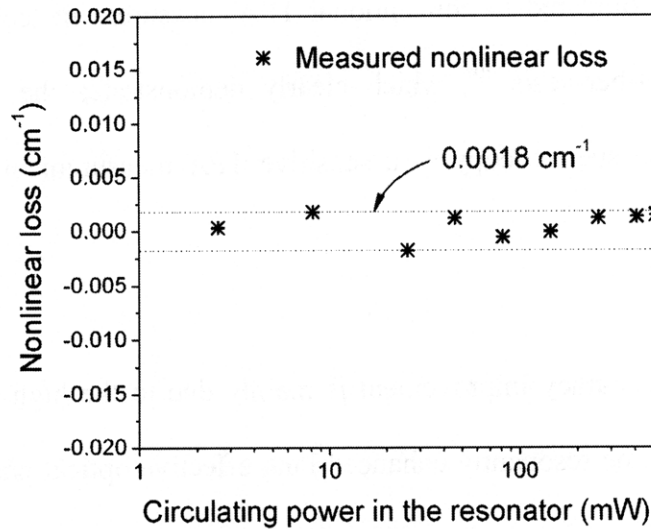


Figure 52 Nonlinear absorption calculated from the measured micro-disk transmission spectra as a function of circulating power inside the resonator: the calculation uses a coupling matrix approach¹⁷; the two red dotted lines indicate the measurement accuracy.

We notice that optical resonance extinction ratio critically depends on optical loss and hence any absorption variation, a phenomenon we can leverage to accurately measurement nonlinear absorption in As_2S_3 micro-disks. Details regarding the data processing methodology in cavity enhanced absorption spectroscopy can be found in Chapter 8. Figure 52 gives the measured nonlinear absorption component (on top of existing linear absorption) as a function of circulating power inside the resonator. In the presence of TPA, nonlinear absorption is supposed to be linearly proportional to the circulating power; the lack of such apparent linearity in Figure 52 suggests the absence of TPA in As_2S_3 glass within the measurement accuracy of our cavity-enhanced absorption spectroscopy technique. Based on the micro-disk transmission spectra, the cavity-enhanced absorption spectroscopy technique gives an upper limit of TPA coefficient in

As₂S₃ film to be 1.5×10^{-13} m/W. Notably this measurement accuracy represent a 5 to 10-fold improvement compared to conventional TPA measurement techniques such as Z-scan¹¹⁹ or optical fiber tests¹²⁰, which clearly demonstrates the potential of cavity enhanced absorption spectroscopy as a sensitive TPA measurement technique for thin film materials.

This measurement accuracy improvement is mainly due to the high power density in a resonator as well as the resonantly enhanced long effective optical path length. The high power density in the resonator is attributed to: 1) the resonance enhancement effect, which leads to 15.2 dB, i.e. approximately 33-fold power enhancement; and 2) the small optical mode size ($< 10^{-12}$ m², smaller than the diffraction limit achievable via free space optics at 1550 nm wavelength) in a high-index-contrast micro-disk.

9.3. Thermo-optic cavity instability

From Figure 51 it is clear that the resonant peak is distorted towards a shark fin-like shape at high input power suggesting a cavity instability phenomenon. Our calculations indicate that the optical power inside the resonator is still an order of magnitude smaller than that required to trigger Kerr instability. Moreover, the resonant peak is slanted towards shorter wavelength, which cannot be explained by the cavity enhanced photosensitivity effect we will discuss in section 9.4. Therefore, we attribute the peak shape distortion to thermo-optic cavity instability, which results from heat deposited on the micro-disk during a high-power measurement and the subsequent resonant wavelength change. We note that similar cavity instability phenomena have been reported

in As_2Se_3 micro-spheres recently¹²¹, and here we emphasize two important distinctions in our experiment: firstly, the resonant peak is slanted towards the shorter wavelength end in our measurement due to the negative TO coefficient of our device; secondly, the power threshold for triggering such instability is two orders of magnitude higher in our case, most possibly due to the improved heat conduction from the on-chip micro-disk device to silicon substrate (heat sink), as compared to the case of a suspended micro-sphere. Using the measured device TO coefficient from Table 9, the temperature increase of micro-disk is calculated to be < 7 °C even at 18.6 dBm input power, and thus no thermal-induced material degradation is expected in our tests. For nonlinear optical applications, such an increased cavity instability threshold is critical as it allows higher power to be coupled into the resonator for enhanced nonlinear functionalities. In addition, the partial TO coefficient compensation between chalcogenide glass (with a positive TO coefficient) and polymer over cladding (with a negative TO coefficient) in our device suggests possible further increase of the instability threshold by employing an athermal design.

9.4. Resonant cavity enhanced photosensitivity in As_2S_3 chalcogenide glass at 1550 nm telecommunication wavelength

In addition to the transient TO response, the resonant wavelength red shifts after the high power test, as is shown in Figure 51. Such a permanent peak shift indicates a non-transient refractive index change in As_2S_3 . To verify the origin of such index modification, a series of pump-probe measurements are performed using a setup schematically illustrated in Figure 53. In the test, light from a pump laser amplified by an EDFA is used to induce refractive index change in the As_2S_3 micro-disk, and the

corresponding resonant peak shift is measured independently using a probe laser (with the pump laser turned off during measurement). Figure 54 shows the transmission spectra evolution in a pump-probe setting when the pump light is on/off micro-disk resonance. Apparently, a resonant peak red shift is observed when the pump light is tuned to the micro-disk resonant wavelength; in contrast, when the pump light is off-resonance, no resonant peak shift is observed even at the highest pump power. This result suggests that the glass refractive index change induced by resonant pumping stems from light coupled into the micro-disk at resonance and hence resonantly enhanced photon-matter interaction. From Figure 54, we can also estimate the threshold power density for such cavity enhanced photosensitivity to be $< 0.1 \text{ GW/cm}^2$, based on the onset of resonant peak shift at a resonant pumping power of 9.6 dBm. This threshold figure is an order of magnitude smaller compared to the previously reported value⁴⁸, probably because the resonant cavity refractometry method we use enables the sensitive detection of much smaller refractive index variation. In our experiment we measure refractive index change as large as 1.6×10^{-2} due to cavity enhanced photosensitivity and no obvious saturation behavior has been observed yet. Since the saturation behavior of such photosensitivity critically determines the upper limit of optical power density allowed in nonlinear optical applications without disrupting device performance (i.e. causing “optical damage”), further study is still under way to investigate this phenomenon in greater detail.

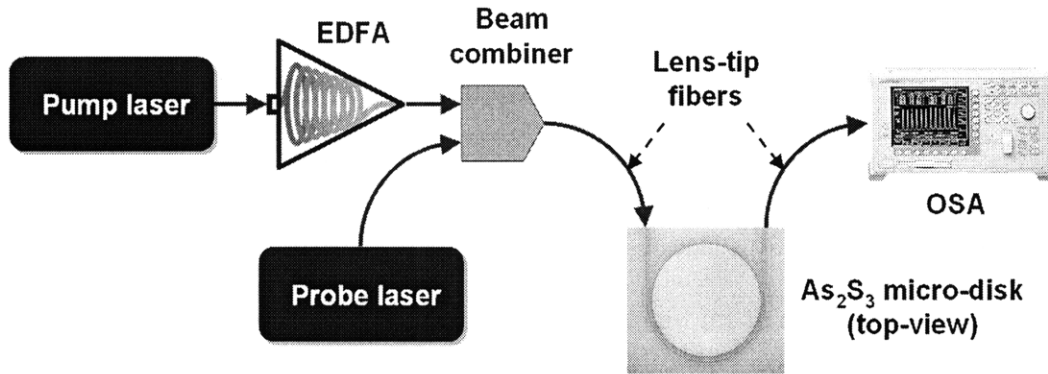


Figure 53 Schematic illustration of the pump-probe measurement setup used to characterize cavity-enhanced photosensitivity in As_2S_3 glass: both the pump and probe are tunable lasers operating near 1550 nm wavelength.

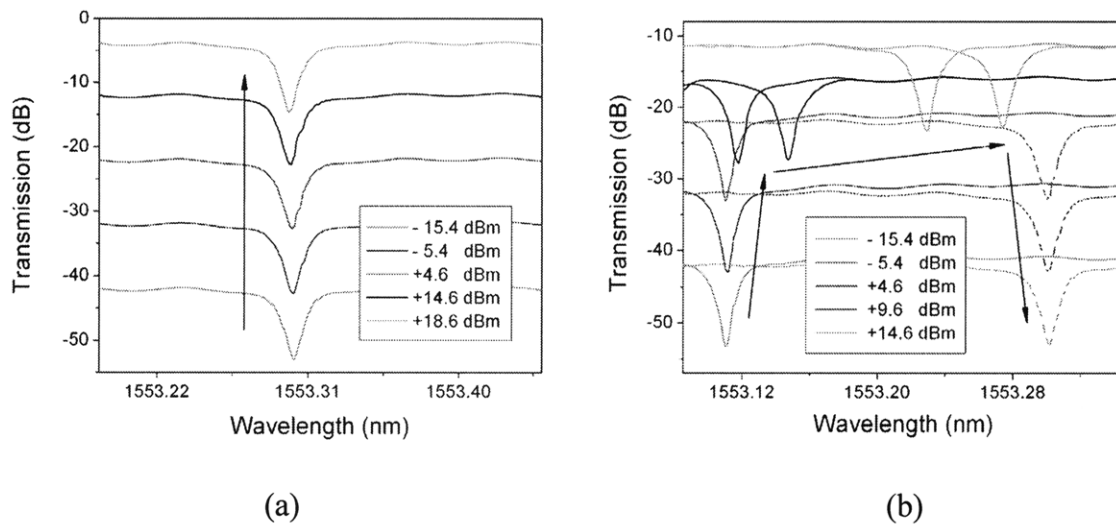


Figure 54 Transmission spectra of As_2S_3 micro-disks measured using a low-power probe beam in a pump-probe setting: (a) when the pump light is off-resonance, no resonant peak shift is observed even at the highest pump power; (b) when the pump light is aligned with micro-disk resonant wavelength, resonant cavity enhanced photosensitivity leads to the non-transient red shift of resonant peak; note that the spectra with different pump power are offset vertically for clarity.

From a material perspective, we also seek to understand the origin of such photosensitivity. Since the heating effect during our optical tests is minimal ($< 7^\circ\text{C}$), we

can exclude heating-induced material structural relaxation (“annealing”). In addition, since the photon energy at 1550 nm wavelength is much smaller than the optical band gap of As_2S_3 , other mechanisms that possibly account for the photosensitivity necessarily involve energy transfer to glass network via sub-gap absorption, including defect (e.g. Urbach band tails states or mid-gap states) absorption and nonlinear absorption with the latter mainly refers to two photon absorption (TPA). Further, since the upper limit of nonlinear absorption determined from our measurement (< 0.008 dB/cm) is two orders of magnitude smaller compared to linear absorption, we conclude that sub-gap defect absorption is responsible for the energy transfer from 1550 nm wavelength photons to the glass network in the photosensitive process. Since defect density and energy distribution in glasses is highly processing-dependent, we do expect purposive control of the photosensitivity threshold in chalcogenide glass via optimizing film deposition and treatment processes.

9.5. Aging of As_2S_3 chalcogenide glass

Another application example of resonant cavity refractometry is the quantitative determination of glass aging kinetics. It has been well documented that chalcogenide glasses, especially the compositions with relatively low glass transition temperature (T_g), undergo considerable sub- T_g structural relaxation (aging) at room temperature, given that glasses are actually situated in a thermodynamically unstable state compared to their single crystalline counterparts. The aging process is accompanied by a refractive index change; therefore refractive index becomes the observable of choice for monitoring structural relaxation kinetics in glasses. In addition to the fundamental importance of

understanding structural relaxation process in glasses, determination of refractive index change due to aging is essential to the stable operation of photonic device made from chalcogenide glasses.

In light of the importance of aging, this phenomenon has been extensively studied using structural¹²², mechanical^{123, 124}, and optical^{125, 126} techniques. However, since the structural relaxation rate at room temperature is relatively small, it often takes a long time in the order of several years to study the aging phenomenon at room temperature since most currently available techniques are not capable of detecting small structural or property changes. Further, the small magnitude of structural or property change due to aging also prohibits detailed studies on the structural relaxation kinetics.

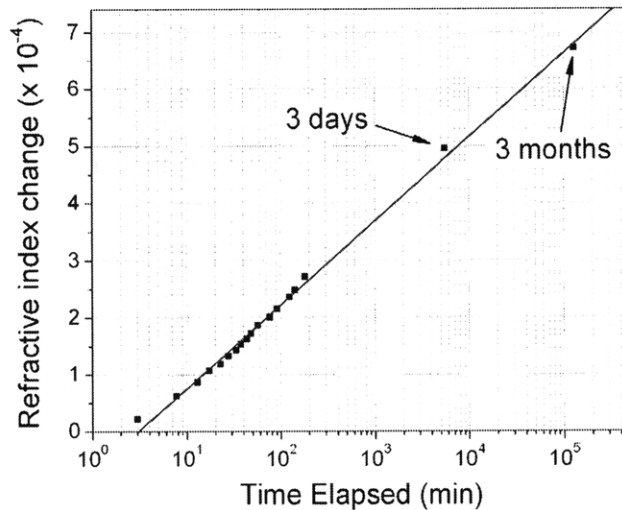


Figure 55 Refractive index change in As_2S_3 film as a function of time elapsed after annealing at 60 °C

The ultra-high sensitivity of resonant cavity refractometry provides a new route for quantitatively evaluating aging in chalcogenide glasses. Towards this end, a proof-of-

concept study is performed using an As_2S_3 micro-disk resonator. The resonator is annealed at 60 °C until the resonant peak is stabilized prior to the aging study. The resonant wavelength change is recorded as a function of elapsed time after annealing, and the corresponding refractive index change is calculated and shown in Figure 55. The refractive index change can be fitted using a semi-exponential model:

$$\text{Eq. 78: } \Delta n = [-0.72 + 1.47 \cdot \log t(\text{min})] \times 10^{-4}$$

This is what we believe to be the first quantitative study on the aging kinetics in chalcogenide glasses. Further study regarding temperature effects on aging is currently underway.

9.6. Summary

This chapter summarizes the work to date on using our recently developed resonant cavity refractometry technique to investigate micro-structural and property evolution in chalcogenide glasses. In resonant cavity refractometry, an optical resonant cavity is leveraged as a highly sensitive spectroscopic tool to detect refractive index and/or optical absorption change in the glass material comprising of the cavity, and thereby provide information on glass micro-structural evolution kinetics otherwise difficult to obtain using conventional metrology techniques.

We capitalize on the extreme sensitivity of optical resonance to refractive index variation to enable the sensitive detection of photo-induced index change caused by near-band gap illumination. We confirm that annealing and photosensitivity follow very different kinetic paths, suggesting that they result from dissimilar micro-structural changes.

The strong resonance enhancement effect is also utilized to measure nonlinear absorption inside chalcogenide glass using a novel cavity enhanced absorption spectroscopy technique, which clearly demonstrates the potential of cavity enhanced absorption spectroscopy as a sensitive TPA measurement technique for thin film materials.

The discovery on the cavity enhanced photosensitivity of As_2S_3 glass at 1550 nm telecommunication wavelength is significant given the increasing interest in using chalcogenide glasses as a Kerr medium for ultra-fast optical switching, since high optical power density is often involved in the nonlinear optical processes. The measured photosensitivity threshold is $< 0.1 \text{ GW/cm}^2$, and photo-induced refractive index change as large as 0.016 is observed. The photosensitive process is athermal; further, we confirm the absence of two photon absorption in As_2S_3 . These results lead us to conclude that defect absorption accounts for the energy transfer from photons to glass network.

Chapter 10. Investigation of copper alloying effects in As-Se-Te glass

In this chapter, I summarize our work on copper doped As-Se-Te glasses. The As-Se-Te glass presents a good model system for studying transition metal alloying effects in chalcogenide glasses; and copper has been well known to induce significant electrical property modification when added into chalcogenide glass network³¹, an important phenomenon for both fundamental glass science and practical applications. In this study, we aim at clarifying the impact of copper alloying on the structural, optical and electrical properties of As-Se-Te glass, and provide insight into the fundamental physics that accounts for these modifications.

In this study we evaluate two film deposition techniques for the preparation of films from As-Se-Te glasses containing high concentrations of Cu: thermal evaporation (single-source evaporation) and co-evaporation. The first technique for the film deposition is the thermal evaporation technique from bulk Cu doped chalcogenide glasses where the bulk material is used as the target. A systematic study of the structural modification of the chalcogenide bulk glasses in the ternary system As-Se-Te with the progressive introduction of Cu across a broad glass-forming range is presented. We establish a correlation between the glass structure and the optical properties of the glasses as determined from chemical and physical property measurements. Raman scattering has been used to examine the glass structure modification as a function of Cu concentration in the arsenic based glass system, using, both, single-source and dual-source co-evaporated films. The composition of the films has been verified using Wavelength Dispersive Spectroscopy (WDS) and the structure of the different films has been

measured using micro-Raman spectroscopy. The electrical properties of the Cu doped bulk and films have been investigated. A study of the electrical conductivity as a function of temperature has been used as a powerful tool to probe the electronic transport mechanism in the glasses.

10.1. Film deposition

Chalcogenide glass thin films were deposited on both oxide coated Si wafers (4" Si wafers with 1 μ m thermal oxide, Silicon Quest International) as well as pre-cleaned glass microscope slides (VWR International), by thermal evaporation. Films on the two different substrates were found to have very similar material properties due to the amorphous nature of both substrates at the substrate-film interface. Two different evaporation techniques, single-source evaporation from Cu-doped bulk glasses and dual-source co-evaporation of As₂Se₃ or As₂Te₃ (Alfa Aesar Inc, 99.99%) and CuSe (Alfa Aesar Inc., 99.99%) were tested. Details of the bulk glass fabrication process is described in Chapter 4. The evaporations were carried out with a base pressure <10⁻⁶ Torr. During evaporation, the current and voltage on the molybdenum boats are monitored to bring the chalcogenides just above melting point in order to establish a vapor pressure in the chamber and keep a constant evaporation rate. In dual-source co-evaporation, ratios of co-evaporated components are achieved by controlling the current passing through the individual boats. In the co-evaporation scheme, depositions were carried out only when the evaporation reached a steady state, namely a constant deposition rate is maintained at a fixed current value in order to equilibrate the evaporation sources.

10.2. Single source thermal evaporation of Cu doped films in the system $As_{0.40}Se_{0.35}Te_{0.25}$

Cu-doped films were obtained by single-source thermal deposition technique using Cu doped glasses in the composition $(1-x) As_{0.40}Se_{0.35}Te_{0.25} + x Cu$ with $x = 0.075, 0.10, 0.125$ and 0.15 used as a source.

10.2.1. Source characterization

Table 10 Variation in glass transition temperature, density and conductivity of the investigated bulk samples used in the single-source film evaporation, as a function of atomic fraction of Cu in the glass host system $(1-x) As_{0.40}Se_{0.35}Te_{0.25} + x Cu$.

| Atomic fraction Cu x | T_g (°C) ± 5°C | Density (g/cm ³) ± 0.02 | Conductivity (1/(Ω.m)) at 298K |
|----------------------------|---------------------|---|--------------------------------------|
| 0 | | 4.99 | |
| 0.05 | | 5.18 | |
| 0.075 | 157 | 5.25 | 0.00056 |
| 0.1 | 162 | 5.30 | 0.00152 |
| 0.125 | 168 | 5.40 | 0.00518 |
| 0.15 | 174 | 5.35 | 0.01949 |

In Table 10 we report the glass transition temperatures and the density of the Cu doped $As_{0.40}Se_{0.35}Te_{0.25}$ glasses as a function of Cu content. The glass transition temperatures of the glasses with the composition $(1-x) As_{0.40}Se_{0.35}Te_{0.25} + x Cu$ with $x = 0.05, 0.075, 0.10,$

0.125 and 0.15 increase monotonically with increasing Cu incorporation and the corresponding density increases from 4.99 g/cm³ to 5.35 g/cm³. The absence of sharp diffraction peaks in the XRD spectra has confirmed the amorphous nature of the glasses, and lack of detectable crystallinity for the Cu doping levels used.

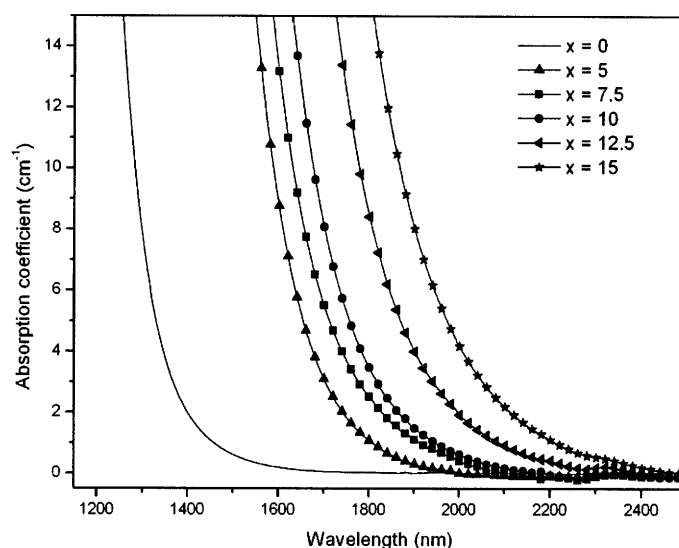


Figure 56 Absorption spectra of bulk $(1-x) \text{As}_{0.40}\text{Se}_{0.35}\text{Te}_{0.25} + x \text{Cu}$ glasses. When Cu is gradually added in the glass network, the optical band gap exhibits a shift to the near infrared.

The absorption spectra of the glasses are shown in the Figure 56. When Cu is gradually added in the glass network, the optical band gap exhibited a shift to the near infrared. The exponential absorption tail of the bulk glasses can be well fitted by an Urbach bandtail model, which confirms the existence of mid-gap states in these amorphous materials.

The micro-Raman spectra of the glass with $x = 0.15$, taken as an example, is presented in Figure 57. The spectra exhibit a broad band from 100cm⁻¹ to 300cm⁻¹. No variation of the

Raman signal was observed when the Cu content increases. This may suggest that Cu is introduced into the glass without disrupting the basic network units, i.e. As-chalcogen pyramids. The major Raman peak is centered near 195cm^{-1} for all samples. The main broad band cannot be simply attributed to AsSe_3 pyramids (typical vibration band located at 200cm^{-1} to 280cm^{-1}) or AsTe_3 units (typical vibration band located at 150cm^{-1} to 190cm^{-1}). In accordance with Nguyen et al., this band may be attributed to modified structural units which are represented by $\text{AsSe}_{(3-x)}\text{Te}_x$ structural units¹²⁷. The shoulders at smaller wavenumber may be attributed to greater Te concentrated $\text{AsSe}_{(3-x)}\text{Te}_x$ units, as Te is heavier than Se. The shoulder at 170cm^{-1} is consistent with the features that appear in pure As_2Te_3 glasses and is probably due to AsTe_3 units existing in the glasses whereas the shoulder at $\sim 240\text{cm}^{-1}$ may be related to AsSe_3 pyramidal units.

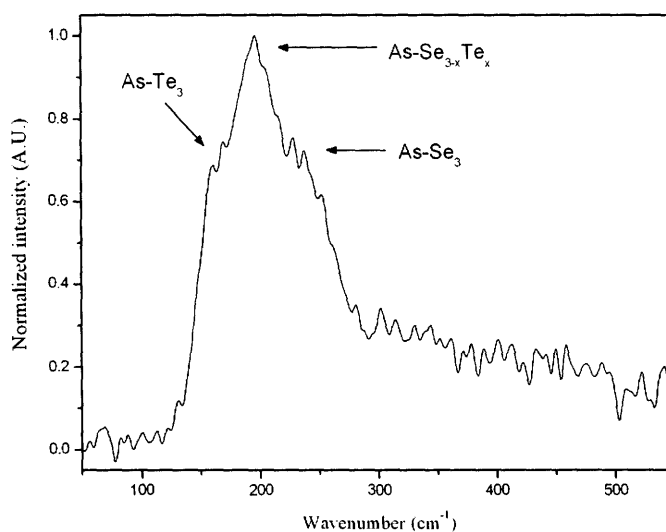
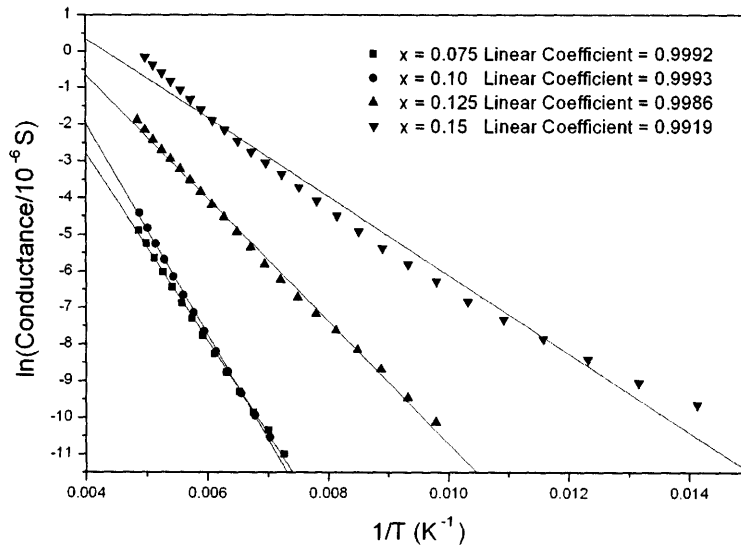


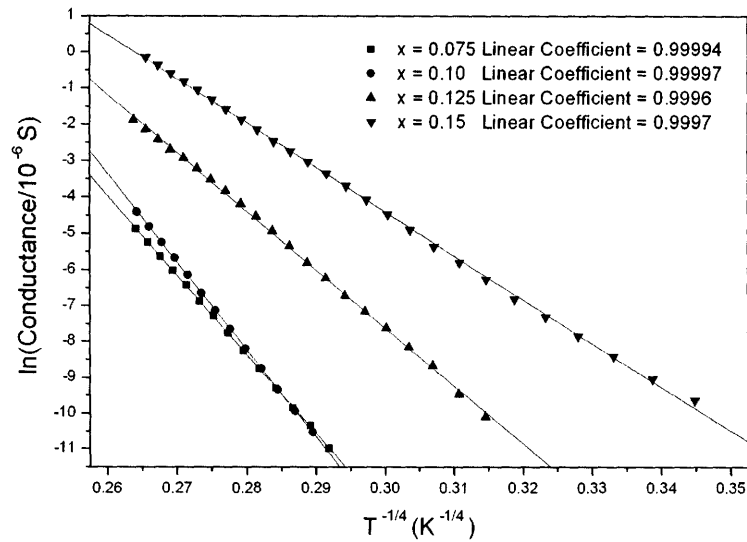
Figure 57 Micro-Raman spectra of bulk sample with $x = 0.15$ in $(1-x) \text{As}_{0.40}\text{Se}_{0.35}\text{Te}_{0.25} + x \text{Cu}$. The spectra exhibit a broad band from 100cm^{-1} to 300cm^{-1} . This band may be attributed to modified structural units which are represented by $\text{AsSe}_{(3-x)}\text{Te}_x$ structural units.

The conductance of the investigated glasses has been measured at temperatures ranging from room temperature down to 70K. Table 10 lists the conductivity of the glasses (measured at 298K) and clearly shows that the conductivity increases by a factor of 35 when the content of Cu increases from $x = 0.075$ to $x = 0.15$. The logarithm of the conductivity data are plotted against both $1/T$ and $T^{-1/4}$ and are presented in Figure 58. These results have been fitted considering two conduction mechanisms; extended states conduction which is equivalent to thermal excitation of localized carriers into the bands; and variable range hopping near the Fermi level. The fits are also shown in Figure 58. As one can see, below 200K, the conductance of all the samples can be very well fitted to the $T^{-1/4}$ law. This excellent fit indicates that carrier hopping near Fermi level is most probably the dominant charge transport mechanism at low temperature, which is consistent with the general trend that $T^{-1/4}$ law is obeyed at lower temperature.

Using Eq. 5 and Eq. 6, $N(E_F)$ values in As-Se-Te-Cu glasses are calculated and tabulated in Table 11. If we use the pre-exponential factor $\sigma_0 T^{1/2}$ fitted from $\ln(\sigma T^{1/2})-T^{-1/4}$ curve, the calculation gives an unphysically high value of $N(E_F)$ compared to the typical 10^{17} - 10^{19} cm^{-3} defect center density in chalcogenide glasses. As we mentioned in Chapter 2, this phenomenon was attributed to the over-simplified assumptions (e.g. constant density of states (DOS) near Fermi energy, omission of multi-phonon process, etc.) which Mott used in deriving his variable range hopping theory. A more reasonable estimation of $N(E_F)$ can be given by using Eq. 4 and $\alpha \sim (10\text{\AA})^{-1}$, which leads to a defect density of the order of 10^{16} - 10^{17} $\text{cm}^{-3}\text{eV}^{-1}$ (Table 11).



(a)



(b)

Figure 58 Conductance of the bulk $(1-x) \text{As}_{0.40}\text{Se}_{0.35}\text{Te}_{0.25} + x \%$ Cu glasses at temperatures ranging from 200K to 70K fitted to two different conduction models (a) $\ln(\text{Conductance})-1/T$, extended states conduction or thermal excitation of localized states; (b) $\ln(\text{Conductance})-T^{-1/4}$, variable range hopping according to Mott-Davis model. The error of the measurement is estimated to be smaller than 1 pS.

Table 11 Mott's parameters α and $N(E_F)$ calculated for bulk $(1-x) \text{As}_{0.40}\text{Se}_{0.35}\text{Te}_{0.25} + x \text{Cu}$ glasses using a typical phonon frequency of 10^{12}Hz . $*N(E_F)$ are density of states near Fermi energy calculated by assuming $\alpha = (10\text{\AA})^{-1}$.

| x | $\sigma_0 T^{1/2}$ ($\Omega^{-1}\text{cm}^{-1}\text{K}^{1/2}$) | T_0 (K) | α (cm^{-1}) | $N(E_F)$ ($\text{cm}^{-3}\text{eV}^{-1}$) | $*N(E_F)$ ($\text{cm}^{-3}\text{eV}^{-1}$) |
|--|---|--------------------|----------------------------------|--|---|
| 0.075 $\text{As}_{0.37}\text{Se}_{0.33}\text{Te}_{0.23}\text{Cu}_{0.075}$ | 9.95×10^{19} | 2.63×10^9 | 1.08×10^{27} | 1.01×10^{77} | 7.04×10^{16} |
| 0.1 $\text{As}_{0.36}\text{Se}_{0.32}\text{Te}_{0.23}\text{Cu}_{0.10}$ | 8.14×10^{22} | 3.91×10^9 | 1.07918E30 | 6.72×10^{85} | 4.75×10^{16} |
| 0.125 $\text{As}_{0.35}\text{Se}_{0.31}\text{Te}_{0.21}\text{Cu}_{0.125}$ | 4.00×10^{14} | 7.97×10^8 | 2.40×10^{21} | 3.60×10^{60} | 2.33×10^{17} |
| 0.15 $\text{As}_{0.34}\text{Se}_{0.30}\text{Te}_{0.21}\text{Cu}_{0.15}$ | 7.63×10^{10} | 2.74×10^8 | 2.68×10^{17} | 1.47×10^{49} | 6.76×10^{17} |

The conductance of $x = 0.075$ and $x = 0.10$ samples can also be reasonably fitted to an Arrhenius type temperature dependence, which suggest a mixture of hopping and band conduction in the temperature range of the measurement. A larger defect density of states near the Fermi level in the two Cu-rich samples increases the likelihood of variable range hopping.

10.2.2. Single-source film characterization

The compositional analysis of the single-source evaporated films from the different bulk samples indicate that no Cu has been incorporated into the films, leading to the conclusion that Cu did not evaporate congruently with other low-melting point elements during the single-source evaporation. This phenomenon may be explained by the comparatively low vapor pressure of Cu (compared to volatile As and chalcogens), at the

evaporation temperature. Due to the absence of Cu, the films do not maintain the compositional stoichiometry of the bulk source. A significant content of Te has been measured in all the films. Cross-sectional WDS elemental analysis reveals an elemental concentration gradient across a 16.5 μm thick film (Figure 59). The film was striated into three or more layers, starting from an As-rich layer near the substrate and gradually turned to a Te-rich surface layer. Similar trends have been observed in the other $(1-x)\text{As}_{0.40}\text{Se}_{0.35}\text{Te}_{0.25} + x\text{Cu}$ films when evaporated from bulk glass sample using the single-source evaporation technique. This can be attributed to volatile arsenic being preferentially evaporated from the melt, forming the As-rich bottom layer resulting in the depletion of arsenic in the source, and hence the decreased arsenic content in the films thereafter during the course of the evaporation.

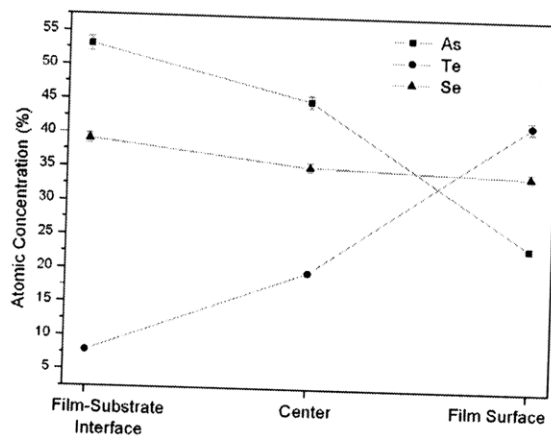


Figure 59 WDS elemental analysis results confirming the As-rich bottom layer which gradually turned into a Te-rich surface layer.

10.3. Dual source co-evaporation of As-Se-(Te)-Cu Films

To deposit films with high Cu concentrations, we have investigated a dual-source co-evaporation technique for film deposition. The composition non-uniformity due to non-congruent evaporation has been minimized by equilibrating the evaporation source prior to deposition. Instead of exhausting all the bulk materials loaded into the boats which leads to compositionally striated films, we carried out the deposition only when the evaporation reached a steady state, namely a constant deposition rate is maintained at a fixed current value. Table IV lists the compositional analysis of the dual-source co-evaporated films. $(As_2Se_3)_{100-x}(CuSe)_x$ ($x = 8, 30$) films were co-deposited simultaneously from As_2Se_3 and CuSe sources while $(As_2Te_3)_{100-x}(CuSe)_x$ ($x = 40, 60$) films were obtained by co-evaporating from As_2Te_3 and CuSe sources. The nominal compositions of the films were estimated from the individual deposition rates of As-ChG and Cu-ChG sources. From Table 12, one can notice that the films $(As_2Se_3)_{92}(CuSe)_8$ and $(As_2Se_3)_{70}(CuSe)_{30}$ films have a similar composition within the accuracy of the WDS measurement (± 1 at. %) whereas the seleno-tellurite films have the expected composition.

Figure 60 shows the transmission spectra of the co-evaporation films. An increase of Cu content in the films $(As_2Se_3)_{92}(CuSe)_8$ and $(As_2Se_3)_{70}(CuSe)_{30}$ shifts the position of the band gap to higher wavelength. This is in good agreement with the red-shift of the absorption band gap observed in bulk glasses in the system As-Se-Te-Cu (Figure 56). The absorption edge of $(As_2Te_3)_{40}(CuSe)_{60}$ is situated at shorter wavelength compared to

the one of the $(As_2Te_3)_{60}(CuSe)_{40}$ film. This is attributed to the lower Te content which blue-shifts the bandgap counteracting the Cu-doping effect.

Table 12 Composition analysis and thickness of the Cu doped films obtained by co-evaporation

| Nominal film composition | Conductivity ($1/(\Omega m)$) at 293K | Thickness (μm) $\pm 0.1 \mu m$ | Atomic percentage of actual film composition $\pm 1\%$ | | | |
|--|---|---------------------------------------|--|--------|--------|--------|
| | | | As (%) | Se (%) | Te (%) | Cu (%) |
| $(As_2Se_3)_{92}(CuSe)_8$ $As_{0.387}Se_{0.597}Cu_{0.016}$ | 0.00015 | 4.5 | 33 | 57 | | 10 |
| $(As_2Se_3)_{70}(CuSe)_{30}$ $As_{0.342}Se_{0.585}Cu_{0.073}$ | 0.00693 | 5.6 | 30 | 53 | | 17 |
| $(As_2Te_3)_{60}(CuSe)_{40}$ $As_{0.316}Se_{0.105}Cu_{0.105}Te_{0.474}$ | 0.02128 | 0.2 | 26 | 18 | 50 | 6 |
| $(As_2Te_3)_{40}(CuSe)_{60}$ $As_{0.25}Se_{0.188}Cu_{0.188}Te_{0.375}$ | 0.20364 | 0.7 | 18 | 42 | 24 | 16 |

The micro-Raman spectra of the co-evaporated films are shown in

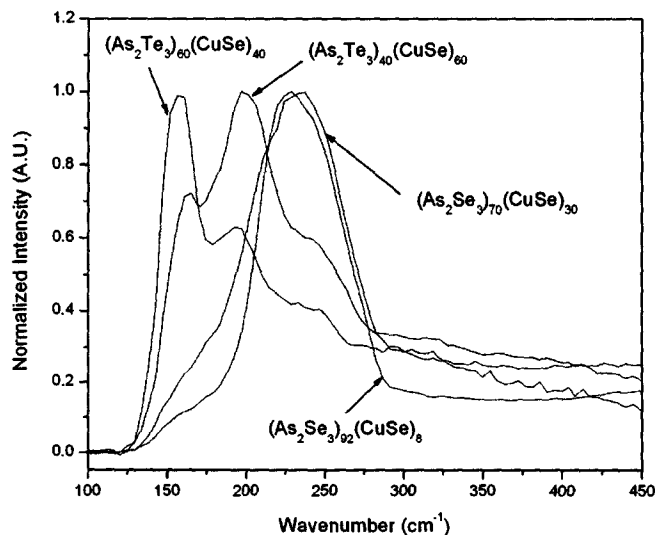


Figure 61. The spectra exhibit bands, intensity of which depends on the composition of the film, located at 150, 195 and 230 cm^{-1} . As seen in the Raman spectra of the Cu doped bulk glasses in the As-Se-Te system, the band at 150 cm^{-1} has been related to AsTe_3 units, the one at 195 cm^{-1} to mixed units $\text{AsSe}_{(3-x)}\text{Te}_x$ to and at 230 cm^{-1} to AsSe_3 pyramidal units. The following observations are made: 1) the films $(\text{As}_2\text{Se}_3)_{92}(\text{CuSe})_8$ and $(\text{As}_2\text{Se}_3)_{70}(\text{CuSe})_{30}$ exhibit a similar Raman signal. This is attributed to the similarity in their composition; and 2) the films with the composition $(\text{As}_2\text{Te}_3)_{60}(\text{CuSe})_{40}$ and $(\text{As}_2\text{Te}_3)_{40}(\text{CuSe})_{60}$ present different Raman signals. The spectrum of the $(\text{As}_2\text{Te}_3)_{60}(\text{CuSe})_{40}$ film exhibits a Raman spectrum dominated by the band at 150 cm^{-1} which is consistent with the highest Te content. The spectrum of the Se rich $(\text{As}_2\text{Te}_3)_{40}(\text{CuSe})_{60}$ film is dominated by the band at 195 cm^{-1} . Due to its higher Se content, the band at 230 cm^{-1} , which is related to the vibration of Se based units, is more pronounced compared to the one measured in the $(\text{As}_2\text{Te}_3)_{60}(\text{CuSe})_{40}$ film.

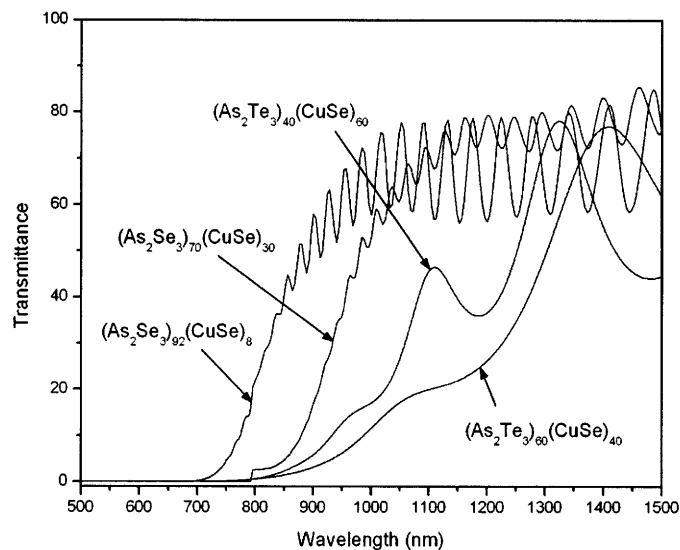


Figure 60 Transmission spectra of the Cu doped co-evaporated films

As seen for the Cu doped glasses and as shown in Table 12, the conductivity of the films measured at 293 K increases with an increase of Cu content. Figure 62 show plots of the logarithm of the conductance data versus $1/T$ and $T^{-1/4}$, respectively. As seen in Figure 62(b), the logarithm of the conductance of the $(As_2Te_3)_{40}(CuSe)_{60}$ films can be very well fitted to the $T^{-1/4}$ law with a linear coefficient as high as 0.9997. As explained previously, this indicates that carrier hopping near the Fermi level dominates the charge transport mechanism at low temperature. Assuming a localization parameter $\alpha=(10\text{\AA})^{-1}$ yields the DOS near Fermi level $1.00 \cdot 10^{19} \text{ cm}^{-3} \text{ eV}^{-1}$ for $(As_2Te_3)_{40}(CuSe)_{60}$. However, the logarithm of the conductance of the $(As_2Te_3)_{60}(CuSe)_{40}$ film can be reasonably fitted with both models suggesting a mixture of the two conduction mechanisms, which again can be attributed to the lower defect density in this glass film.

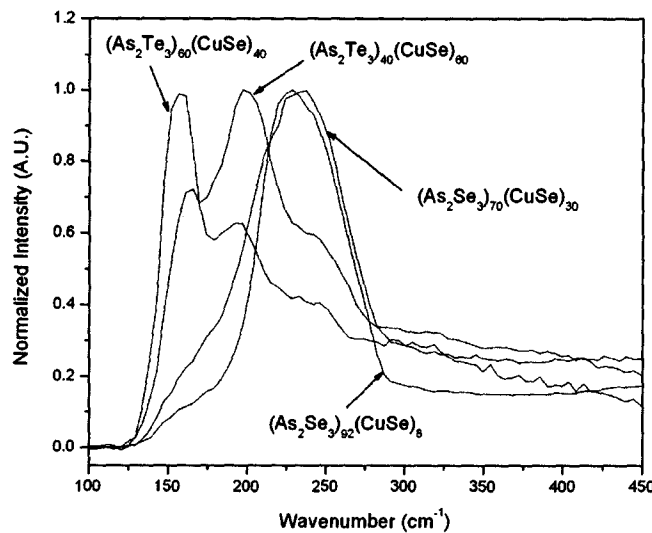
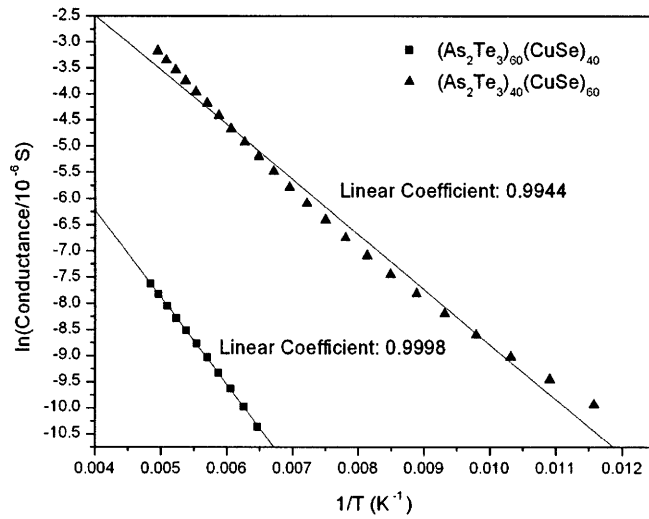
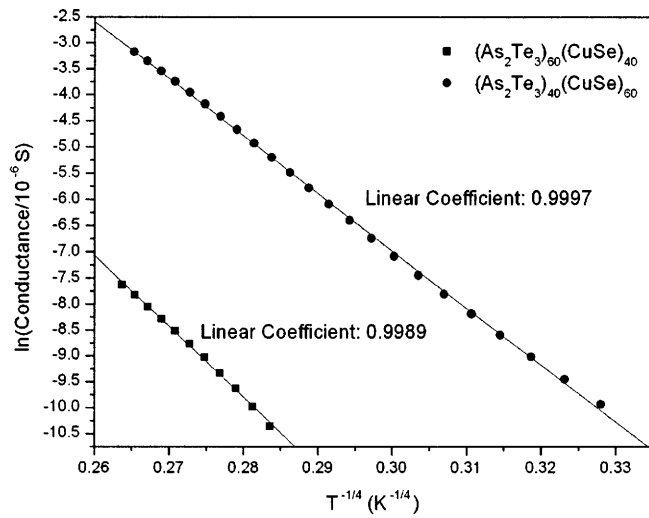


Figure 61 Micro-Raman spectra of the Cu doped co-evaporated films. The spectra exhibit different bands, intensity of which depends on the composition of the film.



(a)



(b)

Figure 62 Conductance of $(\text{As}_2\text{Te}_3)_{60}(\text{CuSe})_{40}$ and $(\text{As}_2\text{Te}_3)_{40}(\text{CuSe})_{60}$ films at low temperature fitted to different conduction models (a) $\ln(\text{Conductance})-1/T$, extended states conduction or thermal excitation of localized states; (b) $\ln(\text{Conductance})-T^{-1/4}$, variable range hopping according to Mott-Davis model. The error of the measurement is estimated to be smaller than 1 pS.

10.4. Summary

In this chapter, I summarize the results from a systematical study on the chemical modification of As-Se-Te glass systems incorporated with Cu. It is found that incorporation of Cu into the glass network increases T_g , the density and the electrical conductivity at low temperature and, also, shifts the absorption bandgap to longer wavelength.

We show that it is not possible to deposit Cu doped films with high Cu concentrations from bulk samples when this material is used as the single source in a thermal evaporator. The films are found to have a laminated compositionally non-uniform structure in thick films. We demonstrate that significant Cu content can be incorporated into selenide or seleno-telluride glass network by co-evaporating As-Se-Te and Cu-ChG systems.

The electrical conductivity properties are measured in Cu doped bulks and films and we have observed an increase in the electrical conductivity at low temperature with an increase of Cu content. We find that the charge transport mechanism at low temperature is dominated by carrier hopping near Fermi level. Further, we discover that the DOS of localized states near Fermi level increases with increasing Cu content. This finding confirms the charge defect model prediction¹²⁸.

Chapter 11. Summary and future work

11.1. Summary

In this thesis, we describe our work on the development and optimization of a lift-off patterning technique for Si-CMOS backend compatible fabrication of high-index-contrast (HIC) chalcogenide glass devices. A thermal reflow technique further removes the sidewall roughness resulting from the patterning process and is shown to effectively reduce the scattering loss in chalcogenide glass waveguides. Using the lift-off technology, we have demonstrated the first micro-ring and micro-disk resonators in chalcogenide glasses, with a record cavity quality factor (Q-factor) exceeding 2×10^5 .

11.1.1. Resonator refractometry for biological sensing

In Chapter 7, we detail our tests to confirm the biological sensing capability of the chalcogenide glass resonator sensors. The resonators are measured to have a refractive index sensitivity of 182 nm/RIU and a detection limit of refractive index change down to 8×10^{-7} RIU.

We further use the resonator to detect PSA in buffer solutions. The detection limit of the test is estimated to be ~ 0.05 ng/mL, which compares favorably with the detection limit of ELISA tests (~ 0.2 ng/mL).

11.1.2. Cavity enhanced infrared spectroscopy for chemical detection

In Chapter 8, we describe the experimental demonstration of two types of on-chip sensor devices for measuring infrared absorption. The devices are tested for N-methylaniline

sensing. The evanescent waveguide sensor yields transmission spectra in good agreement with traditional UV-Vis spectroscopy, and features an absorption detection limit down to 0.07 cm^{-1} . To resolve the physical limit between sensitivity and device footprint in evanescent waveguide sensors, we demonstrate cavity-enhanced infrared absorption spectroscopy using optofluidic micro-resonators in Ge-Sb-S chalcogenide glass. We show that slightly under-coupled (extinction ratio $\sim 12 \text{ dB}$), low loss resonant cavities lead to optimized detection limit of optical absorption in the solution. We achieve a detection limit of $\sim 0.02 \text{ cm}^{-1}$ to optical absorption in N-methylaniline solutions, using micro-disk resonators with a cavity Q-factor of $\sim 130,000$. This detection limit represents a three-fold improvement as compared to the evanescent waveguide sensor, while the physical device length is reduced by 40-fold. This result clearly proves the competitive advantage of using optical resonators for on-chip infrared absorption spectroscopic sensing.

11.1.3. Resonant cavity refractometry for precision glass metrology

Chapter 9 summarizes the work to date on using our recently developed resonant cavity refractometry technique to investigate micro-structural and property evolution in chalcogenide glasses. In resonant cavity refractometry, an optical resonant cavity is leveraged as a highly sensitive spectroscopic tool to detect refractive index and/or optical absorption change in the glass material comprising of the cavity, and thereby provide information on glass micro-structural evolution kinetics otherwise difficult to obtain using conventional metrology techniques.

We capitalize on the extreme sensitivity of optical resonance to refractive index variation to enable the sensitive detection of photo-induced index change caused by near-band gap illumination. We confirm that annealing and photosensitivity follow very different kinetic paths, suggesting that they result from dissimilar micro-structural changes.

The strong resonance enhancement effect is also utilized to measure nonlinear absorption inside chalcogenide glass using a novel cavity enhanced absorption spectroscopy technique, which clearly demonstrates the potential of cavity enhanced absorption spectroscopy as a sensitive TPA measurement technique for thin film materials.

The discovery on the cavity enhanced photosensitivity of As_2S_3 glass in film form at 1550 nm telecommunication wavelength is significant given the increasing interest in using chalcogenide glasses as a Kerr medium for ultra-fast optical switching, since high optical power density is often involved in the nonlinear optical processes. The measured photosensitivity threshold is $< 0.1 \text{ GW/cm}^2$, and photo-induced refractive index change as large as 0.016 is observed. The photosensitive process is athermal; further, we confirm the absence of two-photon absorption in As_2S_3 . These results lead us to conclude that localized state absorption accounts for the energy transfer from photons to glass network.

11.2. Future work

11.2.1. Resonator refractometry for biological sensing

Further sensitivity enhancement can be achieved by using SU8 windows with smaller size, which minimizes the loss of antigens binding to chip areas other than the resonator

surface. The long waiting time in our current test can be reduced by incorporating a microfluidic analyte transport design; the high flow velocity inside a microfluidic channel leads to a hydrodynamically decreased boundary layer thickness and hence reduced diffusion time.

Future work will also focus on examine the reproducibility and robustness of sensing experiments under different aqueous environments. For biomedical applications, it is also important to test our devices in biological fluids such as serum or urine. Tests on more molecular species will be performed to validate the platform nature of our technology.

11.2.2. Cavity enhanced infrared spectroscopy for chemical detection

The future work will focus on shifting the operating wavelength of our resonator device to mid-infrared range. Since the molecular absorption fingerprint intensity is two to three orders of magnitude higher in mid-IR than in near-IR, significant chemical detection sensitivity improvement is expected by optimizing the operating wavelength. The new design requires a waveguide structure completely fabricated out of chalcogenide glasses (i.e. the silicon oxide under cladding will be replaced by a thick chalcogenide glass under cladding). We have completed the device design and simulations, and the device fabrication work is underway. Further, involvement of thick glass films for mid-infrared work also poses new challenges and opportunities in chalcogenide glass material and processing development.

11.2.3. Resonant cavity refractometry for precision glass metrology

Systematic study will be performed to understand the aging kinetics and photosensitivity dynamics at different temperatures. Our initial results have indicated new phenomena in the thermal behaviour of chalcogenide glass films that have not been previously discovered.

Resonant cavity refractometry will be applied to characterize different chalcogenide glass film compositions. The comparison between film and bulk property variations will shed light on the structural transition during thin film deposition and processing.

Saturation behaviour of As_2S_3 photosensitivity to 1550 nm light is critically important for telecommunication applications of these glasses. Further study will be carried on to ascertain the photosensitivity saturation, as well as the dependence of photosensitivity threshold on film processing conditions, as we have suggested in Chapter 9.

11.2.4. Planar integration: case-by-case analysis

Planar integration of components with different functionalities is the key to device miniaturization and cost reduction. Future generations of the resonator sensor device may incorporate integrated light source and detector structures as well as embedded read-out circuitry for on-chip signal processing. From an application-specific perspective, the degree of integration warrants a case-by-case analysis. For example, in biomedical applications, the antibody-antigen binding is usually non-reversible, and therefore a disposable sensor chip design is appropriate. In this case, integration of resonators with

high-cost laser sources becomes essentially unnecessary. On the other hand, chemical sensors based on cavity-enhanced absorption spectroscopy with a high degree of integration may possibly open up new application arenas including remotely accessible wireless sensor network. This long-range vision will eventually fulfill the Holy Grail concept of “lab-on-a-chip”.

Appendix I. Derivation of useful relations in micro-ring/micro-disk resonators

The following important relations are derived in the context of a traveling wave resonator:

Resonant wavelength $\lambda_r = \frac{n_{eff}L}{N}, N \in Z^+$

Modal group index $n_g = n_{eff} - \lambda \frac{\partial n_{eff}}{\partial \lambda}$

Intrinsic cavity Q-factor $Q_{in} = \frac{2\pi n_g}{\alpha \lambda_r}$

Free spectral range $FSR = \frac{\lambda_r^2}{n_g L}$

Cavity finesse $F = \frac{2\pi}{\alpha L}$

Resonant field enhancement $G = \frac{F}{2\pi} \cdot (1 - T)$

Resonant wavelength shift $\Delta\lambda = \frac{\Delta n_{eff}}{n_g} \cdot \lambda$

I.1. Cavity Q-factor and optical loss

Without losing generality, let's consider a micro-ring resonator with a bending radius of R . The total cavity length L is thus $2\pi R$. Figure 63 shows a schematic diagram of a ring resonator discussed here.

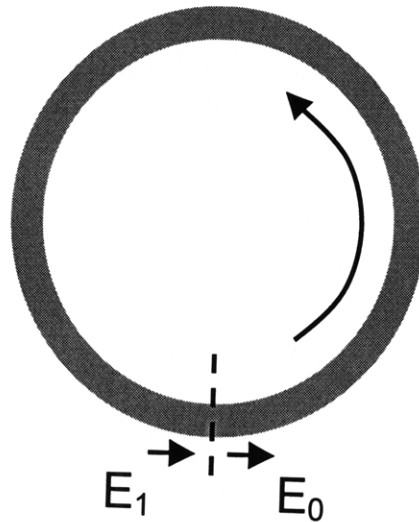


Figure 63 Schematic diagram of a micro-ring resonator, which is used as a vehicle in the derivations without losing generality

The effective index and linear power (not amplitude) loss of the waveguide comprising the ring are denoted by n_{eff} and α , respectively. We first use the phasor summation approach to derive the relation between resonator optical loss and cavity Q-factor. In this approach, the amplitudes of a traveling wave after each round trip are summed up to give the field circulating inside the resonator. Mathematically this method is similar to the ray tracing technique often used in geometric optics, the only difference being that interference between the waves is taken into account in the phasor summation approach.

Denote the electric field amplitude of a traveling wave at a given resonator cross-section as E_0 . After one round trip, the amplitude of the same wave is given by:

$$\text{Eq. 79: } E_1 = E_0 \cdot \exp\left(-\frac{\alpha L}{2}\right) \cdot \exp\left(i \cdot \frac{2\pi n_{\text{eff}} L}{\lambda}\right)$$

Similarly, after two round trips, the wave amplitude becomes:

$$\text{Eq. 80: } E_2 = E_1 \cdot \exp\left(-\frac{\alpha L}{2}\right) \cdot \exp\left(i \cdot \frac{2\pi n_{\text{eff}} L}{\lambda}\right) = E_0 \cdot \left[\exp\left(-\frac{\alpha L}{2}\right) \cdot \exp\left(i \cdot \frac{2\pi n_{\text{eff}} L}{\lambda}\right)\right]^2$$

The amplitude of the circulating wave E inside the resonator can be represented as the serial sum of E_0, E_1, E_2, \dots

$$\text{Eq. 81: } E = \sum_j E_j = \frac{E_0}{1 - \exp\left(-\frac{\alpha L}{2}\right) \cdot \exp\left(i \cdot \frac{2\pi n_{\text{eff}} L}{\lambda}\right)}, \text{ i.e.}$$

$$\text{Eq. 82: } |E|^2 = \frac{|E_0|^2}{\left|1 - \exp\left(-\frac{\alpha L}{2}\right) \cdot \exp\left(i \cdot \frac{2\pi n_{\text{eff}} L}{\lambda}\right)\right|^2}$$

Cavity Q-factor is defined as the ratio of resonant wavelength against the full width at half maximum (FWHM) of the resonant peak. Resonant condition is met when Eq. 14 is satisfied, which translates to:

$$\text{Eq. 83: } \exp\left(i \cdot \frac{2\pi n_{\text{eff}} L}{\lambda}\right) = 1$$

At resonance, the square field amplitude gives its maximum value:

$$\text{Eq. 84: } |E_r|^2 = \frac{|E_0|^2}{\left|1 - \exp\left(-\frac{\alpha L}{2}\right)\right|^2}$$

where $\delta\lambda$ represent the wavelength detuning from resonance at peak FWHM. Note that in the left hand side we use n'_{eff} to represent the effective index at the wavelength $\lambda + \delta\lambda$:

$$\text{Eq. 85: } n'_{eff} = n_{eff} + \frac{\partial n_{eff}}{\partial \lambda} \delta \lambda = n_{eff} \left(1 + \frac{1}{n_{eff}} \cdot \frac{\partial n_{eff}}{\partial \lambda} \delta \lambda \right)$$

If we assume that the cavity Q-factor is much greater than unity, the left hand side in the above expression can be Taylor expanded near λ_r , which gives:

$$\begin{aligned} & \frac{|E_0|^2}{\left| 1 - \exp\left(-\frac{\alpha L}{2}\right) \cdot \exp\left(i \cdot \frac{2\pi n'_{eff} L}{\lambda_r + \delta \lambda}\right) \right|^2} \\ &= \frac{|E_0|^2}{\left| 1 - \exp\left(-\frac{\alpha L}{2}\right) \cdot \exp\left[i \cdot \frac{2\pi n_{eff} L}{\lambda_r} \cdot \left(1 - \frac{\delta \lambda}{\lambda_r}\right) \cdot \left(1 + \frac{1}{n_{eff}} \cdot \frac{\partial n_{eff}}{\partial \lambda} \delta \lambda\right) \right] \right|^2} \\ &= \frac{|E_0|^2}{\left| 1 - \exp\left(-\frac{\alpha L}{2}\right) \cdot \exp\left[i \cdot \frac{2\pi n_{eff} L}{\lambda_r} \cdot \left(\frac{1}{n_{eff}} \cdot \frac{\partial n_{eff}}{\partial \lambda} \delta \lambda - \frac{\delta \lambda}{\lambda_r}\right) \right] \right|^2} \end{aligned}$$

In addition, because $Q \gg 1$, $\alpha L \ll 1$ and $\delta \lambda \ll 1$. Using these relations, the equation can be further simplified to give:

$$\text{Eq. 86: } \delta \lambda = \pm \frac{\alpha \lambda_r^2}{4\pi} \cdot \frac{1}{n_{eff} - \lambda_r \frac{\partial n_{eff}}{\partial \lambda}} = \pm \frac{\alpha \lambda_r^2}{4\pi n_g}$$

where we define the modal group index n_g as:

$$\text{Eq. 87: } n_g = n_{eff} - \lambda \frac{\partial n_{eff}}{\partial \lambda} = \frac{\partial \omega}{\partial k}$$

where k is the propagation constant. The second equality suggests that the modal group index is also directly correlated to the pulse propagation velocity inside a dispersed waveguide. By definition, the cavity Q-factor is:

$$\text{Eq. 88: } Q = \frac{\lambda_r}{2 |\delta \lambda|} = \frac{2\pi n_g}{\alpha \lambda_r}$$

I.2. Free spectral range and finesse

FSR is defined as the wavelength spacing between two adjacent resonant peaks (in the frequency domain, FSR is given by the frequency difference between two adjacent resonances). Denote the two adjacent resonant wavelengths as $\lambda_{r,1}$ and $\lambda_{r,2}$, and we have:

$$\text{Eq. 89: } \lambda_{r,1} = \frac{n_{eff,1}L}{N_1} \text{ and } \lambda_{r,2} = \frac{n_{eff,2}L}{N_2}$$

where $N_1 = N_2 + 1$ and $n_{eff,2} = n_{eff,1} + \frac{\partial n_{eff}}{\partial \lambda} \cdot FSR$ (a linear expansion). According to

the definition of FSR:

$$\text{Eq. 90: } FSR = \lambda_{r,2} - \lambda_{r,1} = \frac{n_{eff,2}L}{N_2} - \frac{n_{eff,1}L}{N_1} = L \cdot \frac{n_{eff,2} + N_2 \frac{\partial n_{eff}}{\partial \lambda} \cdot FSR}{N_1 N_2}$$

In most ring resonators, the resonance order $N \gg 1$. Thus as a first order approximation, $N_1 \sim N_2 \sim N$ and $\lambda_{r,1} \sim \lambda_{r,2} \sim \lambda_r$. Solve the equation above using this simplification we derive:

$$\text{Eq. 91: } FSR = \frac{\lambda_r^2}{n_g L}$$

Therefore, the cavity finesse F is defined as the ratio between FSR and resonant peak FWHM, which gives:

$$\text{Eq. 92: } F = \frac{2\pi}{\alpha L}$$

I.3. Resonant field enhancement factor

Electric field enhancement inside a resonator can be most intuitively derived from an energy conservation perspective. When a power flux I (in Watt) passes through a waveguide with linear (power) loss α , the energy loss rate per unit time along a waveguide section dL is $I\alpha \cdot dL$ (as is shown in Figure 64):

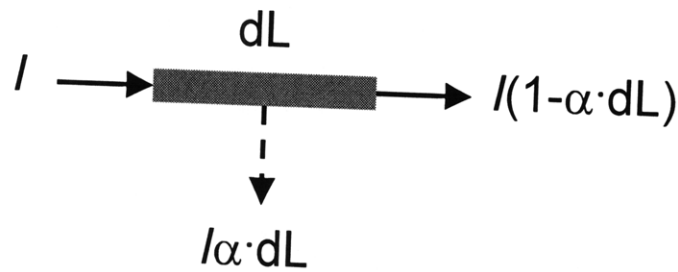


Figure 64 Schematic diagram of a waveguide section which also shows relationship between power input/output/loss

Now consider a ring resonator coupled to one bus waveguide. If we assume the power transmission coefficient at resonance is T and neglect reflection and back scattering, the energy flux into the resonator due to bus waveguide coupling is $I_0(1-T)$ when the input power flux from waveguide is denoted by I_0 . The energy loss rate inside the resonator has to equal that of the energy influx $I_0(1-T)$, which is written as:

$$\text{Eq. 93: } I\alpha L = I_0(1 - T)$$

where I denotes the circulating energy flux inside the ring resonator. The field enhancement factor G is thus given by:

$$\text{Eq. 94: } G = \frac{I}{I_0} = \frac{1 - T}{\alpha L} = \frac{F}{2\pi} \cdot (1 - T)$$

The power transmission coefficient T in Eq. 94 can be calculated using the generalized coupling matrix approach⁶⁸. The above formula can be easily adapted to the case when a ring is coupled to two waveguides, where T now represents the sum of power transmission coefficients of the through port and the drop port.

I.4. Resonant wavelength shift as a function of effective index change

When the modal effective index is modified due to external perturbations such as temperature, stress or molecular binding, the resonant wavelength also changes accordingly. Here we use $\Delta\lambda$ to denote the resonant wavelength shift when the effective index is changed from n_{eff} to $n_{eff} + \Delta n_{eff}$ at the original resonant wavelength λ_r . In this case the effective index at the new resonant wavelength $\lambda_r + \Delta\lambda$ is different from n_{eff} in two ways: 1) Δn_{eff} introduced by external perturbations; and 2) waveguide dispersion since the ring is now resonating at a different wavelength. Such consideration leads to:

$$\text{Eq. 95: } \lambda_r = \frac{n_{eff}L}{N}, \text{ and } \lambda_r + \Delta\lambda = \frac{(n_{eff} + \Delta n_{eff} + \frac{\partial n_{eff}}{\partial \lambda} \cdot \Delta\lambda)L}{N}, N \in Z^+$$

Substituting N in the expression and solve for $\Delta\lambda$ we have:

$$\text{Eq. 96: } \Delta\lambda = \frac{\Delta n_{eff}}{n_{eff} - \lambda \cdot \frac{\partial n_{eff}}{\partial \lambda}} \cdot \lambda = \frac{\Delta n_{eff}}{n_g} \cdot \lambda$$

Appendix II. Monte-Carlo simulation methodology for sensor

wavelength resolution determination

The main purpose of the simulations is to make quantitative sensor system performance predictions based on given optical resonator device parameters and instrumentation noise characteristics, and thereby bridge the gap between device parameters and system performance.

The sensor *device* under investigation is comprised of a traveling wave resonator and a coupling bus waveguide (Figure 31). Transmission spectra of the resonator are monitored *in situ*, and the resonant peak wavelength is tracked to detect the presence of molecules near sensor surface. It should be noted that conclusions derived based on travelling wave resonators can be directly applied to other resonator-based sensors, including standing wave resonators (e.g. 2-d photonic crystal cavities) and SPR sensors, provided that appropriate forms of peak fitting functions are used. In the simulation, firstly transmission spectra through a resonator are calculated using the generalized coupling matrix method proposed by A. Yariv. Our simulation and experimental results indicate a weak dependence of sensor detection limit on the resonant peak extinction ratio, and therefore a fixed extinction ratio of 15 dB is used in the simulations for consistency.

In the absence of noise, resonant peaks on the transmission spectra can be described by a Lorentzian peak function to the first-order approximation with a well-defined resonant wavelength. Considering the finite spectral width of light source used for the measurement, the measured spectra actually consist of discrete data points. Such a

discretized measurement scheme poses a constraint on sensor performance improvement through Q enhancement, since the resolution can become limited by the finite spectral width of light source. The spacing between these data points will be henceforce denoted as $\delta\lambda_s$, the spectral width of light source. If a spectrophotometer is used for the measurement, $\delta\lambda_s$ corresponds to the minimum resolvable wavelength often determined by the monochromator. If a tunable laser is employed, $\delta\lambda_s$ is defined as the minimum step size when the laser is performing a wavelength-sweeping scan. Therefore, the transmission spectra generated by the coupling matrix method is discretized into points evenly spaced with a spacing of $\delta\lambda_s$.

In reality, it is technically challenging to fabricate resonators with an exact resonant peak wavelength; thus the position of the data points relative to that of the resonant peak is randomized for each iteration in the Monte-Carlo simulation to account for fabrication variations. Randomly generated Gaussian-type intensity and wavelength noises are then superimposed onto the spectral data points. Finally a Lorentzian peak fitting of the data points (with noise) is performed to extract the “measured” resonant wavelength. The curve fitting is carried out in a range approximately corresponding to the FWHM of the resonant peak, $\Delta\lambda_{FWHM}$. Therefore, N in Eq. 44 can be approximately expressed as follows in our simulations:

$$\text{Eq. 97: } N \cong \Delta\lambda_{FWHM} / \delta\lambda_s$$

Figure 32 Exemplary transmission spectra of a resonator sensor: The black curve is the analytically calculated spectra obtained using the coupling matrix method. The open squares are the spectral data points obtained, after super-imposing Gaussian-type

intensity and wavelength noises using a Monte-Carlo method in the analytical calculation. The open square data points are spaced by a finite spectral width $\delta\lambda_s$. Finally, the red curve is the Lorentzian peak fit based on the data points. The inset shows the analytical and the fitted spectra near their minima: the ensemble average of $\Delta\lambda$ was taken as the minimum resolvable wavelength (wavelength resolution) $\Delta\lambda_{\min}$ of a sensor. illustrates an example of fitted Lorentzian peak function. The minimum resolvable wavelength shift $\Delta\lambda_{\min}$ is then statistically defined as the ensemble average of deviations of the “measured” values from the actual resonant wavelength over 1,000 Monte-Carlo iterations. Relative numerical error arising from the random nature of the Monte-Carlo method was estimated to be $\sim \pm 3\%$.

For a given device configuration in practical applications, it may be necessary to use a peak function that best describes the resonator spectral response for optimized fitting results. A number of factors can lead to resonant peak shape deviation from the ideal Lorentzian function, for example coupling of counter-propagating waves results in peak broadening and even splitting¹²⁹, Fano resonance gives sharp, asymmetric resonance behavior¹³⁰, whereas cascaded high-order resonators¹³¹ and periodically coupled resonators¹³² exhibit flattened band-pass spectral characteristics. Further, Lorentzian function only *approximates* to the first order the resonant line shape given by generalized coupling matrix approach, and the deviation becomes more pronounced when the cavity Q-factor is high.

All simulations here are situated at a resonant wavelength $\lambda_0 = 1550$ nm for simplicity and ease of comparison with experiments, although the conclusions can be easily generalized to sensor operating at other wavelengths (e.g. at water transparency window $1.06 \mu\text{m}$ for sensors operating in an aqueous environment).

Appendix III. Calculation of autocorrelation function evolution during reflow

In general the 1-d sidewall roughness distribution function $\tilde{H}(z)$ is defined between $[-\infty, \infty]$, and the roughness autocorrelation function $R(z')$ is defined in terms of ensemble average. To calculate the ensemble average, we instead consider a roughness distribution $H(z)$ defined in the finite domain $[-z_0, z_0]$. By applying a periodic boundary condition, $H(z)$ can be extended for any real z value. In this case we have:

$$\text{Eq. 98: } R(z') = \langle \tilde{H}(z) \cdot \tilde{H}(z + z') \rangle \xrightarrow{z' \ll z_0} \frac{1}{2z_0} \int_{-z_0}^{z_0} H(z) \cdot H(z + z') dz$$

where the brackets represent the ensemble average (expected values). When $z' \ll z_0$, $R(z')$ can be approximated by the right-hand-side integration form using the periodically extended function $H(z)$. According to the Wiener-Khinchin theorem:

$$\text{Eq. 99: } \sum_{k=-\infty}^{\infty} |h_k|^2 \cdot \exp\left(-\frac{i \cdot \pi \cdot k}{z_0} z'\right) = \frac{1}{2z_0} \int_{-z_0}^{z_0} H(z) \cdot H(z + z') dz$$

For any given initial autocorrelation function $R(z')$, its corresponding Fourier series coefficient $|h_k|^2$ ($t = 0$) can be calculated using Eq. 99. Additionally, the time evolution of $|h_k|^2$ (t) is quantitatively predicted by Eq. 36. Therefore $R(z', t)$ can be derived by applying an inverse Fourier transformation to $|h_k|^2$ (t).

References

- ¹ J. Wulfkuhle, L. Liotta, and E. Petricoin, "Proteomic Applications for The Early Detection of Cancer," *Nat. Rev. Cancer* **3**, 267-275 (2003).
- ² <http://www.sensata.com/files/spreetar-product-bulletin.pdf>, "Spreeta Refractive Index Sensor Product Bulletin," Texas Instruments Inc.
- ³ T. Chinowsky, J. Quinn, D. Bartholomew, R. Kaiser, and J. Elkind, "Performance of the Spreeta 2000 integrated surface plasmon resonance affinity sensor," *Sens. Actuators, B* **6954**, 1 (2003).
- ⁴ "Concentration measurements of bioactive minor proteins of bovine milk and colostrum by SPR-based biosensor analysis," *Biacore Journal* **4**, 4 (2004).
- ⁵ X. Su and J. Zhang, "Comparison of surface plasmon resonance spectroscopy and quartz crystal microbalance for human IgE quantification," *Sens. Actuators, B: Chemical* **100**, 309 (2004).
- ⁶ J. Prashar, P. Sharp, M. Scarffe, and B. Cornell, "Making lipid membranes even tougher," *J. Mater. Res.* **22**, 2189 (2007).
- ⁷ L. Fadel, F. Lochon, I. Dufour, and O. Francais, "Chemical sensing: millimeter size resonant microcantilever performance," *J. Micromech. Microeng.* **14**, S23 (2004).
- ⁸ D. Lange, C. Hagleitner, A. Hierlemann, O. Brand, and H. Baltes, "Complementary Metal Oxide Semiconductor Cantilever Arrays on a Single Chip: Mass-Sensitive Detection of Volatile Organic Compounds," *Anal. Chem.* **74**, 3084 (2002).
- ⁹ J. Verd, A. Uranga, G. Abadal, J. Teva, F. Torres, J. Lopez, F. Perez-Murano,

J. Esteve, and N. Barniol, "Monolithic CMOS MEMS oscillator circuit for sensing in the attogram range," *IEEE Electron Device Lett.* **29**, 146 (2008).

¹⁰ F. Lammers and T. Scheper, "Thermal Biosensors in Biotechnology," *Advances in Biochemical Engineering / Biotechnology Vol. 64*, Springer-Verlag Berlin Heidelberg (1999).

¹¹ <http://www.universalsensors.co.uk/data/leafletvs2.pdf>, "Universal Transducer Systems™: A Novel Protein Sensor For Diagnostics," Universal Sensors Ltd.

¹² D. Purvis, O. Leonardova, D. Farmakovskiy and V. Cherkasov, "An ultrasensitive and stable potentiometric immunosensor," *Biosens. Bioelectron.* **18**, 1385 (2003).

¹³ P. A. Martin, "Near-infrared diode laser spectroscopy in chemical process and environmental air monitoring," *Chem. Soc. Rev.* **31**, 201-210 (2002).

¹⁴ S. Hocde, O. Loreal, O. Sire, C. Boussard-Pledel, B. Bureau, B. Turlin, J. Keirsse, P. Leroyer, and J. Lucas, "Metabolic imaging of tissues by infrared fiber-optic spectroscopy: an efficient tool for medical diagnosis," *J. Biomed. Opt.* **9**, 404 (2004).

¹⁵ R. Schneider, K. Kovar, "Analysis of ecstasy tablets: comparison of reflectance and transmittance near infrared spectroscopy," *Forensic Sci. Int.* **134**, 187 (2003).

¹⁶ G. Reich, "Near-infrared spectroscopy and imaging: Basic principles and pharmaceutical applications," *Adv. Drug Delivery Rev.* **57**, 1109-1143 (2005).

¹⁷ T. McGarvey, A. Conjusteau and H. Mabuchi, "Finesse and sensitivity gain in cavity-enhanced absorption spectroscopy of biomolecules in solution," *Opt. Express* **14**, 10441-10451 (2006).

-
- ¹⁸ J. Nadeau, V. Ilchenko, D. Kossokovski, G. Bearman and L. Maleki, "High-Q whispering-gallery mode sensor in liquids," Proc. SPIE **4629**, 172-180 (2002).
- ¹⁹ G. Farca, S. Shopova, and A. Rosenberger, "Cavity-enhanced laser absorption spectroscopy using microresonator whispering-gallery modes," Opt. Express **15**, 17443-17448 (2007).
- ²⁰ A. Nitkowski, L. Chen, and M. Lipson, "Cavity-enhanced on-chip absorption spectroscopy using microring resonators," Opt. Express **16**, 11930-11936 (2008).
- ²¹ <http://www.zygo.com/?/met/interferometers/>
- ²² <http://www.metricon.com/>
- ²³ R. Swanepoel, *J. Phys. E: Sci Instrum.* **16**, 1214-1222 (1983).
- ²⁴ <http://scripts.mit.edu/~sunxc/research/tools/rtfit.html>
- ²⁵ T. Fowler and S. Elliott, "Continuous random network models for a-As₂S₃," *J. Non-Cryst. Solids* **92**, 31 (1987).
- ²⁶ C. Mariani and L. Hobbs, "Network properties of crystalline polymorphs of silica," *J. Non-Cryst. Solids* **124**, 242 (1990).
- ²⁷ G. Dohler, R. Dandoloff and H. Bilz, "A topological-dynamical model of amorphycity," *J. Non-Cryst. Solids* **42**, 87 (1980).
- ²⁸ M. Thorpe, "Continuous deformations in random networks," *J. Non-Cryst. Solids* **57**, 355 (1983).
- ²⁹ Y. Luo, *Comprehensive Handbook of Chemical Bond Energies*. CRC Press: Boca Raton, FL (2007).

-
- ³⁰ N. Mott, E. Davis, *Electronic Processes in Non-Crystalline Materials* (Oxford: Clarendon)
- ³¹ E. Mytilineou, "Chalcogenide amorphous semiconductors: chemical modification or doping?" *J. Optoelectron. Adv. Mater.* **4**, 705-710 (2002).
- ³² *Amorphous Semiconductors, Topics in Applied Physics, Vol. 36*, Edited by M. Brodsky, Springer-Verlag New York (1979).
- ³³ A. Miller, E. Abrahams, "Impurity Conduction at Low Concentrations," *Phys. Rev.* **120**, 745 (1960).
- ³⁴ V. Ambegaokar, B. Halperin, J. Langer, "Hopping Conductivity in Disordered Systems," *Phys. Rev. B* **4**, 2612-2620 (1971).
- ³⁵ D. Paul and S. Mitra, "Evaluation of Mott's Parameters for Hopping Conduction in Amorphous Ge, Si, and Se-Si," *Phys. Rev. Lett.* **31**, 1000-1003 (1973).
- ³⁶ M. Dongol, M. Zied, G. Gamal, A. El-Denglawey, "Effects of copper content and heat treatment on the electrical properties of $\text{Ge}_{15}\text{Te}_{85-x}\text{Cu}_x$ thin films," *Appl. Surface Sci.* **161**, 365-374 (2000).
- ³⁷ S. Baranovskii, I. Zvyagin, H. Cordes, S. Yamasaki, and P. Thomas, "Percolation approach to hopping transport in organic disordered solids," *Phys. Stat. Sol. B* **230**, 281-287 (2002).
- ³⁸ J. Marshall, "Computer simulation studies of low-temperature hopping in spatially and energetically disordered systems," *J. Optoelectron. Adv. Mater.* **9**, 84-91 (2007).
- ³⁹ G. Hawkins, "Spectral Characterisation of Infrared Optical Materials and Filters," Ph.D. dissertation, Dept. of Cybernetics, The University of Reading, Reading, UK 1998.

-
- ⁴⁰ A. Wilhelm, C. Boussard-Plédel, Q. Coulombier, J. Lucas, B. Bureau, and P. Lucas, “Development of Far-Infrared-Transmitting Te Based Glasses Suitable for Carbon Dioxide Detection and Space Optics,” *Adv. Mater.* **19**, 3796-3800, (2007).
- ⁴¹ S. Shibata, M. Moriguchi, K. Jinguchi, S. Mitachi, T. Kanamori, and T. Tanabe, “Prediction of Loss Minima in Infra-red Optical Fibers,” *Electron. Lett.* **17**, 775 (1981).
- ⁴² R. Olshansky, “Propagation in glass optical waveguides,” *Rev. Mod. Phys.* **51**, 341-367 (1979).
- ⁴³ C. Lopez, “Evaluation of the photo-induced structural mechanisms in chalcogenide glass,” University of Central Florida Ph.D Thesis (2004).
- ⁴⁴ A. van Popta, R. DeCorby, C. Haugen, T. Robinson, J. McMullin, D. Tonchev, and S. Kasap, “Photoinduced refractive index change in As_2Se_3 by 633nm illumination,” *Opt. Express* **10**, 639-644 (2002).
- ⁴⁵ G. Yang, H. Jain, A. Ganjoo, D. Zhao, Y. Xu, H. Zeng, G. Chen, “A photo-stable chalcogenide glass,” *Opt. Express* **16**, 10565-10571 (2008).
- ⁴⁶ N. Hô, M. Phillips, H. Qiao, P. Allen, K. Krishnaswami, B. Riley, T. Myers, and N. Anheier, “Single-mode low-loss chalcogenide glass waveguides for the mid-infrared,” *Opt. Lett.* **31**, 1860-1862 (2006).
- ⁴⁷ A. Saliminia, A. Villeneuve, T. V. Galstian, S. LaRochelle, and K. Richardson, “First and second order Bragg gratings in single mode planar waveguides of chalcogenide glasses,” *J. Lightwave Technol.* **17**, 837-842 (1999).
- ⁴⁸ N. Hô, J. Laniel, R. Vallée, and A. Villeneuve, “Photosensitivity of As_2S_3 chalcogenide thin films at 1.5 μm ,” *Opt. Lett.* **28**, 965-967 (2003).

-
- ⁴⁹ H. Hisakuni and K. Tanaka, "Optical microfabrication of chalcogenide glasses," *Science* **270**, 974 (1995).
- ⁵⁰ V. Zhdanov, B. Kolomiets, V. Lyubin, and V. Malinovsky, "Photoinduced optical anisotropy in chalcogenide vitreous semiconducting films," *Phys. Stat. Sol. A* **52**, 621 (1979).
- ⁵¹ J. Feinleib, J. Deneufville, S. Moss, S. Ovshinsky, "Rapid reversible light-induced crystallization of amorphous semiconductors," *Appl. Phys. Lett.* **16**, 254-257 (1971).
- ⁵² K. Tanaka, "Photoinduced processes in chalcogenide glasses," *Curr. Opin. Solid State Mater. Sci.* **1**, 567-571 (1996).
- ⁵³ V. Ta'eed, N. Baker, L. Fu, K. Finsterbusch, M. Lamont, D. Moss, H. Nguyen, B. Eggleton, D. Choi, S. Madden, and B. Luther-Davies, "Ultrafast all-optical chalcogenide glass photonic circuits," *Opt. Express* **15**, 9205-9221 (2007).
- ⁵⁴ M. Pelusi, F. Luan, T. Vo, M. Lamont, S. Madden, D. Bulla, D. Choi, B. Luther-Davies, and B. Eggleton, "Photonic-chip-based radio-frequency spectrum analyzer with terahertz bandwidth," *Nat. Photonics* **3**, 139 (2009).
- ⁵⁵ E. Vogel, M. Weber, and D. Krol, "Nonlinear Optical Phenomena in Glass," *Phys. Chem. Glasses* **32**, 231-254 (1991).
- ⁵⁶ R. Slusher, G. Lenz, J. Hodelin, J. Sanghera, L. Shaw, and I. Aggarwal, "Large Raman gain and nonlinear phase shifts in high-purity As_2Se_3 chalcogenide fibers," *J. Opt. Soc. Am. B* **21**, 1146-1155 (2004).
- ⁵⁷ M. Yamane, and Y. Asahara, *Glasses for photonics*, University Press, Cambridge, 2000.

-
- ⁵⁸ G. Agrawal, *Nonlinear Fiber Optics*, Academic Press, San Diego, 2001.
- ⁵⁹ Y. Ruan, R. Jarvis, A. Rodeb, S. Madden, and B. Luther-Davies, "Wavelength dispersion of Verdet constants in chalcogenide glasses for magneto-optical waveguide devices," *Opt. Commun.* **252**, 39-45 (2005).
- ⁶⁰ A. Ganjoo, H. Jain, C. Yu, J. Irudayaraj and C. Pantano, "Detection and fingerprinting of pathogens: Mid-IR biosensor using amorphous chalcogenide films," *J. Non-Cryst. Solids*, **354**, 2757-2762 (2008).
- ⁶¹ *Laser-Induced Damage in Optical Materials: 2003*, edited by G. Exarhos, A. Guenther, N. Kaiser, K. Lewis, M. Soileau, and C. Stolz, *Proceedings of SPIE Vol. 5273*.
- ⁶² A. Zoubir, M. Richardson, C. Rivero, A. Schulte, C. Lopez, K. Richardson, N. Ho, and R. Vallée, "Direct femtosecond laser writing of waveguides in As_2S_3 thin films," *Opt. Lett.* **29**, 748 (2004).
- ⁶³ S. Madden, D. Choi, D. Bulla, A. Rode, B. Luther-Davies, V. Ta'eed, M. Pelusi, and B. Eggleton, "Long, low loss etched As_2S_3 chalcogenide waveguides for all-optical signal regeneration," *Opt. Express* **15**, 14414-14421 (2007).
- ⁶⁴ Y. Akahane, T. Asano, B. Song, and S. Noda, "High-Q photonic nanocavity in a two-dimensional photonic crystal," *Nature* **425**, 944 (2003).
- ⁶⁵ M. Gorodetsky, A. Savchenkov, and V. Ilchenko, "Ultimate Q of optical microsphere resonators," *Opt. Lett.* **21**, 453-455 (1996).
- ⁶⁶ D. Armani, T. Kippenberg, S. Spillane and K. Vahala, "Ultra-high-Q toroid microcavity on a chip," *Nature* **421**, 925-929 (2003).

-
- ⁶⁷ M. Borselli, T. Johnson, and O. Painter, "Beyond the Rayleigh scattering limit in high-Q silicon microdisks: theory and experiment," *Opt. Express* **13**, 1515-1530 (2005).
- ⁶⁸ A. Yariv, "Universal relations for coupling of optical power between microresonators and dielectric waveguides," *Electron. Lett* **36**, 321-322 (2000).
- ⁶⁹ B. Little, S. Chu, H. Haus, J. Foresi, and J. Laine, "Microring resonator channel dropping filters," *IEEE J. Lightwave Technol.* **15**, 998 (1997).
- ⁷⁰ S. Xiao, M. Khan, H. Shen, and M. Qi, "Modeling and measurement of losses in silicon-on-insulator resonators and bends," *Opt. Express* **15**, 10553-10561 (2007).
- ⁷¹ R. Jones, "New calculus for the treatment of optical systems," *J. Opt. Soc. Am.* **31**, 488-493 (1941).
- ⁷² M. Popović, T. Barwicz, M. Watts, P. Rakich, L. Socci, E. Ippen, F. Kärtner and H. Smith, "Multistage high-order microring-resonator add-drop filters," *Opt. Lett.* **31**, 2571-2573 (2006).
- ⁷³ V. Almeida, C. Barrios, R. Panepucci, and M. Lipson, "All-optical control of light on a silicon chip," *Nature* **431**, 1081 (2004).
- ⁷⁴ Q. Xu, V. Almeida, and M. Lipson, "Micrometer-scale all-optical wavelength converter on silicon," *Opt. Lett.* **30**, 2733 (2005).
- ⁷⁵ M. Eichenfield, C. Michael, R. Perahia and O. Painter, "Actuation of micro-optomechanical systems via cavity-enhanced optical dipole forces," *Nat. Photonics* **1**, 416 (2007).
- ⁷⁶ J. Galas, J. Torres, M. Belotti, Q. Kou, and Y. Chen, "Microfluidic tunable dye laser with integrated mixer and ring resonator," *Appl. Phys. Lett.* **86**, 264101 (2005).

-
- ⁷⁷ B. Kuadzhe, G. Ustyugov, A. Kudryavtsev, "Vapor pressure and thermal stability of arsenic chalcogenides," *Tr. Inst. Mosk. Khim. Tekhnol. Inst. im. D. I. Mendeleeva* **58**, 29-32 (1968).
- ⁷⁸ B. Brunetti, V. Piacente, and P. Scardala, "Torsion Measurement of Orpiment Vapor Pressure," *J. Chem. Eng. Data* **52**, 1343-1346 (2007).
- ⁷⁹ V. Ban, B. Knox, "Mass-spectrometric study of the laser-induced vaporization of compounds of arsenic and antimony with the elements of Group VIa," *J. Chem. Phys.* **521**, 248-253 (1970).
- ⁸⁰ N. Carlie, J. Hu, L. Petit, A. V. Rode, A. Agarwal, L. C. Kimerling, B. Luther-Davies and K. Richardson, "Comparison of the optical and thermal properties and structure of Ge-Sb-S thin films deposited using thermal evaporation and pulsed laser deposition techniques," to be submitted.
- ⁸¹ W. Li, Y. Ruan, B. Luther-Davies, A. Rode, and R. Boswell, "Dry-etch of As₂S₃ thin films for optical waveguide fabrication," *J. Vac. Sci. Technol. A* **23**, 1626-1632 (2005).
- ⁸² O. Joubert, P. Paniez, M. Pons, and J. Pelletier, "Polymer behavior under plasma etching: Influence of physical properties on kinetics and durability," *J. Appl. Phys.* **70**, 977 (1991).
- ⁸³ C. Huang, D. Hewak, and J. Badding, "Deposition and characterization of germanium sulphide glass planar waveguides," *Opt. Express* **12**, 2501 (2004).
- ⁸⁴ L. Petit, N. Carlie, F. Adamietz, M. Couzi, V. Rodriguez, and K. C. Richardson, "Raman and infrared spectroscopic studies of Ge-Ga-Ag sulphide glasses," *Mater. Chem. Phys.* **97**, 64 (2006).

-
- ⁸⁵ Q. Mei, J. Saienga, J. Schrooten, B. Meyer, and S. Martin, "Preparation and characterization of glasses in the $\text{Ag}_2\text{S}+\text{B}_2\text{S}_3+\text{GeS}_2$ system," *J. Non-Cryst. Solids* **324**, 264 (2003).
- ⁸⁶ L. Petit, N. Carlie, F. Adamietz, M. Couzi, V. Rodriguez, and K. C. Richardson, "Correlation between physical, optical and structural properties of sulfide glasses in the system Ge-Sb-S," *Mater. Chem. Phys.* **97**, 64 (2006).
- ⁸⁷ S. Campbell, *The Science and Engineering of Microelectronic Fabrication*, Oxford University Press, 1996.
- ⁸⁸ C. Xu, W. Huang, M. Stern, and S. Chaudhuri, "Full-vectorial mode calculations by finite difference method," *IEE Proc. Optoelectron.* **141**, 281 (1994).
- ⁸⁹ S. Suriñach, E. Illekova, G. Zhang, M. Poulain, and M. Baró, *J. Mater. Res.* **11**, 2633 (1996).
- ⁹⁰ <http://www.amorphousmaterials.com/IR%20Fibers.htm>
- ⁹¹ P. Roberts, F. Couny, H. Sabert, B. Mangan, D. Williams, L. Farr, M. Mason, A. Tomlinson, T. Birks, J. Knight and P. Russell, "Ultimate low loss of hollow-core photonic crystal fibres," *Opt. Express* **13**, 236-244 (2005).
- ⁹² F. Ladouceur, J. D. Love, and T. J. Senden, "Effect of side wall roughness in buried channel waveguides," *Proc. Inst. Elect. Eng. Optoelectron.* **141**, 242–248 (1994).
- ⁹³ J. Lacey and F. Payne, "Radiation loss from planar waveguides with random wall imperfections," *IEE Proc.*, **137**, 282-288 (1990).

-
- ⁹⁴ T. Barwicz and H. Haus, "Three-dimensional analysis of scattering losses due to sidewall roughness in microphotonic waveguides," *J. Lightwave Technol.* **23**, 2719 (2005).
- ⁹⁵ R. Wang, S. Madden, C. Zha, A. Rode, and B. Luther-Davies, "Annealing induced phase transformations in amorphous As_2S_3 films," *J. Appl. Phys.* **100**, 063524 (2006).
- ⁹⁶ N. Feng, G. Zhou, C. Xu, and W. Huang, "Computation of full-vector modes for bending waveguide using cylindrical perfectly matched layers," *IEEE J. Lightwave Technol.* **20**, 1976 (2002).
- ⁹⁷ A. Sv Sudbo, "Film mode matching: a versatile numerical method for vector mode field calculations in dielectric waveguides," *Pure Appl. Opt.* **2**, 211-233 (1993).
- ⁹⁸ H. Haus, W. Huang, S. Kawakami, and N. Whitaker, "Coupled-mode theory of optical waveguides," *IEEE J. Lightwave Technol.* **5**, 16 (1987).
- ⁹⁹ Y. Ruan, M. Kim, Y. Lee, B. Luther-Davies, A. Rode, "Fabrication of high-Q chalcogenide photonic crystal resonators by e-beam lithography," *Appl. Phys. Lett.* **90**, 071102 (2007).
- ¹⁰⁰ G. Elliott, D. Hewak, G. Murugan, and J. Wilkinson, "Chalcogenide glass microspheres; their production, characterization and potential," *Opt. Express* **15**, 17542 (2007).
- ¹⁰¹ I. White and X. Fan, "On the performance quantification of resonant refractive index sensors," *Opt. Express* **16**, 1020-1028 (2008).
- ¹⁰² J. Homola, S. Yee, and G. Gauglitz, "Surface plasmon resonance sensors: review," *Sens. Actuators, B* **54**, 3-15 (1999).

-
- ¹⁰³ C. Barrios, M. Bañuls, V. González-Pedro, K. Gylfason, B. Sánchez, A. Griol, A. Maquieira, H. Sohlström, M. Holgado, and R. Casquel, "Label-free optical biosensing with slot-waveguides," *Opt. Lett.* **33**, 708-710 (2008).
- ¹⁰⁴ Y. Kokubun, M. Takizawa, and S. Taga, "Three-dimensional athermal waveguides for temperature independent lightwave devices," *Electron. Lett.* **30**, 1223-1224 (1994).
- ¹⁰⁵ See for example: T. Clark, M. Currie, and P. Matthews, "Digitally Linearized Wide-Band Photonic Link," *J. Lightwave Technol.* **19**, 172-179 (2001). In practical applications, it is necessary to specify the measurement bandwidth at which the SNR is attained to obtain S* value and an accurate description of the sensor system.
- ¹⁰⁶ H. Zhu, I. White, J. Suter, P. Dale and X. Fan, "Analysis of biomolecule detection with optofluidic ring resonator sensors," *Opt. Express* **15**, 9139-9146 (2007).
- ¹⁰⁷ W. Irvine and J. Pollack, "Infrared optical properties of water and ice spheres," *Icarus* **8**, 324 (1968).
- ¹⁰⁸ J. D. Jackson, *Classical Electrodynamics*, 3rd ed., New York: Wiley (1998).
- ¹⁰⁹ S. Shaji, S. Eappen, T. Rasheed, K. Nair, "NIR vibrational overtone spectra of N-methylaniline, N,N-dimethylaniline and N,N-diethylaniline - a conformational structural analysis using local mode model," *Spectrochim. Acta, Part A*, **60**, 351-355 (2004).
- ¹¹⁰ J. Robinson, L. Chen, and M. Lipson, "On-chip gas detection in silicon optical microcavities," *Opt. Express* **16**, 4296-4301 (2008).
- ¹¹¹ J. Laniel, J. Ménarda, K. Turcotte, A. Villeneuve, R. Vallée, C. Lopez, and K. Richardson, "Refractive index measurements of planar chalcogenide thin film," *J. Non-Cryst. Solids* **328**, 183 (2003).

-
- ¹¹² A. van Popta, R. DeCorby, C. Haugen, T. Robinson, J. McMullin, D. Tonchev, and S. Kasap, "Photoinduced refractive index change in As₂Se₃ by 633nm illumination," *Opt. Express* **10**, 639 (2002).
- ¹¹³ M. Lee, C. Grillet, C. Smith, D. Moss, B. Eggleton, D. Freeman, B. Luther-Davies, S. Madden, A. Rode, Y. Ruan, and Y. Lee, "Photosensitive post tuning of chalcogenide photonic crystal waveguides," *Opt. Express* **15**, 1277 (2007).
- ¹¹⁴ R. Wang, S. Madden, C. Zha, A. Rode, and B. Luther-Davies, *J. Appl. Phys.* **100**, 063524 (2006).
- ¹¹⁵ P. Lucas, "Energy landscape and photoinduced structural changes in chalcogenide glasses," *J. Phys.: Condens. Matter* **18**, 5629-5638 (2006).
- ¹¹⁶ P. Lucas, E. King, A. Doraiswamy, and P. Jivaganont, "Competitive photostructural effects in Ge-Se glass," *Phys. Rev. B* **71**, 104207 (2005).
- ¹¹⁷ H. Fritzsche, "Toward understanding the photoinduced changes in chalcogenide glasses," *Semiconductors* **32**, 850 (1998).
- ¹¹⁸ A. Saliminia, T. Galstian, A. Villeneuve, and K. Le Foulgoc, "Temperature dependence of Bragg reflectors in chalcogenide As₂S₃ glass slab waveguides," *J. Opt. Soc. Am. B* **17**, 1343-1348 (2000).
- ¹¹⁹ L. Petit, N. Carlie, A. Humeau, G. Boudebs, H. Jain, A. Miller and K. Richardson, "Correlation between the nonlinear refractive index and structure of germanium-based chalcogenide glasses," *Mater. Res. Bull.* **42**, 2107-2116 (2007).

-
- ¹²⁰ H. Nguyen, K. Finsterbusch, D. Moss, B. Eggleton, "Measurement of n_2 and two-photon absorption in As_2Se_3 chalcogenide single-mode fiber," Conference on Optical Fiber Technology/Australian Optical Society (2006).
- ¹²¹ D. Broaddus, M. Foster, I. Agha, J. Robinson, M. Lipson, and A. Gaeta, "Silicon-waveguide-coupled high-Q chalcogenide microspheres," *Opt. Express* **17**, 5998-6003 (2009).
- ¹²² C. Rivero, P. Sharek, W. Li, K. Richardson, A. Schulte, G. Braunstein, R. Irwin, V. Hamel, K. Turcotte and E. Knystautas, "Structural analysis of chalcogenide waveguides using Rutherford backscattering spectroscopy," *Thin Solid Films* **425**, 59-67 (2003).
- ¹²³ M. Koide, R. Sato, T. Komatsu, K. Matusita, "Viscosity and relaxation of glasses below the glass transition temperature," *Thermochim. Acta* **280/281**, 401-415 (1996).
- ¹²⁴ S. Etienne, J. Cavaille, J. Perez, G. Johari "Effect of physical ageing on the mechanical relaxation of a chalcogenide glass," *Philos. Mag. A* **51**, L35-L40 (1985).
- ¹²⁵ N. Savchenko, T. Shchurova, N. Baran, A. Spesivkyh, "Relaxation processes in As_2S_3 thin films," *Vacuum* **80**, 128 (2005).
- ¹²⁶ K. Richardson, C. Lopez, A. Schulte, C. Rivero, A. Saliminia, T. Galstian, K. Turcotte, A. Villeneuve, "Aging behavior of photo-induced As_2S_3 gratings," Conference on Lasers and Electro-Optics (2001).
- ¹²⁷ V. Nguyen, J. Sanghera, J. Freitas, I. Aggarwal, I. Lloyd, "Structural investigation of chalcogenide and chalcogen halide glasses using Raman spectroscopy," *J. Non-Cryst. Solids*, **248**, 103-114 (1999).

-
- ¹²⁸ S. Ovshinsky and D. Adler, "Local structure, bonding, and electronic properties of covalent amorphous semiconductors," *Contemp. Phys.* **19**, 109 (1978).
- ¹²⁹ B. Little, J. Laine, and S. Chu, "Surface-roughness-induced contradirectional coupling in ring and disk resonators," *Opt. Lett.* **22**, 4-6 (1997).
- ¹³⁰ U. Fano, "Effects of Configuration Interaction on Intensities and Phase Shifts," *Phys. Rev.* **124**, 1866-1878 (1961).
- ¹³¹ R. Orta, P. Savi, R. Tascone, and D. Trincherro, "Synthesis of multiple-ring-resonator filters for optical systems," *IEEE Photon. Technol. Lett.* **7**, 1447-1449 (1995).
- ¹³² B. Little, S. Chu, J. Hryniewicz, and P. Absil, "Filter synthesis for periodically coupled microring resonators," *Opt. Lett.* **25**, 344-346 (2000).